TIME-RESOLVED IMAGING AND ELECTRON DIFFRACTION OF LASER-DRIVEN PLUMES

By

Meghanad Kayanattil

Dissertation submitted to the University of Hamburg in partial fulfillment of the requirements for the degree of Doctor of Philosophy

Faculty of Mathematics, Informatics, and Natural Sciences, Department of Chemistry, University of Hamburg
Max Planck Institute for the Structure and Dynamics of Matter
Hamburg, Germany

2023

mpsd

Universität Hamburg
DER FORSCHUNG | DER LEHRE | DER BILDUNG

The work described in this dissertation was carried out at the Department of Atomically Resolved Dynamics and the Scientific Support Unit - Ultrafast Beams at the Max Planck Institute for the Structure and Dynamics of Matter, Hamburg, from February 2019 through June 2023.

List of publications

This thesis is based in part on the following publications. Figures and sections from published documents, all of which have been accurately cited and used with appropriate permissions.

1. **Meghanad Kayanattil**, Zhipeng Huang, Djordje Gitaric and Sascha W. Epp, "Rubber-like elasticity in laser-driven free surface flow of a Newtonian fluid" Proceedings of the National Academy of Sciences (PNAS), 120(27), e2301956120 (2023), https://doi.org/10.1073/pnas.2301956120

2. Zhipeng Huang **Meghanad Kayanattil**, Stuart A. Hayes, and RJ Dwayne Miller, "Picosecond infrared laser driven sample delivery for simultaneous liquid-phase and gas-phase electron diffraction studies" Structural Dynamics, 9, 054301 (2022), https://doi.org/10.1063/4.0000159

Contents

Part I

Part II

Appendix

6

Nomenclature

$\boldsymbol{\lambda_l}$: Wavelength

$\boldsymbol{\tau_l}$: Laser pulse length

PLA : Pulsed laser ablation

J : Joule (SI unit of energy)

mJ : Millijoule (10^{-3} J)

$\boldsymbol{\mu}$**J** : Microjoule (10^{-6} J)

cm : Centimeter (10^{-2} m)

mm : Millimeter (10^{-3} m)

$\boldsymbol{\mu}$**m** : Micrometer (10^{-6} m)

nm : Nanometer (10^{-9} m)

Å : Angstrom (10^{-10} m)

fs : Femtosecond (10^{-15} s)

ps : Picosecond (10^{-12} s)

ns : Nanosecond (10^{-9} s)

$\boldsymbol{\mu}$**s** : Microsecond (10^{-6} s)

ms : Millisecond (10^{-3} s)

cw : Continuous wave

$\boldsymbol{\eta}$: Viscosity

NF : Newtonian fluid

$\boldsymbol{\sigma_s}$: Shear stress

DMA : Dynamic Mechanical Analysis

$\boldsymbol{\omega}$: Angular frequency ($\frac{2\pi}{T}$)

$\boldsymbol{\epsilon_s}$: Shear strain

$\boldsymbol{G}$: Shear modulus

Hz : Hertz (SI unit of frequency)

kHz : Kilohertz (10^3 Hz)

MHz : Megahertz (10^6 Hz)

GHz : Gigahertz (10^9 Hz)

TCV : Taylor-Culick Velocity

$\boldsymbol{\rho}$: Density

$\boldsymbol{\sigma_{ST}}$: Surface tension

$\boldsymbol{\tau_m}$: Molecular (diffusion) relaxation time

$\boldsymbol{\mu_a}$: Absorption coefficient

$\boldsymbol{c_s}$: Sound velocity

IR : Infra-Red

LIFT : Laser-induced forward transfer

$\boldsymbol{\sigma^*}$: Tensile strength (of the material)

$\boldsymbol{\sigma_p}$: Peak tensile strength (induced)

$\boldsymbol{\Gamma}$: Grüneisen parameter

$\boldsymbol{F_{peak}}$: Peak fluence

Pa : Pascal (SI unit of pressure)

bar : Unit of pressure, 1 bar = 10^5 Pa

mbar : Millibar (10^{-3} bar)

MPa : Megapascal (10^6 Pa)

GPa : Gigapascal (10^9 Pa)

N : Newton (SI unit of force)

$\boldsymbol{G^*}$: Complex shear modulus

$\boldsymbol{G'}$: Storage modulus

$\boldsymbol{G''}$: Loss modulus

$\boldsymbol{G_\infty}$: High-frequency shear modulus

UK : United Kingdom

USA : United States of America

$\boldsymbol{f}$: Focal length

CCD : Charge-coupled device

PIRL : Pico-second infra-red laser

ND : Neutral density

FWHM : Full width at half maximum

mW : Milliwatt (10^{-3} W)

V : Volt (SI unit of electric potential)

8

HSD : Hypothetical Spallation Depth

Z_e : Effective path length

USAF : United States Air Force

RP : Rayleigh-Plesset (equation)

DYM : Dynamic Young's modulus

E : Young's modulus

ν : Poisson's ratio

SE : Surface Energy

KE : Kinetic Energy

RHS : Right Hand Side

LHS : Left Hand Side

eV : Electron-volt (1.6×10^{-19} J)

keV : Kilo-electron-volt (10^3 eV)

MeV : Mega-electron-volt (10^6 eV)

CHD : Cyclohexadiene

CF$_3$I : Trifluoroiodomethane

CCl$_4$: Carbon tetrachloride

CO$_2$: Carbon dioxide

ED : Electron diffraction

UED : Ultra-fast electron diffraction

DC : Direct current

Nd:YAG : Neodymium-doped Yttrium Aluminum Garnet (lasing medium)

MD : Molecular Dynamic

Ti:Sapphire : Titanium Sapphire (lasing medium)

UV : Ultra-Violet

pl : Picoliter (10^{-12} l)

μ**l** : Microliter (10^{-6} l)

Zusammenfassung

Die gepulste Laserablation von Flüssigkeiten, bei der Laserpulse zum Materialabtrag eingesetzt werden, findet in zahlreichen Bereichen Anwendung, darunter Lithografie, Druck, Chirurgie und chemische Analyse. Die Dynamik, die sich nach der Wechselwirkung zwischen dem Ablationslaser und der Flüssigkeit entfaltet, ist komplex und Gegenstand umfangreicher Forschung.

In dieser Arbeit wird zunächst der Aufbau und die Anwendung eines Hellfeld Bildgebungsaufbaus zur Untersuchung der gepulsten Laserablation von vakuumstabilen Flüssigkeiten unter verschiedenen Einflüssen und Außendrücken beschrieben. Die nach der Laserablation im Vakuum erzeugten Ablationsfahnen zeigen eine bisher nicht beobachtete Blasenbildung, welche untersucht und analysiert wird. Viskosität und Oberflächenspannung können die Dynamik der Blasenbildung nicht erklären. Eine sorgfältiger Analyse der Dynamik zeigt, dass die Scherelastizität, die normalerweise nicht mit Flüssigkeiten in Verbindung gebracht wird, unter diesen Umständen die treibende Kraft der Dynamik in flüssigem Glycerin ist. Wir bestimmen für die lasererzeugten Blasen einen Elastizitätsmodul von etwa 0.2 MPa, was jenem von Gummi entspricht. Ferner gelang es durch die Analyse des Berstvorgangs über die Geschwindigkeit der Lochentwicklung ein ähnliches Schermodul von etwa 0.48 MPa zu bestimmen. Solch Schermodulwerte belegen, dass die Glycerinhülle der Blase ein Verhalten wie normalerweise nur beobachtbar in Materialien wie Gummi aufweist, mit ähnlichen Elastizitätswerten und der Toleranz gegenüber großen Verformungen. Glycerin zählt zu den Newtonschen Flüssigkeit. Newtonschen Flüssigkeitn zeichnen sich dadurch aus, dass sie bei Verformung ein viskoses Verhalten zeigen. In der Regel wird eine festkörperähnliche elastische Reaktion nur beobachtet, wenn Newtonsche Flüssigkeiten auf sehr kurzen Zeitskalen, die kürzer sind als die im Nanosekundenbereich liegende molekulare Diffusionszeit eines einzelnen Moleküls, verformt und unter-

sucht werden. Unsere Ergebnisse zeigen jedoch, dass die Elastizität dieser Flüssigkeit viel länger anhält, vier Größenordnungen über die molekulare Diffusionszeit hinaus. Dies deuten auf das Vorhandensein eines metastabilen Zustands hin, der durch langreichweitige, festkörperähnliche Wechselwirkungen in der Flüssigkeit gekennzeichnet ist. Dies läd zu einer Neubewertung unseres derzeitigen Verständnisses des flüssigen Zustands ein.

Im zweiten Teil der Arbeit wurden die mit dem Laser abgetragenen Fahnen mit zeitaufgelöster Elektronenbeugung untersucht. Die Laserablation von Flüssigkeiten in Verbindung mit der Elektronenbeugung ermöglichte es, die radialen Verteilungsfunktionen von zwei verschiedenen Phasen von Glycerin zu beobachten: Gas und Flüssigkeit. Unseres Wissens nach ist dies das erste Mal, dass mittels eine einzigen Probenquelle isolierte und kondensierte Phasen für Elektronenbeugungsstudien erzeugt und untersucht wurden.

Abstract

Pulsed laser ablation of liquids, in which laser pulses are used to remove material, has applications in a wide range of fields, including lithography, printing, surgery, and chemical analysis. The dynamics that unfold after the interaction between the ablation laser and the liquid are complex and the subject of extensive research.

This thesis first describes the design and use of a brightfield imaging setup to study pulsed laser ablation of vacuum stable liquids at different fluence and external pressure ranges. The plumes generated after laser ablation in a vacuum exhibit a novel bubble formation. The behavior of these bubbles is studied and analyzed. Equilibrium viscosity and surface tension fail to explain the bubble growth and rupture dynamics. Our analysis identifies shear elasticity, not typically associated with liquids, as the driving force for this surface flow in liquid glycerol under laser ablation. We determine Young's modulus of about 0.2 MPa for the laser-driven bubbles, which is a large rubber-like value. In addition, by analyzing the rupture of the bubble and the speed of the retracting film, we again find a similarly large shear modulus of about 0.48 MPa. These values provide evidence that the glycerol shell exhibits solid-like behavior with similar elasticity values and tolerance to large deformation strains that are typically only observed in materials such as rubber.

Glycerol is a well-known Newtonian fluid. When subjected to deformation, Newtonian fluids are expected to exhibit viscous behavior. Typically, a solid-like elastic response is only observed when Newtonian fluids are deformed and probed on very short time scales, shorter than the nanosecond molecular diffusion time of a single molecule. However, our results show that the elasticity of this fluid persists for much longer, extending four orders of magnitude beyond the molecular diffusion time. Our results imply the presence of a metastable state characterized by solid-like long-range correlations in the liquid. This invites a re-evaluation of our current understanding

of the liquid state.

The laser-ablated plumes are then studied using time-resolved electron diffraction. Laser ablation of liquids coupled with electron diffraction allowed the observation of radial distribution functions of two distinct phases of glycerol: gas and liquid. To our knowledge, this is the first time that a single sample source has successfully produced isolated and condensed phases for study by electron diffraction.

To my family.

Thoroughly conscious ignorance is the prelude to every real advance in science. - Sir. James Clerk Maxwell

Chapter 1

Introduction

Since the advent of the first optical lasers in the 1960s, laser-matter interaction has been the subject of intense research. The observed phenomena vary greatly depending on the different characteristics of the laser radiation, such as wavelength (λ_l), pulse length (τ_l), or the properties of matter, along with other environmental factors such as temperature and pressure. The interactions between lasers and matter are intricate and complex, encompassing many phenomena, including absorption, ablation, excitation, phase change, ionization, plasma generation, and most recently, the fusion of hydrogen atoms into helium. A particular area of research into the interaction of lasers with matter is focused on pulsed laser ablation (PLA). *Ablatio* is a Latin word meaning removal, and as the name implies, PLA is a light-matter interaction in which material is removed using a laser pulse. PLA is used in materials processing [1, 2], laser surgery [3, 4], analytical studies [5], and as a sample delivery mechanism [6–9]. This thesis encompasses research that integrates three seemingly unrelated fields with pulsed laser ablation: rheology, bubble physics, and time-resolved electron diffraction. The scientific field of rheology focuses on understanding how materials respond to applied forces, including their ability to deform and flow under different circumstances. Bubble physics is a vast field that involves the study of how bubbles form, grow, and collapse [10]. Bubbles are all around us. We encounter and notice bubbles from boiling water and dishwashing soap without giving them much thought. However, they have been the subject of curiosity of scientists for a long time [11]. Learning about bubbles can help us in many ways, from understanding new ways of synthesizing materials [12] to tackling erosion in mechanical parts [13, 14] to medical applications

[15–17].

Time-resolved electron diffraction is a scientific technique that uses electrons to study structural changes in materials over very short time scales, typically in the range of microseconds to femtoseconds. This technique allows scientists to follow the movement of atoms during chemical reactions, phase transitions, and rearrangements.

How are these four fields of science intertwined?

The research presented in this thesis involved the use of time-resolved brightfield imaging to capture intricate images of laser-ablated plumes of liquids in a vacuum. The resulting images are shown in Figure 1.1. Here, we investigate the behavior of these ablated plumes generated under a wider range of parameters than in previous studies [18, 19]. We observed a presumably novel laser-driven surface bubble at a particular ablation fluence and pressure window. To unravel the dynamics of these laser-driven free surface bubbles, we need concepts from the fields of PLA, rheology, and bubble physics. Finally, we demonstrate how these laser-driven plumes can be used to deliver samples of two different phases, liquid and gas, which can be studied using the technique of time-resolved electron diffraction [20]. The electron diffraction aspect is discussed in detail in Chapter 4 of this thesis.

Laser ablation of a liquid

As the laser pulses become shorter and more intense, extreme non-equilibrium conditions can be created due to their interaction with matter. Reviews discussing these nanosecond pulsed ablations in various materials[1] are available with references [22–24]. A recent review of the dynamics during femtosecond laser ablation can be found in Guo et al. [25], which mainly discusses the tools used to study these phenomena. A very comprehensive illustration discussing the qualitative influence of laser pulse duration (τ_l) and fluence in the case of metal ablation can be found in Shugaev et al. [24], as shown in Figure 1.2. Figure 1.2 illustrates the various processes that can occur in the system upon irradiation with a laser pulse in the parameter space spanned by pulse duration and fluence. The relevant parameter space for this work is indicated

---

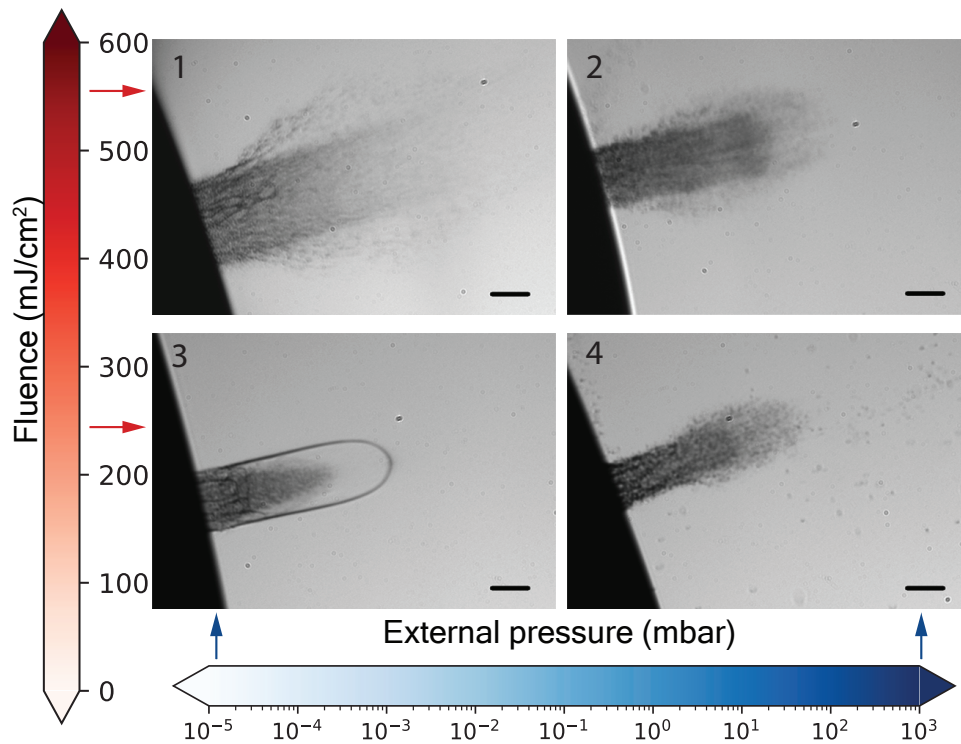[1]These include primarily metals, water, and other water-rich targets such as tissue.

Figure 1.1: Brightfield images of the liquid glycerol plume behavior at 2 μs after ablation laser incidence. Shown for different ablation laser fluences and external pressure conditions. The bubble (inset 3) is a previously unobserved phenomenon and exhibits a solid-like metastable state for liquid glycerol. Figure adapted from [21].

in the figure and deals with laser fluences of $100 - 600$ mJ/cm^2 at a pulse duration of about 400 picoseconds. Accordingly, we expect the dynamics to be driven primarily by phase explosion and spallation phenomena.

Phase explosion is a process in which the absorbed energy rapidly ($\tau_l < 1$ μs) heats a volume to temperatures above the boiling point, without allowing the heterogeneous nuclei[2] to expand in the way that normal liquid boiling does. At sufficiently high laser energy, the volume reaches the point of instability called the spinoidal temperature, which is very close to the critical temperature[3] of the liquid, and decomposes into

---

[2]Nucleation is a primary step during a phase change that occurs around certain instabilities (nuclei). This process can occur in two ways: heterogeneous nucleation, which occurs when pre-existing nuclei such as dust particles or dissolved gas are present in the liquid or solid, and homogeneous nucleation, which occurs due to local thermodynamic fluctuations in the absence of contaminants.

[3]The critical temperature of a substance is the temperature above which no amount of pressure will cause its vapor to condense into a liquid.
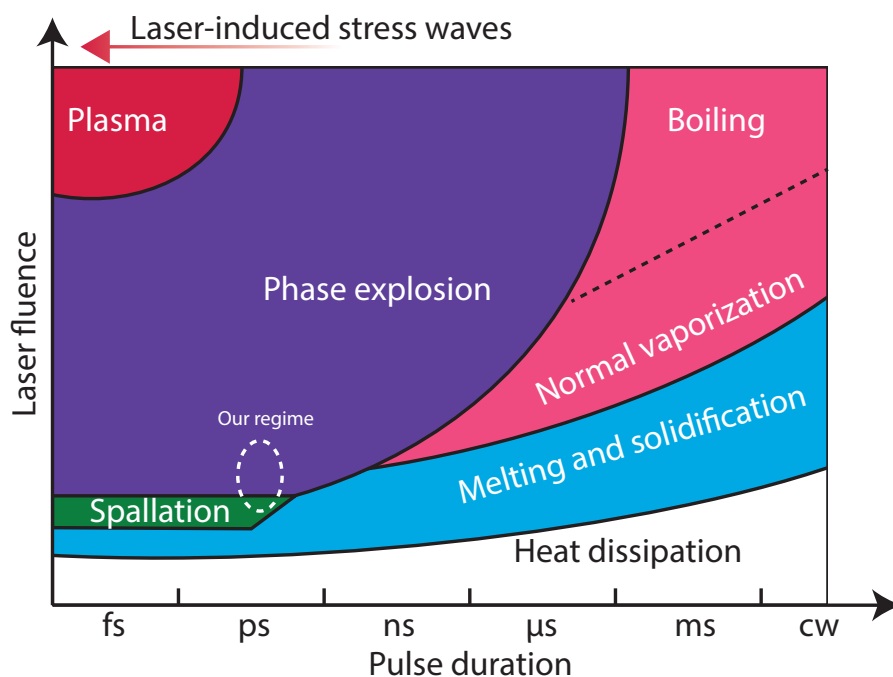
Figure 1.2: Influence of laser pulse duration and fluence in the case of ablation and resulting processes. Figure reproduced and modified from reference [24].

gas, vapor, and droplets. The phenomenon of phase explosion[4] has been extensively studied in ablation with water [26–29] and water-rich targets such as tissue [4, 22]. The use of mid-IR lasers, which can initiate laser ablation by means of phase explosion, has also shown promise in laser surgery [30].

In laser-induced or photomechanical spallation, the photomechanical stresses cause the material to fracture, ideally without undergoing a phase change. Pure mechanical means can also induce spallation without the generation of thermoelastic[5] stresses, and the majority of studies conducted in liquids have not used a laser to induce stresses [31, 32]. When it comes to laser-induced spallation, studies have focused on metals [33] or other solids [34, 35] and there are only a few cases of laser-induced spallation studies in a small molecule liquid such as water [36, 37].

---

[4]Phase explosion is also known as explosive boiling.

[5]The thermoelastic effect is a phenomenon in which a material undergoes deformation or changes in shape or dimensions when subjected to changes in temperature or vice versa.

A brief introduction to viscoelasticity

When a force is applied to a solid, it can deform or break, depending on the strength and direction of the force and the properties of the material. The amount and type of deformation depends on factors such as the composition of the material, its molecular structure, and the magnitude, direction, and duration of the applied force. Once the force is removed, the materials typically exhibit a complex response between two limiting cases: elastic or plastic. An elastic response occurs when the material returns to its original shape after the force is removed. Rubber bands and steel springs are examples of everyday objects that exhibit the property of elasticity. On the other hand, a plastic response occurs when the material permanently deforms and does not return to its original shape even after the force is removed.

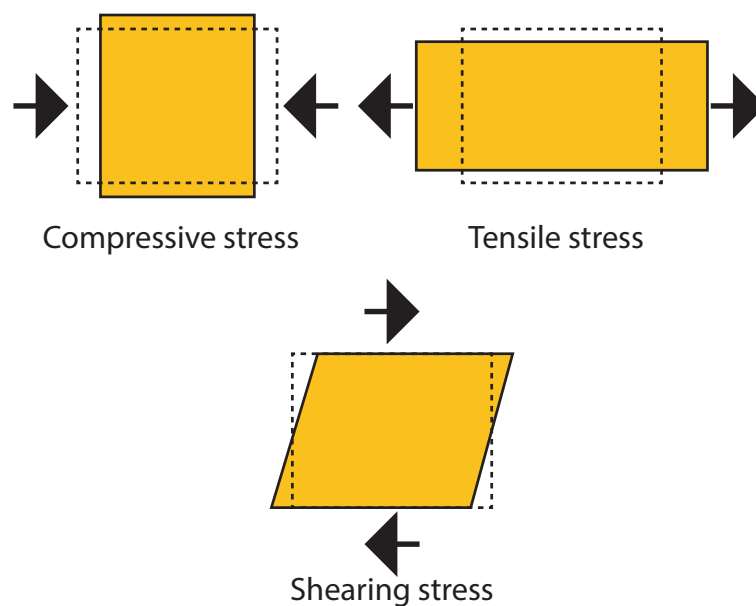
Figure 1.3: Illustrations depicting the behavior of materials under various deformations. The dotted rectangle depicts the original shape of the material. Arrows depict the direction of the applied force at the surface.

The study of elasticity involves examining how a material responds to three types of deformation: compressive, tensile, and shear. Compressive, tensile, and shear stresses

are types of forces that are present in an object during deformation, depending on the action of the force on that object, as shown in Figure 1.3. Compressive and tensile stresses are forces per unit area that act perpendicularly to the surface of an object, attempting to compress or stretch it. In contrast, shear stress is a force per unit area that acts parallel to the surface of an object, causing one surface to slide or displace relative to the parallel surface.

When it comes to liquids, we typically use the physical property of viscosity (η) to describe the response to deformation. When force is applied to liquids, such as water, we know that they will flow. The flow properties of liquids vary. For example, honey requires more force to flow than water. The property that accounts for this difference is viscosity. Honey ($\eta \approx 10$ Pa s) has a higher viscosity than water ($\eta \approx 10^{-3}$ Pa s) [38]. Viscosity is a measure of a fluid's resistance to deformation due to its inherent internal molecular interactions.

Viscosity and elasticity are fundamentally different, although both appear as responses to deformation. The dissipation or retention of energy can be used to further distinguish between viscosity and elasticity. When a force is applied to a viscous liquid, the energy is eventually dissipated as heat, unlike an elastic solid where the energy is stored and can be recovered [39].

For small molecule liquids such as water and glycerol, their viscosity is considered invariant to the strain rate, where strain is the relative displacement of particles in a body, excluding the motion of a rigid body itself[6]. Liquids such as water and glycerol are typically classified as Newtonian fluids (NF) and obey Newton's law of viscosity as follows,

$$\sigma_s = \eta \frac{dS}{dt} \tag{1.1}$$

where σ_s is the shear stress, η is the viscosity, and $\frac{dS}{dt}$ is the shear rate.

Materials that respond to external forces in a manner that is intermediate between the behavior of an elastic solid and a viscous liquid are known as *viscoelastic*. To study the viscoelastic properties of a material, dynamic mechanical analysis (DMA) is used, in which an oscillating strain is applied to the material and the resulting stress is measured[7].

For a material subjected to oscillatory strain at the frequency ω, the strain can be defined as $\epsilon = \epsilon_0 sin(\omega t)$, and the resulting stress can be written as $\sigma = \sigma_0 sin(\omega t + \delta)$,

---

[6]Strain can also be defined as the ratio of the initial dimensions of a body to the deformed dimensions of the body after an applied force.

[7]A more detailed discussion of this can be found in the Appendix B.

where δ is the phase lag between stress and strain. For an ideal elastic material, stress and strain are in phase with $\delta = 0$. For an ideal viscous material, the stress and strain are 90° out of phase (i.e., $\delta = \pi/2$). For a viscoelastic material, the response shows a parameter δ between the limits of $0 < \delta < \pi/2$.

The typical form of vibrational strain used to measure the viscoelastic properties of liquids using commercially available instruments is shear strain, and the behavior in these viscoelastic materials can be quantified using the shear modulus, which can be defined as the ratio of the shear stress (σ_s) to the applied strain (ϵ_s) as follows,

$$G(\omega) = \frac{\sigma_s}{\epsilon_s} \tag{1.2}$$

The presence of measurable shear elasticity at times longer than a short time window of nanoseconds ($\omega < $ MHz) is one way to distinguish between non-Newtonian and Newtonian fluids [38]. These non-Newtonian fluids may have some ability to store and recover shear energy[8].

What is rubber elasticity?

Following J. E. Mark, *rubber elasticity* can be operationally defined as high deformability with nearly complete recoverability [40]. For a material to display this type of elasticity, it must meet three molecular criteria: (1) the material must consist of polymeric chains, (2) the chains must be interconnected to form a network structure, and (3) the chains must possess a high degree of flexibility.

It is clear from these descriptions that a small molecule liquid such as glycerol does not meet any of these criteria. So, is it possible for liquid glycerol to behave like rubber?

What can we learn from bursting bubbles?

There is a great deal of scientific interest in bubble rupture. To give a few examples, aerosols produced during bubble rupture play an important role in a variety of processes, ranging from the very familiar flavor release of sparkling drinks [41] to the

---

[8]The internal work done in a body when externally applied stress causes it to deform, with the specific type of external stress, in this case being shear stress.

more globally impactful aerosol generation of ocean sprays [42]. Therefore, it can be very useful to understand the dynamics of bubble rupture.

The limiting velocity of the rim fracture for soap bubbles[9] was modeled independently in the early 1960s by Taylor [43] and Culick [44]. The equation relates surface tension and bubble thickness to rim fracture velocity and became known as the Taylor-Culick velocity (TCV). Since its derivation, it has been widely used to describe the fracture mechanisms of liquid bubbles and sheets. The equation balances the energy of the disappearing surface with the kinetic energy of the moving rim, resulting in a final form as follows,

$$v_{TC} = \sqrt{\frac{2\sigma_{ST}}{\rho\delta}} \qquad (1.3)$$

where σ_{ST} is the surface tension of the liquid, ρ is the density of the liquid, and δ is the thickness of the retracting film.

In our case, as we will discuss in detail, the expected TCV is 20 times smaller than the measured one, and this discrepancy cannot be explained by the effects of surface tension alone. Similar deviations are only observed in the case of elastic bubbles [45], where the introduction of elasticity into the bubble resulted in a 30-fold increase in the fracture retraction velocity. In our laser-induced bubble, the fracture velocity analysis suggests shear modulus values comparable to those of rubber, which is corroborated by an entirely different analysis looking at bubble growth. So, how can glycerol exhibit elastic properties similar to those of rubber with fundamentally different interatomic interactions?

Can liquid glycerol behave like rubber?

As a prelude to a possible explanation, I quote Markus Reiner[10] here,

States of matter are a matter of time(s)

The importance of Reiner's notion is evident even in Newtonian fluids such as glycerol and water, whose state can vary depending on the time frame of observation,

---

[9]In general, this is also true for non-viscous (inviscid) films, but high-viscosity films deviate from linear fracture diameter growth.

[10]Reiner along with Eugene C. Bingham coined the term Rheology for the scientific field concerned with the flow of matter.

appearing either liquid-like or solid-like, even with no change in temperature, density, or pressure.

By introducing a diffusion relaxation time τ, an average period between two successive rearrangements of neighboring particles (pink in Figure 1.4)[11] surrounding a reference particle (violet in Figure 1.4), Frenkel showed that the response of a liquid is indistinguishable from that of an amorphous solid for $t < \tau$ [46]. In the case of small molecule liquids such as water and glycerol, $\tau = \tau_m$. The molecular relaxation time (τ_m) is generally evaluated by Einstein's formula as follows [47],

$$\tau_m = \frac{\Delta^2}{6D_{sd}} \tag{1.4}$$

where Δ is the inter-particle[12] distance and D_{sd} is the self-diffusion coefficient. The value of τ_m is typically between 1 ps to 1 ns for Newtonian fluids [48][13].

In particular, Frenkel's microscopic description implies that, below τ_m, Newtonian fluids can transmit both compressional and shear waves, just as in the case of solids. However, as time passes and the local molecular environment is rearranged and relaxed, NFs transition to the viscous behavior we experience in our daily lives, where they can no longer support shear waves.

However, subsequent experiments have contradicted Frenkel's view. In a 1986 review, Daniel D. Joseph [50] outlines the historical development of the idea that so-called Newtonian fluids can have varying degrees of elasticity and viscosity. Some very recent studies [51, 52], along with earlier work by D.D. Joseph et al. [53–55], and Derjaguin et al. [56] have challenged this paradigm. They have shown that confined fluids can have measurable shear elasticity well beyond their molecular relaxation times, even at $\omega \rightarrow 1$ Hz. However, direct observation of the manifestation of elasticity in NFs during flow beyond their molecular relaxation times is rare and is typically measured only by indirect methods of dynamic mechanical analysis [52, 56].

During pulsed laser ablation, the liquid experiences extreme strain rates in response to the stresses generated. The behavior of fluids at these extreme strain rates is a poorly understood area. In the limited literature available to describe these systems, they are known to deviate from the expected Newtonian behavior [57, 58]. It has been shown that at high strain rates, especially in the case of glycerol, the viscosity appears to depend on the strain rate, indicating an apparent non-Newtonian behav-

---

[11]In our case, these particles can be thought of as molecules.

[12]Inter-molecular in our case.
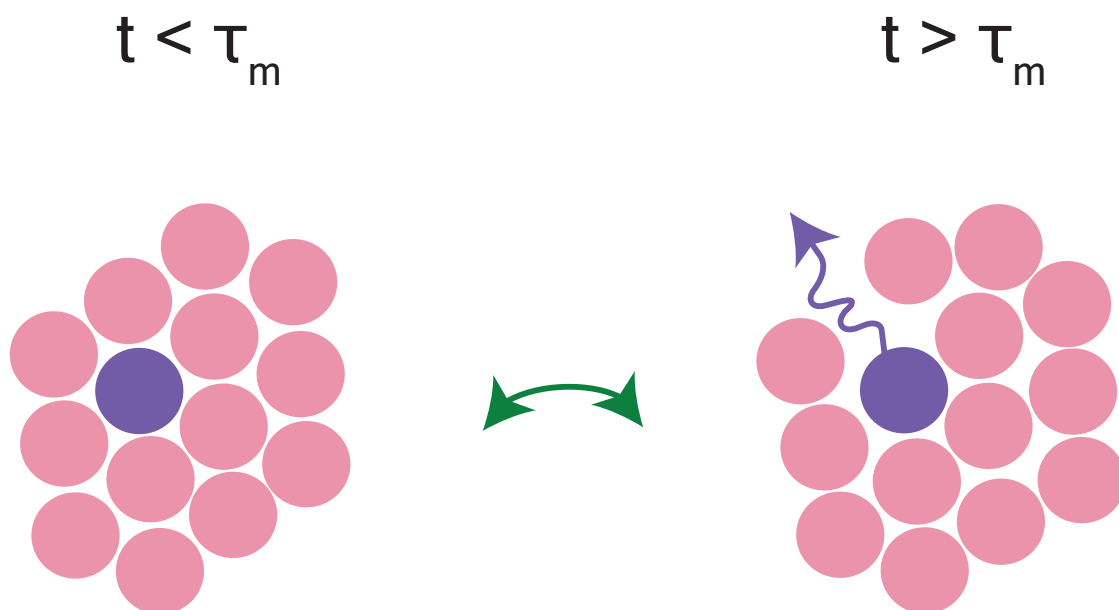
[13]And references therein.

Figure 1.4: The figure represents the molecular jumps of a reference molecule with respect to its neighboring molecules. At times $t < \tau_m$ the liquid practically acts like an amorphous solid. Figure reproduced from reference [49].

ior [47]. As we discussed earlier, this non-Newtonian behavior can lead to a material with the ability to store and recover elastic energy [38], as in the case of rubber.

In conclusion, a straightforward answer to the question *"Can liquid glycerol behave like rubber?"* is not elementary. However, given all the unexpected behaviors[14] shown by liquid glycerol [47, 52, 59], it is certainly possible, and we may have captured such a rare occurrence. For a Newtonian fluid to be elastic beyond τ_m, solid-like long-range correlations[15] in the liquid is required, which challenges our current understanding of the liquid state [61].

---

[14]That is, strain rate dependent viscosity and solid-like ability to sustain shear waves.

[15]Paraphrasing Robert. M. White [60]: In systems that exhibit long-range order, the value of a property at one point is correlated with its value at a point infinitely far away. Long-range order is observed in many forms in nature, with the most prominent example being crystalline solids, where the mass density exhibits this property. Unlike in liquids, where atomic motion leads to density fluctuations, atoms in a crystal occupy regularly spaced locations, leading to density-density correlations that persist over long distances.

1.1. Thesis overview

This thesis charts a scientific journey, commencing with the construction of an in-vacuum laser ablation and imaging system, followed by the analysis of the unusual plumes, and culminating in the utilization of these plumes as a sample delivery mechanism. As most of the discussion requires an appreciation of the unusual plumes created during the laser ablation, the dissertation is divided into two parts and follows a somewhat unconventional format.

Part 1 consists of Chapters 2 and 3, each dealing with time-resolved imaging aspects of the research. Chapter 2 focuses on the production of laser-ablated plumes in vacuum and their investigation using a brightfield imaging setup. This chapter also presents findings on the behavior of the produced plumes with respect to ablation fluence and pressure variations for selected liquid samples. In Chapter 3, we dive deeper into the study of laser-induced bubble formation by these liquids within a specific pressure and fluence range. Our analysis includes the exploration of possible explanations for the observed bubble formation phenomenon through the study of bubble growth and fracture dynamics.

Part 2 consists of Chapters 4 and 5, which focus on time-resolved electron diffraction aspects of the research. Chapter 4 highlights the need for a new sample delivery method for performing time-resolved electron diffraction and provides the essential theoretical framework for analyzing the data obtained from gas-phase and liquid-phase electron diffraction. Chapter 5 presents a proof-of-concept experiment performed with a table-top time-resolved electron diffraction instrument. Specifically, this chapter describes the measurement of radial distributions for gaseous and liquid glycerol derived from the ablated plumes.

1.2. Project contributions

Collaboration is a fundamental aspect of scientific work in the modern era, and this dissertation is no different. This thesis consists of experimental and theoretical work performed by myself and a group of other scientists at the Max Planck Institute for the Structure and Dynamics of Matter, with regular supervision by Dr. Sascha Epp. The brightfield imaging instrumentation was built and the measurements were set up and performed by myself and Dr. Zhipeng Huang. Electron diffraction measurements were performed with the assistance of Dr. Stuart Hayes. The sample delivery system was designed and developed with the help of Hendrik Schikora and Djordje Gitaric. All analyzes presented in Chapters 3 and 4, unless otherwise stated, were performed by me with input from Dr. Epp and Dr. Huang.

Part of the analysis of the data from the electron diffraction experiment in Chapter 5 was performed by Dr. Huang. Dr. Epp performed the finite element modeling with hypothetical elastic material to explain the elastic behavior of the bubble described in the Appendix C. Dr. Hayes performed the deduction of the geometry of the liquid glycerol using molecular dynamics techniques explained in the Appendix D.

Part I

Chapter 2

Time-resolved imaging of laser-driven plumes in vacuum

In this chapter, I describe our custom-built instrumentation for laser ablation of liquids in vacuum with a time-resolved far-field brightfield microscope to observe plume formation. Using this apparatus, we investigated the effect of laser fluence and vacuum conditions on the generated plumes and their dynamics.

2.1. Experiment design

The central element of our apparatus is the vacuum chamber, which allows us to study plume dynamics under various external pressure conditions ranging from 1 bar to 10^{-6} mbar as shown in Figure 2.1). The chamber has one view port for the ablation laser (red), one for the flash lamp pulse (blue), and two for two microscopes, one for observing the ablation event and one for monitoring the sample. There are also flanges to connect the turbo pump and the vacuum gauge.

The studies discussed in this thesis used a picosecond ($\tau_l = 400 \pm 50$ ps) mid-IR ($\lambda_l = 2.94$ μm) laser from Light-Matter Interaction, Canada as the ablation source.
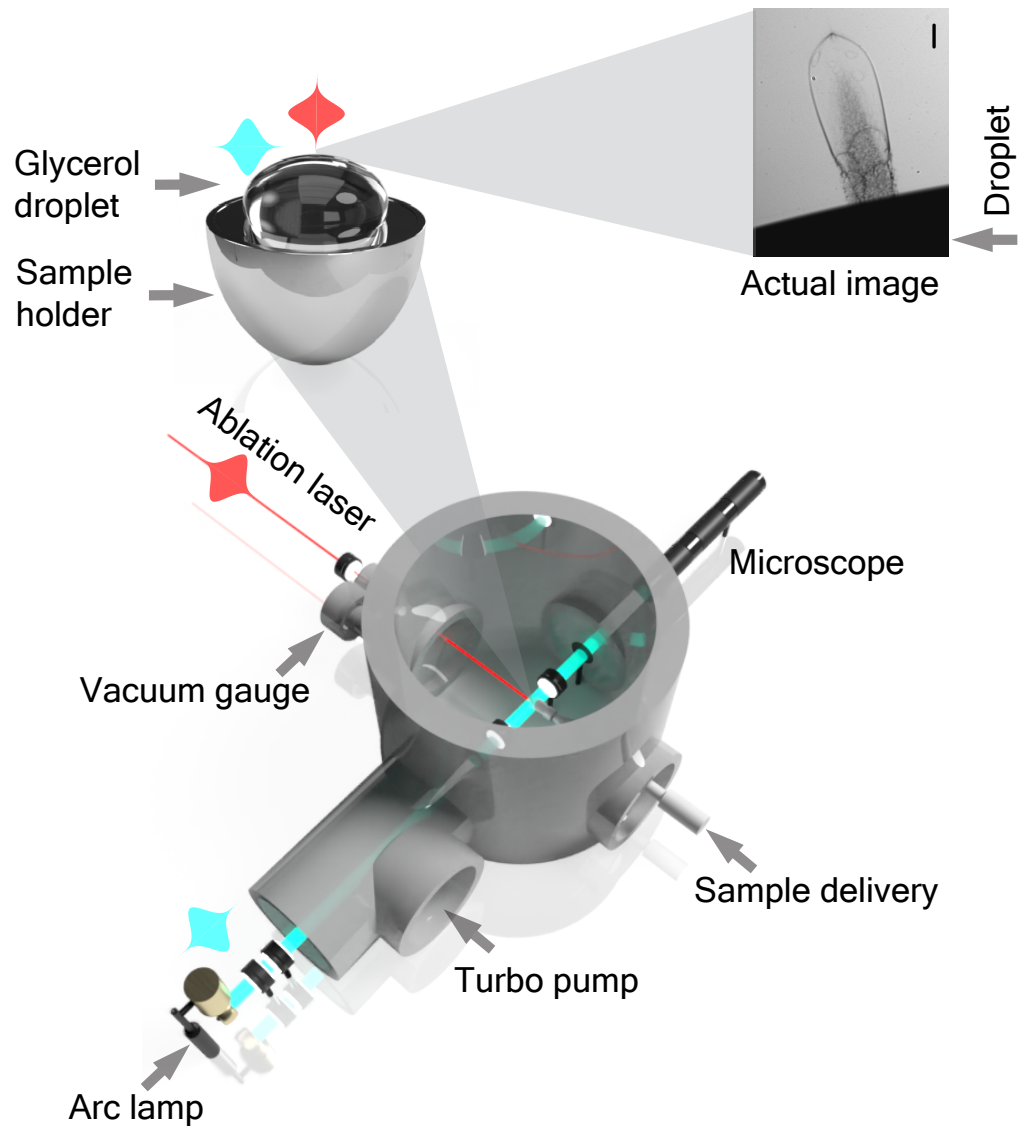
Figure 2.1: Schematic drawing of the experimental setup for imaging the laser-ablated plumes in vacuum. The ablation laser (red) and the imaging path (light blue) are orthogonal to each other. The first inset (top left) shows the plume and pump-probe interaction directions. The second inset (top right) shows the recorded image of an ablation plume. Not to scale. Figure adapted from [21].

Here, the energy transfer from the laser pulse into all the liquids discussed (see Figure 2.2) is facilitated by resonant excitation of the O-H bond stretching modes around 2.94 μm (3400 cm^{-1})[1]. The IR absorption spectra of the liquid samples used are shown in Figure 2.3. The wavelength of the ablation laser is in the region of strong absorption for both water and glycerol and moderately good absorption for the ionic liquid used in the study. Efficient and rapid redistribution of ablation laser energy is facilitated by the strong interaction between the molecules through hydrogen bonding. An additional benefit of the efficient energy transfer into the sample is that the fluences required to initiate ablation are significantly lower compared to other ablation lasers [28]. The reduction in ablation laser fluence also lowers the likelihood of plasma formation and other enhanced nonlinear optical excitation processes, resulting in a reduced molecular modification during the ablation[2]. Nanosecond and picosecond mid-IR ablation with a specific focus on a wavelength of about 3 μm has previously been studied with a focus on laser surgery [30] and mass spectrometry [63]. However, studies that focus on the dynamic of plumes formed in vacuum are scarce [19].

2.1.1. Sample delivery

One of the critical parts of this study is getting the liquid sample into the vacuum. Because of the high vapor pressure, most small molecule liquids are not good candidates for a preliminary study. Water begins to boil below 32 mbar[3] and thus can only be studied under ambient conditions without extensive engineering of the sample delivery mechanism. However, glycerol ($>$ 99.5%, Sigma-Aldrich), with its low vapor pressure and strong absorption around 2.94 μm, is an ideal system to study. Our search for another liquid to study under vacuum conditions led to an ionic liquid (Tris-(2-hydroxyethyl)-methylammonium-methylsulfate), shown in Figure 2.2c, which has a reasonable absorption of around 2.94 μm and an even lower vapor pressure. An accurate measurement of the vapor pressure of the ionic liquid used here is not avail-

---

[1]Marked in Figure 2.3 with a gray dashed line.

[2]Including destruction and potential charging of the liquid. Eliminating the possibility of charging is important because liquids exposed to high voltage differences can exhibit elasticity [62].

[3]At a temperature of 25° C [64].

(a) Water molecule

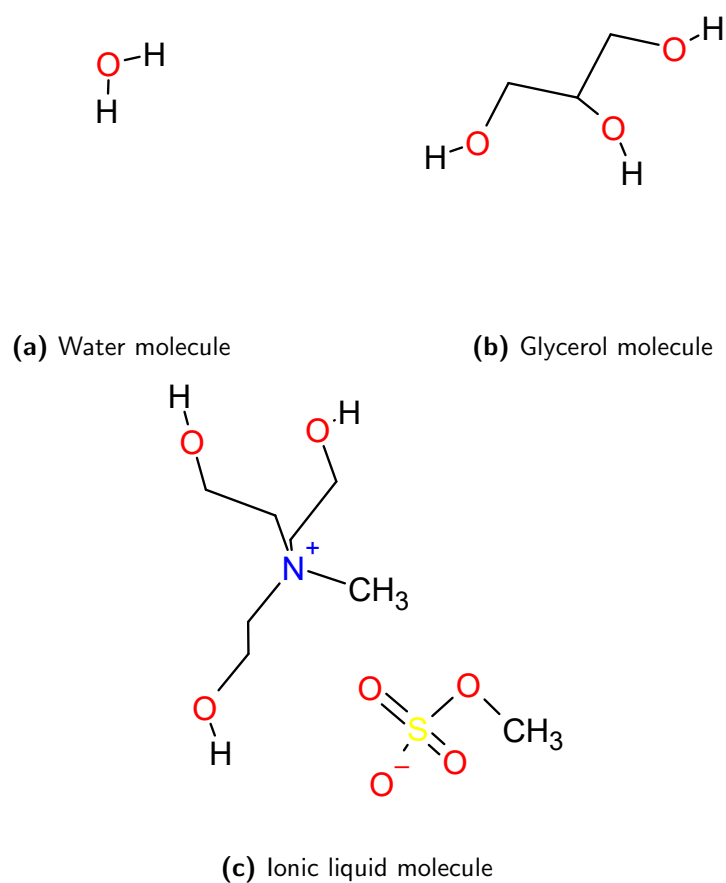**(b)** Glycerol molecule

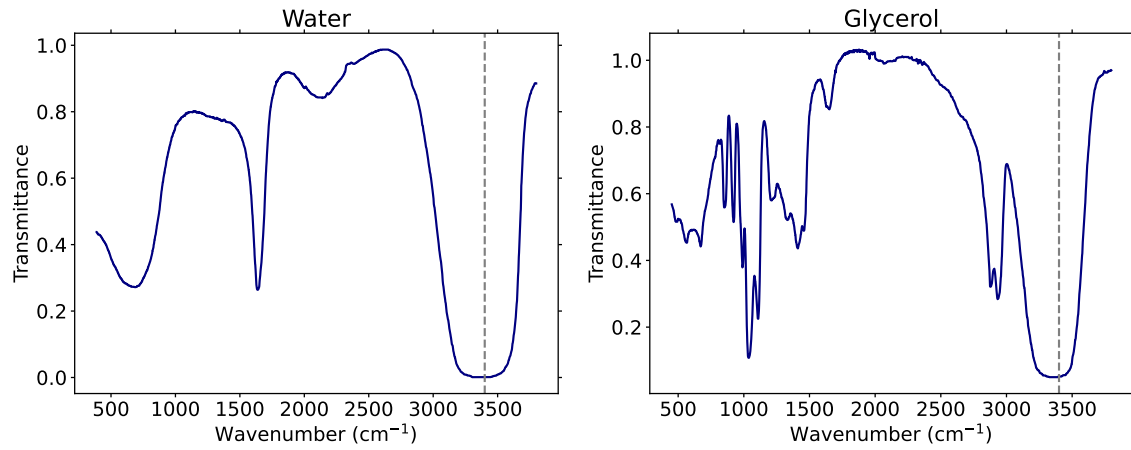

(c) Ionic liquid molecule

Figure 2.2: Molecular structures of the sample materials that have been the subject of this study. The OH groups present are strong absorbers of the 2.94 μm ablation laser. Based on molecular structures available at `https://pubchem.ncbi.nlm.nih.gov/`.

(a) IR absorption spectrum - Water, Data available at `https://webbook.nist.gov/`.

(b) IR absorption spectrum - Glycerol, Data available at `https://webbook.nist.gov/`.
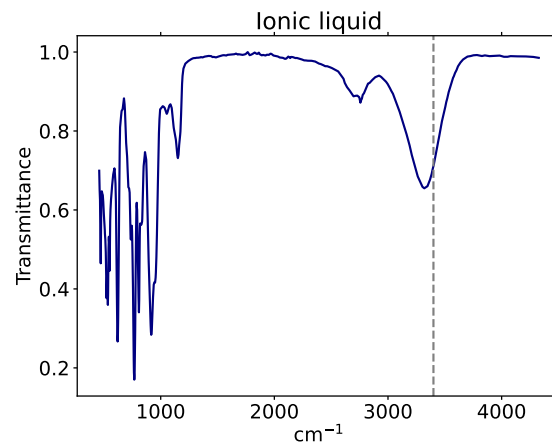
(c) IR absorption spectrum - Ionic-liquid, Data from the vendor: `https://www.sigmaaldrich.com/DE/de`.

Figure 2.3: The dotted gray line corresponds to the ablation laser wavelength(2.94 μm $\approx$ 3400 cm^{-1}).

able. However, a qualitative estimate was obtained by keeping a droplet in a vacuum ($< 10^{-6}$ mbar) for several days and comparing its evaporation with that of glycerol. To introduce liquids into the vacuum, we used a solid stainless steel hemisphere. It is magnetically attached to a handle (see Figure 2.4) for easy removal and replacement. The hemisphere can also be manually rotated from the outside for precise positioning of the liquid droplet relative to the ablation laser and imaging path. The use of a

Figure 2.4: Handle used to rotate the sample droplet delivered into the vacuum.

rotating handle, shown in Figure 2.4, makes it easy to change the ablation site on the glycerol droplet without complex engineering. Glycerol and ionic liquid are carefully dropped onto the surface of the steel ball (see Figure 2.5) using a syringe and needle before the chamber is closed and pumped down using first a scroll pump (Edwards Vacuum, UK) and then a turbo pump (Pfeiffer Vacuum, Germany). In no more than
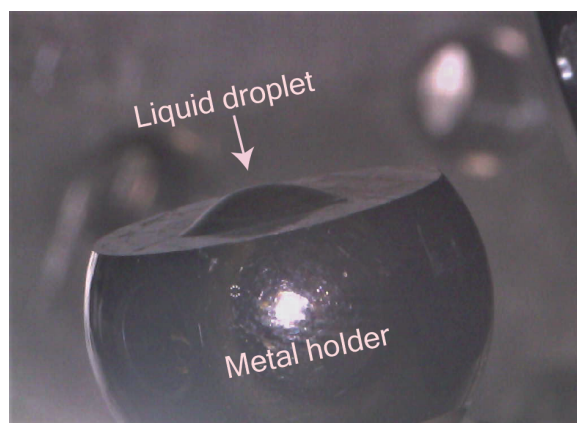

Figure 2.5: Hemispherical steel ball with the liquid sample inside the vacuum chamber, viewed from the top of the chamber.

five minutes, a vacuum of 10^{-5} mbar will be reached. A vent valve can control the

vacuum and is actively monitored by a vacuum gauge (Pfeiffer Vacuum, Germany). One drop of glycerol or ionic liquid is sufficient for a few thousand ablation shots.

2.1.2. Brightfield imaging

As shown in Figure 2.1, a discharge lamp flashlight source (Nanolite, Germany) with a pulse duration of about 12 nanoseconds and a broadband white spectrum was used as the illumination source. A collector lens ($f = 60$ mm) first collects light, and then a field lens ($f = 400$ mm) focuses the beam. An iris is placed at the focal point to shape the beam. The beam was then condensed by a condenser lens ($f = 80$ mm). The illumination path was adjusted so that the plume was in the focal plane of the condenser for maximum contrast. An objective lens with a focal length of 65 mm was used to image the plume. The resulting image was further magnified using an Optem Fusion microscope (Qioptiq, USA) with a focal length of 200 mm and a tube lens to adjust the magnification. The image was then routed to a monochrome CCD camera (DMK23U274) from Imagingsource, Germany.

Camera calibration

Image calibration is performed using a Dyno-lite calibration card. Each pitch in the calibration card is 200 μm. Thus, by imaging the reference scale under the exact conditions (same magnification and sample position), we will be able to deduce the true dimensions of the plume. To accomplish this task, it is necessary to determine the exact dimensions of the pixels within the image. We can do this using existing commercial software, such as ImageJ, which allows us to draw a line between the scales and then measure its pixel length on the calibration card. Once we have an estimate of the true dimensions corresponding to a pixel, the value can be accurately scaled to the real world values. There is inherent uncertainty in this approach due to the three-dimensional nature of the plume and the fact that the calibration card is a flat sheet, which is unavoidable and can lead to small errors in the plume dimension

calculation.

2.1.3. Ablation laser

The ablation laser was passed through a spatial filter to improve beam quality and then directed to the ablation spot by a 300 mm lens located outside the chamber. Additionally, a 100 mm lens is used to achieve higher fluences. In the case of ionic liquids, higher fluences are required for ablations, and to achieve this, the lens was placed inside the chamber without any other changes to the ablation path.

The laser power was varied by inserting different neutral density (ND) filters into the beam path. The laser power is measured both outside the chamber and at the sample position to calculate the fluence used for the measurements. There is a 35% energy loss between the laser power measurement outside the vacuum chamber and the measurement at the sample position. The energy loss can be attributed to two mirrors, a lens, and a view port through which the ablation laser must pass before reaching the sample position. A photodiode was used to monitor the pulse energy variations of the ablation laser from shot to shot by collecting stray light from the mirrors.

The repetition rate of the laser is 1 KHz. However, we cannot perform the measurements at this frequency due to the limitations of the nanosecond flash lamp, which has a maximum allowable repetition rate of 10 Hz. There is also the possibility that the liquid will boil as a result of the build-up of temperature from repeated ablations without a window for thermal dissipation. Therefore, most of the measurements were performed at a repetition rate of 1 Hz, with occasional use of a 10 Hz repetition rate[4]. The repetition rate was controlled by a delay generator (Quantum Composer Inc., USA) that controlled the shutter system built into the ablation laser.

Depending on the shutter opening time, we can choose to use a single pulse or a bundle of multiple pulses. To ensure that the sample we are probing is indeed liquid, we used a format in which a pulse (1 ms before the reference pulse) induces prior ablation at the same fluence. The rationale behind this design choice was that the

---

[4]The use of 10 Hz repetition rate will be explicitly mentioned when presenting the data.

thermal energy deposited during the first ablation (which we will call the pre-pulse) keeps the liquid above its melting point [5]. A detailed discussion of this can be found in Section 2.2.2.

2.1.4. Focus beam diameter

To interpret the ablation measurements, it is critical to accurately determine the fluence of the laser ablation. With our ablation chamber design, we could not implement a system that would allow us to frequently measure the focal spot for different laser energies that we used.

The focus beam diameter was determined using the beam profiler (WinCamD, DataRay Inc.) with a sensor size of 8.16 mm $*$ 10.88 mm and a pixel size of 17.0 μm. The sensor was placed in front of the focusing lenses (100 mm and 300 mm) in the position of the sample. By moving the sensor axially using a delay stage, the smallest beam diameter corresponding to the focal spot can be obtained. Several ND filters have been added to the sensor to ensure that there is no saturation, which could potentially lead to errors and sensor malfunction. The ablation laser has a rather large M^2 value[6], which results in a somewhat poor beam profile and weak focusing. In our case, this results in a 139 μm FWHM beam diameter and 236 μm $1/e^2$ diameter for a 300 mm focusing lens. For the 100 mm focusing lens, the FWHM and $1/e^2$ beam diameters are 79 μm and 134 μm, respectively.

The ablation laser pulse profiles are shown in Figure 2.6, which can produce plumes with different characteristics and sizes depending on the fluence. The illustrative perspective of the plume from top based on the base diameter value for a fluence of 206 mJ/cm^2 and the horizontal and vertical profiles of the Gaussian intensity distributions of the measured ablation beam focal spot profile are shown in Figure 2.7.

---

[5]Glycerol has a melting point of about 291 K.

[6]Beam Propagation Ratio, is a value that indicates how close a laser is to being a perfect Gaussian, which in turn determines how small a beam waist can be focused.
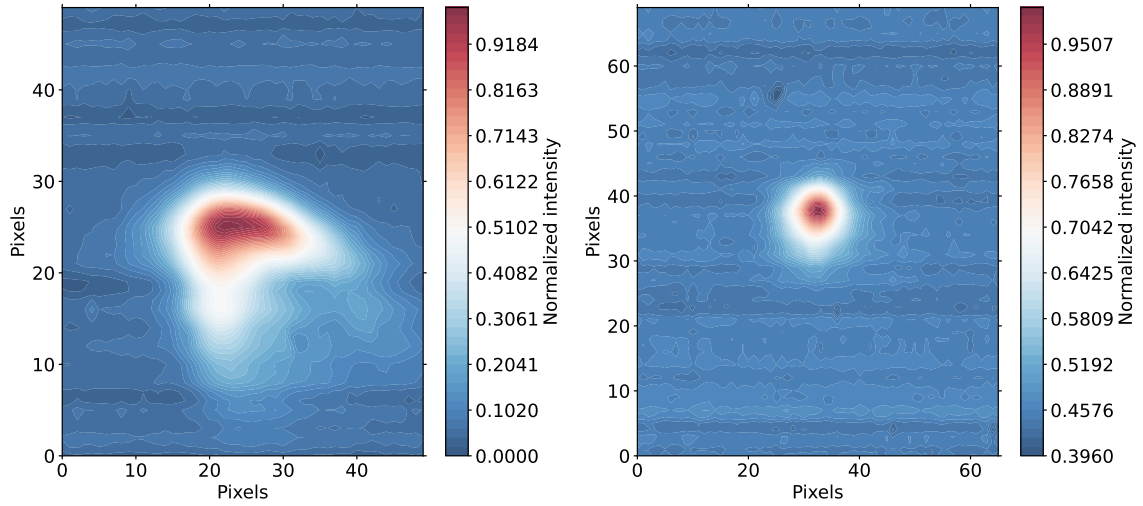
(a) Beam profile slightly out of focus for 300 mm focusing lens.

(b) Beam profile measured in focus for 300 mm focusing lens.
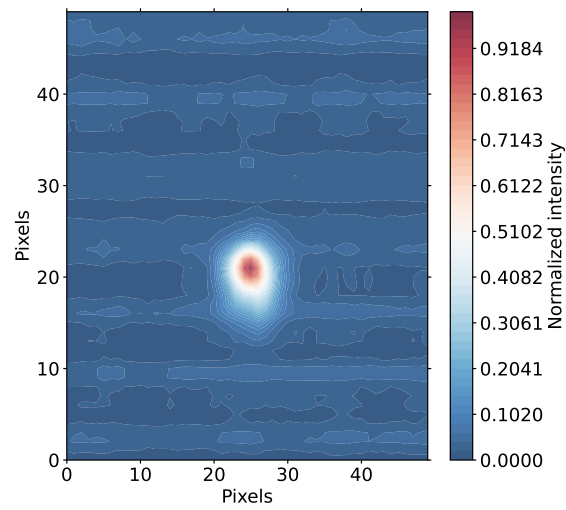
(c) Beam profile measured in focus for 100 mm focusing lens.

Figure 2.6: Beam profiles measured out of focus and in the focus of the ablation laser with two different focusing lenses used for the project.
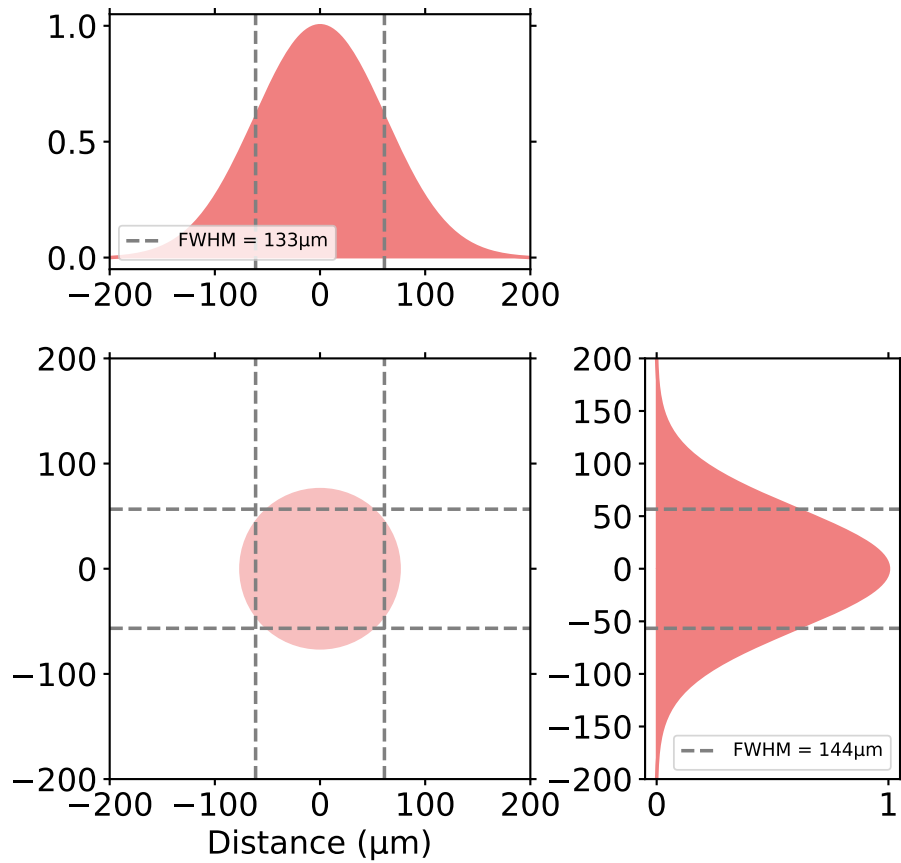
Figure 2.7: Schematics of the laser driven plume (base diameter of 150 μm, for an ablation fluence of 206 mJ/cm^2) top view and the interacting spatial profile at the focal spot of the laser. The gray dashed lines correspond to the sigmas for the laser profile measured in the corresponding directions.

2.1.5. Laser energy and peak fluence calculations

For various calculations performed throughout this thesis, we need ways to describe the ablation laser energy and peak fluence. The analytical equation to describe the peak fluence for a Gaussian pulse is as follows [65],

$$F_{peak} = \frac{2E_p}{\pi r_e^2} \tag{2.1}$$

where E_p is the pulse energy, r_e the beam radius is the distance from the beam axis where the intensity drops to $1/e^2$ ($\approx 13.5\%$) of the maximum value. The peak fluence F_0 is the maximum energy density per unit area at the center of the beam. The peak fluence calculated by numerical integration was in agreement with the above estimate. Equation 2.1 was used throughout the thesis to determine the peak fluence of ablations.

The energy deposited on the bubble during surface bubble formation (described in Section 2.2.2) in glycerol is another important quantity to consider. To determine E_{bubble}, we derive the energy deposited on a surface with a base radius, r_{bubble}.

$$E_{\text{bubble}} = \int_0^{2\pi} \int_0^{r_{bubble}} F(r,\theta)d\theta dr \tag{2.2}$$

Where average r_{bubble} for different ablation pulse energy is shown in Table 2.1.

Total pulse energy (μJ)	Avg. bubble base radius (μm)	Pulse energy on bubble (E_{bubble}) (μJ)
53 ± 1	78 ± 4	43 ± 7
45 ± 1	76 ± 3	36 ± 5
38 ± 1	65 ± 2	27 ± 4

Table 2.1: Bubble base radius for different pulse energies and the effective energy deposited onto the bubble calculated according to Equation 2.2.

The inaccuracies in the calculations are primarily due to the measurement errors associated with each individual quantity. The average power measurement has a relative error of about 2%[7], and is propagated to the total pulse energy error. For

[7]Pulse to pulse variation is discussed later in this chapter.

the peak fluence calculations, the relative error in the $1/e^2$ radius estimate (2%) is also propagated, resulting in a final relative error of δF of F of about 5%. When calculating the pulse energy on the bubble, an additional error from the bubble base radius calculation ($\approx 5\%$) must be taken into account, resulting in a total relative error of about 15%.

Measured avg. power outside the chamber (mW)	Avg. power at the sample (mW)	Total pulse energy (μJ)	Peak fluence (mJ/cm^2)
Water, Glycerol ablation: Phase explosion regime (300 mm, $\frac{1}{e^2}$ radius = 118 μm)			
184	120	120 ± 2	549 ± 25
Glycerol ablation : Bubble regime (300 mm, $\frac{1}{e^2}$ radius = 118 μm)			
81	53	53 ± 1	242 ± 11
69	45	45 ± 1	206 ± 9
58	38	38 ± 1	174 ± 8
Ionic liquid ablation (100 mm, $\frac{1}{e^2}$ radius = 67 μm)			
81	53	53 ± 1	752 ± 34
26	16.9	16.9 ± 0.4	241 ± 11

Table 2.2: Ablation energies and peak fluences used in this thesis.

2.1.6. Synchronization

Accurately capturing the temporal evolution of the ablated plume requires precise synchronization of the timing of all instruments. The procedure used to achieve this is described below. The flash lamp was triggered using a photodiode signal from the ablation laser, where we were able to introduce a delay at the user's discretion using a delay generator (Quantum composer Inc., USA). The ablation laser also triggered the camera to capture the ablation event during its exposure. The camera had a

minimum exposure time of 100 μs, so the triggering process ensured that the ablation event was captured in the middle of the time window. Two photodiodes were used to determine the exact delay between the ablation laser and the flash lamp. An oscilloscope (Keysight Technologies, Germany) was used to collect these photodiode signals from which the delay values were calculated. Each image is stored with a time stamp, the ablation laser amplitude as measured by the photodiode, and the corresponding delay value.

2.2. Data and observations

Ablation of water, glycerol, and the ionic liquid was performed under ambient and various vacuum conditions[8] for various laser fluences. Each image presented in this section shows a plume resulting from a single ablation event at a given time delay. When interpreting the time series of ablation images such as those shown in Figure 2.8, it is important to keep in mind that only one image is taken per ablation. The series of images is more representative of an ablation than of an actual ablation event. Several images were taken for each delay to ensure reproducibility, and the images shown here were manually selected from said collection.

2.2.1. Water

Water has been the subject of extensive study among our sample liquids due to its importance in various scientific fields. Many studies have investigated the ablation of water with 2.94 μm lasers at different fluences and pulse lengths [4, 28]. Figure 2.8 shows a selected set of photographs taken at different time delays, representing the temporal evolution of the water plume ablated by the laser. At the fluence used here (about 550 mJ/cm^2), we observe mainly phase explosion. After the ablation, vapor and water droplets follow a leading shock front. The observed behavior of the plumes is consistent with previous studies [28, 66].

---

[8]Only glycerol and the ionic liquid were ablated under vacuum.

(a) 500 ns

(b) 1 μs

(c) 1.5 μs
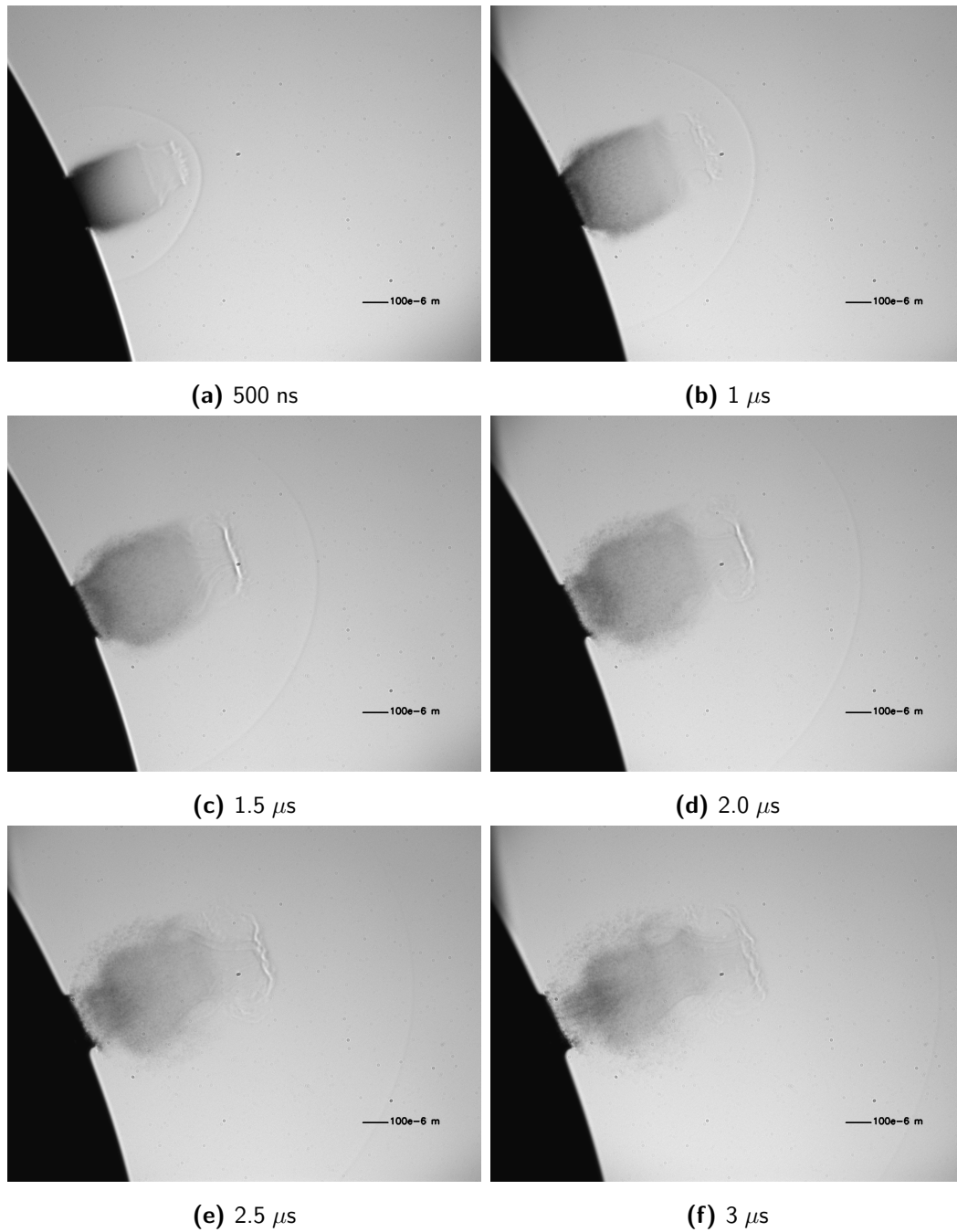
(d) 2.0 μs

(e) 2.5 μs

(f) 3 μs

Figure 2.8: Photographs of water plumes produced by the ablation laser with a peak fluence of 549 ± 25 mJ/cm^2 in ambient conditions (air and room temperature) at different delays. The black scale bar corresponds to 100 μm.

2.2.2. Glycerol

Glycerol is an important small molecule of interest in a biological context [67, 68]. As it is part of lipids, such as glycerides and phospholipids. The low vapor pressure of about 2.5×10^{-4} mbar at 298 K [69] makes glycerol an ideal sample to study under vacuum using our ablation technique.

Before presenting the results of our study, it is worth mentioning two previous laser ablation studies in glycerol. Fan et al. ablated glycerol with different fluences as well as with different IR wavelengths ($\lambda_l = 2.8 - 3.6$ μm, $\tau_l = $ 5 and 100 ns, $F_{peak} = 200 - 300$ mJ/cm^2) under ambient conditions [18], and Leisner et al. performed glycerol ablation under vacuum conditions (with relatively higher fluences suitable for reaching the ion detection threshold for mass spectrometry), their experiments were at $\lambda_l = 2.94$ μm, $F_{peak} = 280$ mJ/cm^2, $\tau_l = 6$ and $100 - 120$ ns [19]. These studies do not fully meet the stress confinement criteria of our ablations. Nevertheless, the plume behavior driven by the phase explosion as seen in Figure 2.9 is qualitatively similar to those in these earlier studies [19].

A selected set of photographs taken at different time delays for liquid glycerol ablation under ambient conditions is shown in Figure 2.9. It is similar to the evolution of the water plume shown in Figure 2.8 as a result of the phase explosion being a dominant factor.
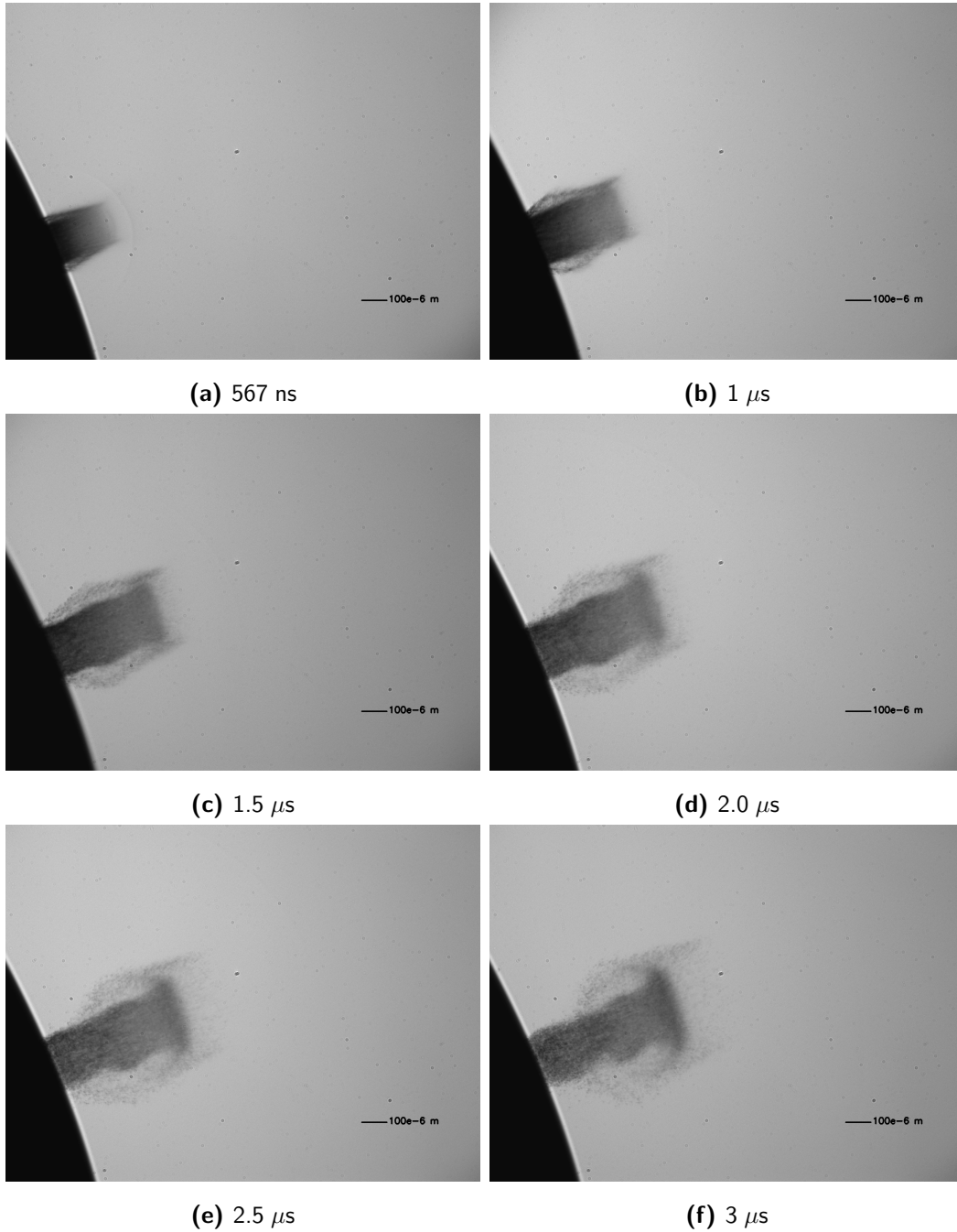
(a) 567 ns

(b) 1 μs

(c) 1.5 μs

(d) 2.0 μs

(e) 2.5 μs

(f) 3 μs

Figure 2.9: Photographs of glycerol plumes produced by an ablation laser fluence of 549 ± 25 mJ/cm^2 under ambient conditions (air and room temperature). The black scale bar corresponds to 100 μm.

Pre-pulse influence

Figure 2.10 shows two plumes with different distributions of ablated material produced by the same fluence. The only difference between them is that the ablation event in Figure 2.10b was preceded by another pulse of the same fluence millisecond earlier. The difference in the ablated material distribution can be attributed to the local temperature change and fluctuations in the liquid droplet surface following the pre-pulse ablation.

Glycerol has a melting point of 291-293 K[9], but it is known to exist in a supercooled liquid form at much lower temperatures (with a glass transition temperature of 190 K). There is evidence that glycerol exhibits a non-Newtonian behavior at these supercooled temperatures due to heterogeneity[10] [70, 71].To ensure that we are working with liquid glycerol above its supercooled state, we implemented a preheating pulse that temporarily raises the local liquid temperature. Additionally, this pre-pulse is believed to create a fresh sample surface prior to each recorded plume, resulting in improved bubble stability and quality as visible in Figure 2.11.
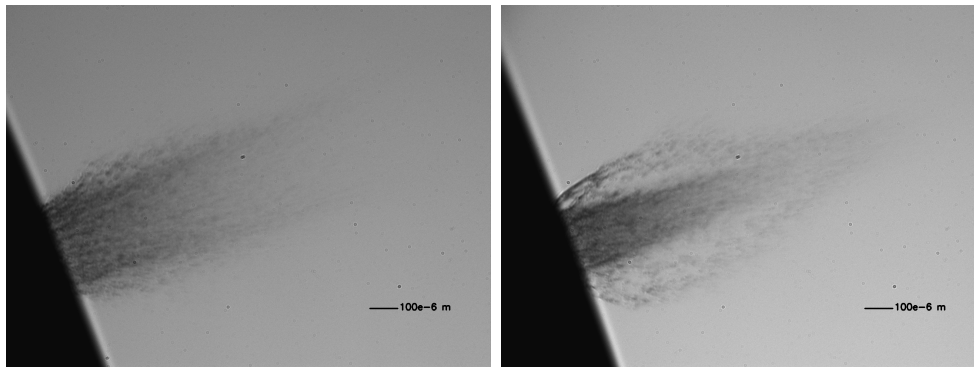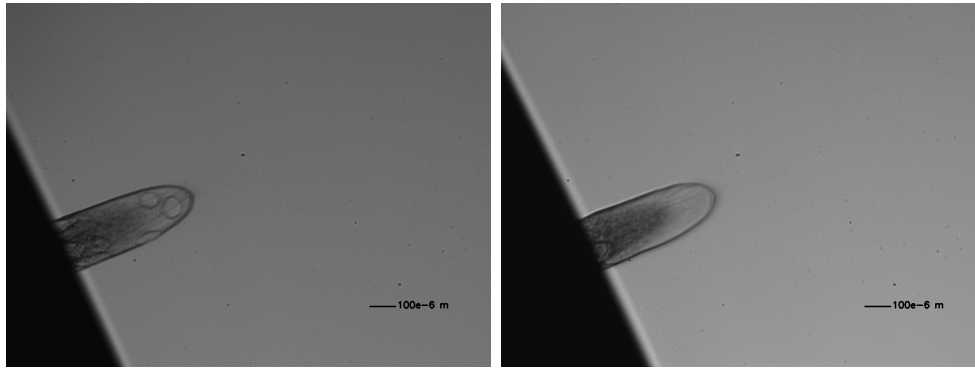

(a) Without any pre-pulse before the ablation pulse.

(b) With a pre-pulse before the ablation pulse.

Figure 2.10: Laser-driven glycerol plume with and without prior heating pulse, both images at a reference delay of 2 μs. The black scale bar corresponds to 100 μm.

---

[9]Depending on the structure of the solid, for example, crystalline glycerol has a melting point of 291.75 K [70].

[10]Heterogeneity here refers to the pockets of solid-like and liquid-like regions created in glycerol below the melting point by phase separation. A detailed understanding of this process is lacking.

(a) Without any pre-pulse before the abla- (b) With a pre-pulse 1 ms before the abla-
tion pulse.   tion pulse.

Figure 2.11: Laser-driven glycerol bubble with and without prior heating pulse, both images at a reference delay of 2 μs. The black scale bar corresponds to 100 μm.

Bubble formation

The most interesting observation during glycerol ablation occurs when we reach an intermediate ablation fluence regime approximately between $170 - 240$ mJ/cm^2. A notable process becomes visible as we move from ambient to vacuum, as shown in Figure 2.12. At these intermediate fluences, the plume transforms into a bubble hundreds of microns in size. For fluences below 170 mJ/cm^2 we find plumes with very defective shells, and at higher fluences (above 240 mJ/cm^2) we see a fractured shell remnant as shown in Figure 2.10b according to Leisner et al. [19]. Figure 2.13 shows a selected set of photographs taken at different time delays, representing the temporal evolution of the laser-driven glycerol bubble.
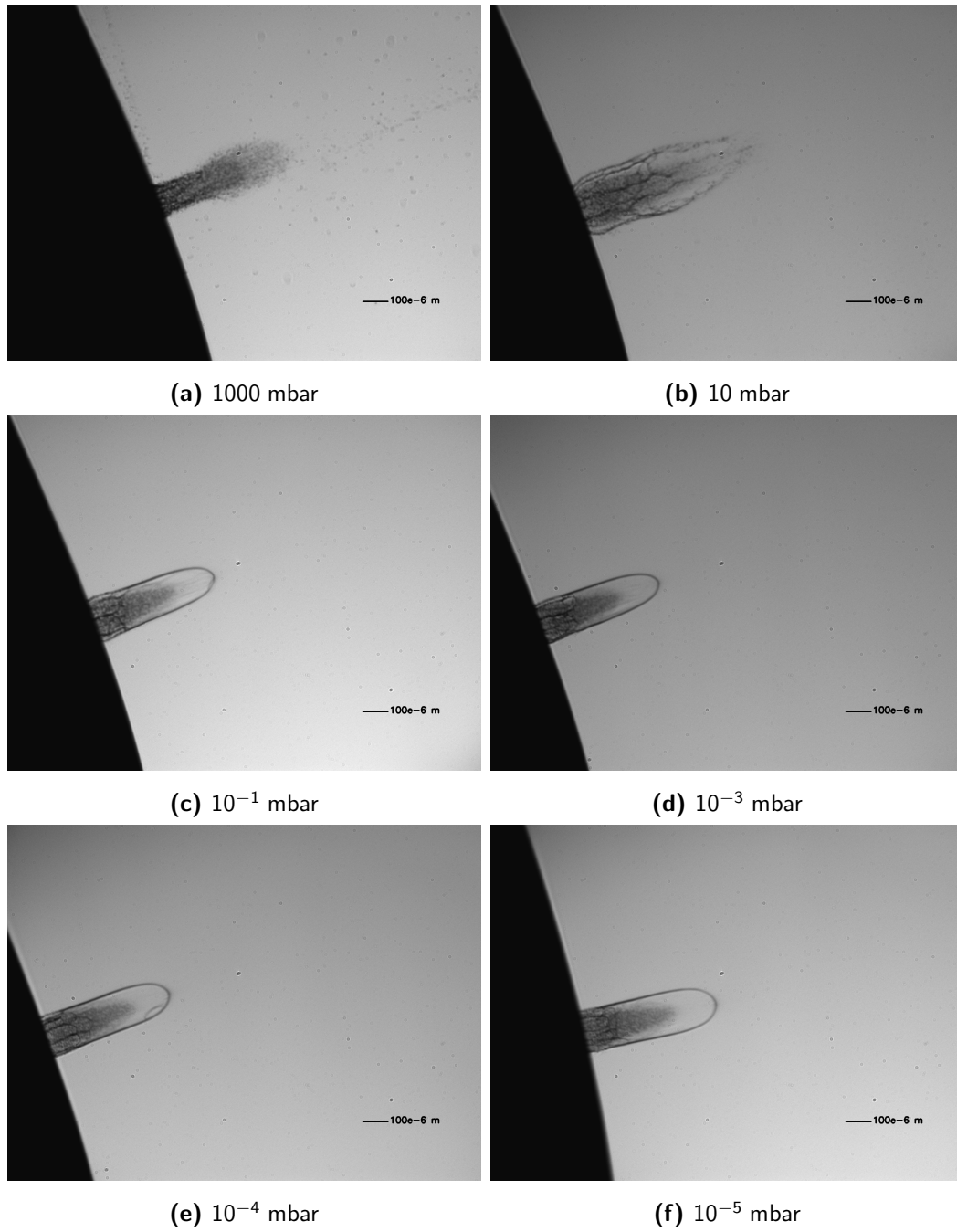
(a) 1000 mbar

(b) 10 mbar

(c) 10^{-1} mbar

(d) 10^{-3} mbar

(e) 10^{-4} mbar

(f) 10^{-5} mbar

Figure 2.12: Glycerol plumes and bubbles at 2 μs at various pressures at a fluence of 242 $\pm$ 11 mJ/cm^2. The black scale bar corresponds to 100 μm.

(a) 514 ns

(b) 1.1 μs

(c) 1.6 μs
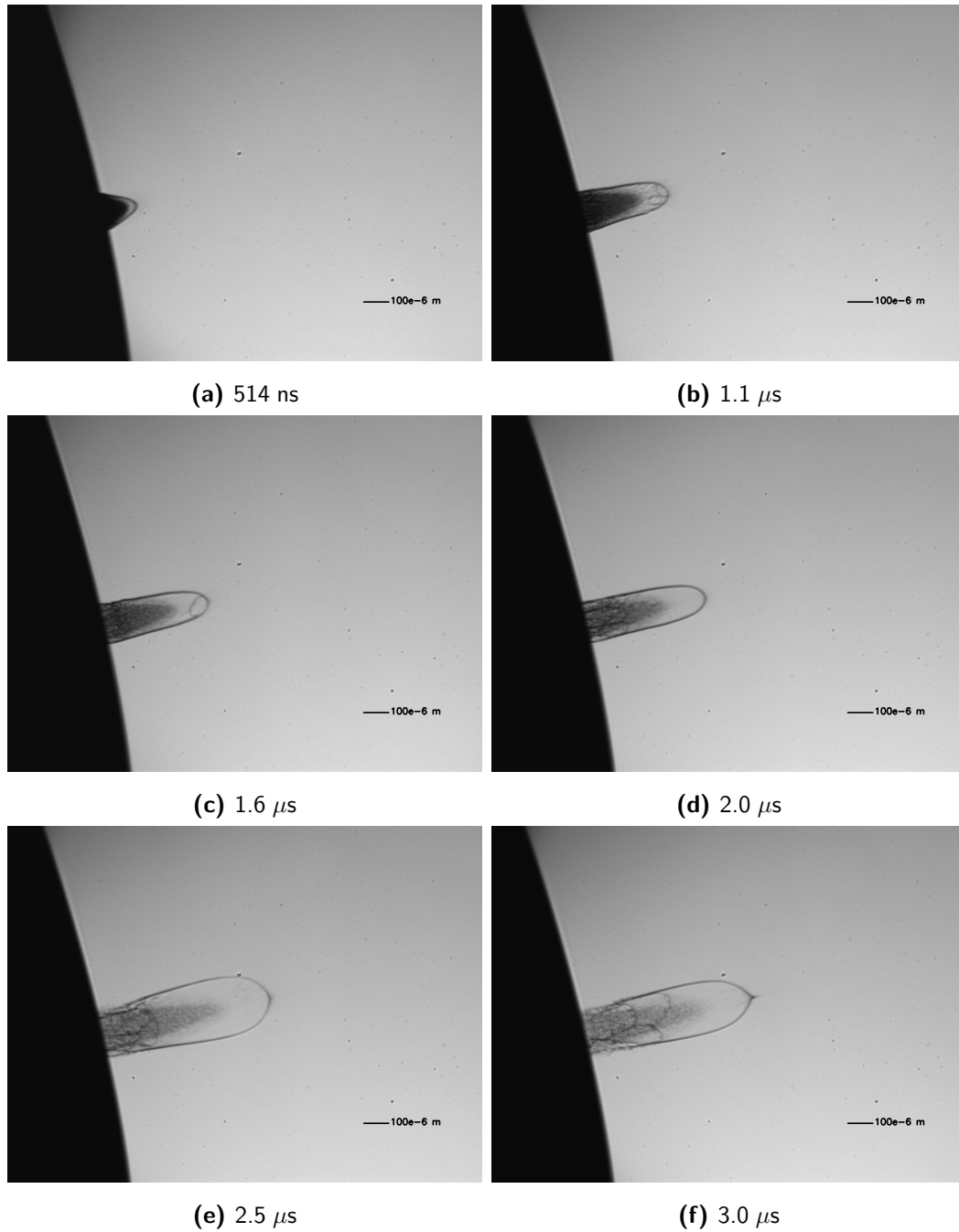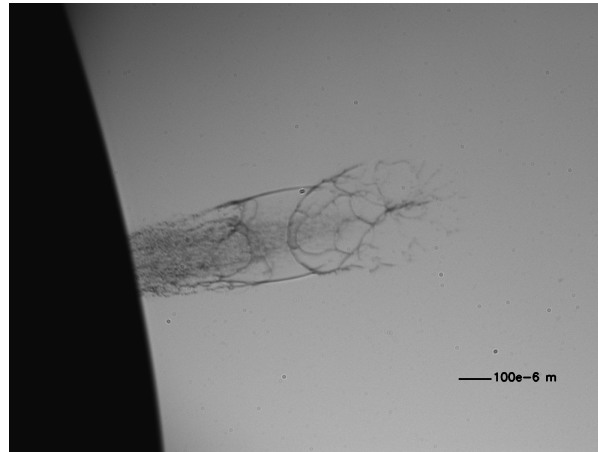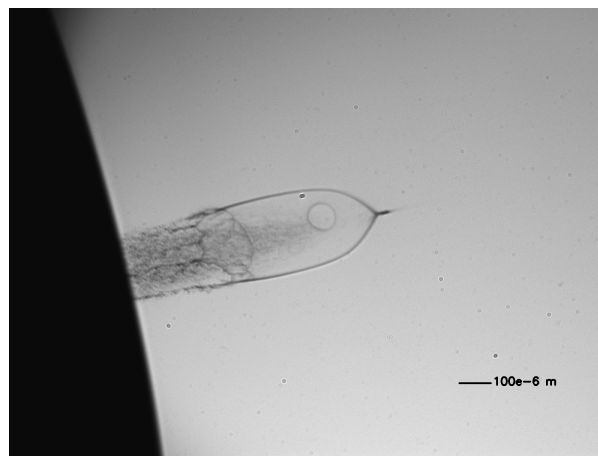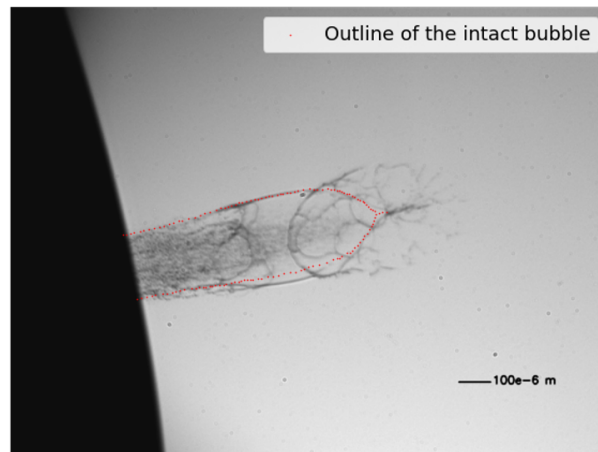
(d) 2.0 μs

(e) 2.5 μs

(f) 3.0 μs

Figure 2.13: Photographs of glycerol bubbles produced by laser ablation at a fluence of 242 ± 11 mJ/cm^2 under vacuum conditions (10^{-5} mbar). The black scale bar corresponds to 100 μm.

(a) Burst bubble at 3.6 μs

(b) Mostly intact bubble at 3.6 μs

(c) Intact bubble outline overlayed on the ruptured bubble

Figure 2.14: Bubbles at 2 μs at a fluence of 242 ± 11 mJ/cm^2, the larger size of the burst bubble shows that there is significant energy being stored in the bubble shell. The black scale bar corresponds to 100 μm.

2.2.3. Ionic Liquid

Ionic liquids are a type of liquid salts that have many applications in different industries and play an important role in the development of environmentally friendly and sustainable chemistry. A brief introduction to them and their applications can be found in the references [72–74].

Ionic liquids are known to have a very low vapor pressure [75]. Their low vapor pressure is one of the main benefits, as it allows us to study plume dynamics in a vacuum without changing the sample delivery mechanisms. Another virtue is the opportunity to test a different liquid (Tris-(2-hydroxyethyl)-methylammonium-methylsulfate) with very different molecular underpinnings than glycerol to study the behavior of laser-induced plumes in a vacuum.

For the current study, we know that the absorption coefficient of ionic liquid is lower than that of water and glycerol. The lower absorption coefficient increases the amount of energy required for ablation. Therefore, for ionic liquid ablations, we used a 100 mm lens to produce a tighter focal spot (see Figure 2.6c) compared to the 300 mm lens normally used (see Figure 2.6b).

Figure 2.15 shows images for ionic liquid ablation at ambient conditions for moderately high fluence. The deviation of the plume behavior from glycerol in Figure 2.9 is clear. A mixture of photomechanical effects and phase explosion may be responsible for the streams of liquid droplets and a broken but clearly defined boundary that we see in Figure 2.15.

Surface bubble formation is also evident in the case of the ionic liquid, but the bubble is less stable and prone to early rupture leading to multiple droplet streams at later time points, as shown in Fig. 2.16. This resembles the spallation shell dynamics of low fluence ablation of glycerol.

(a) 504 ns

(b) 1 μs

(c) 1.5 μs
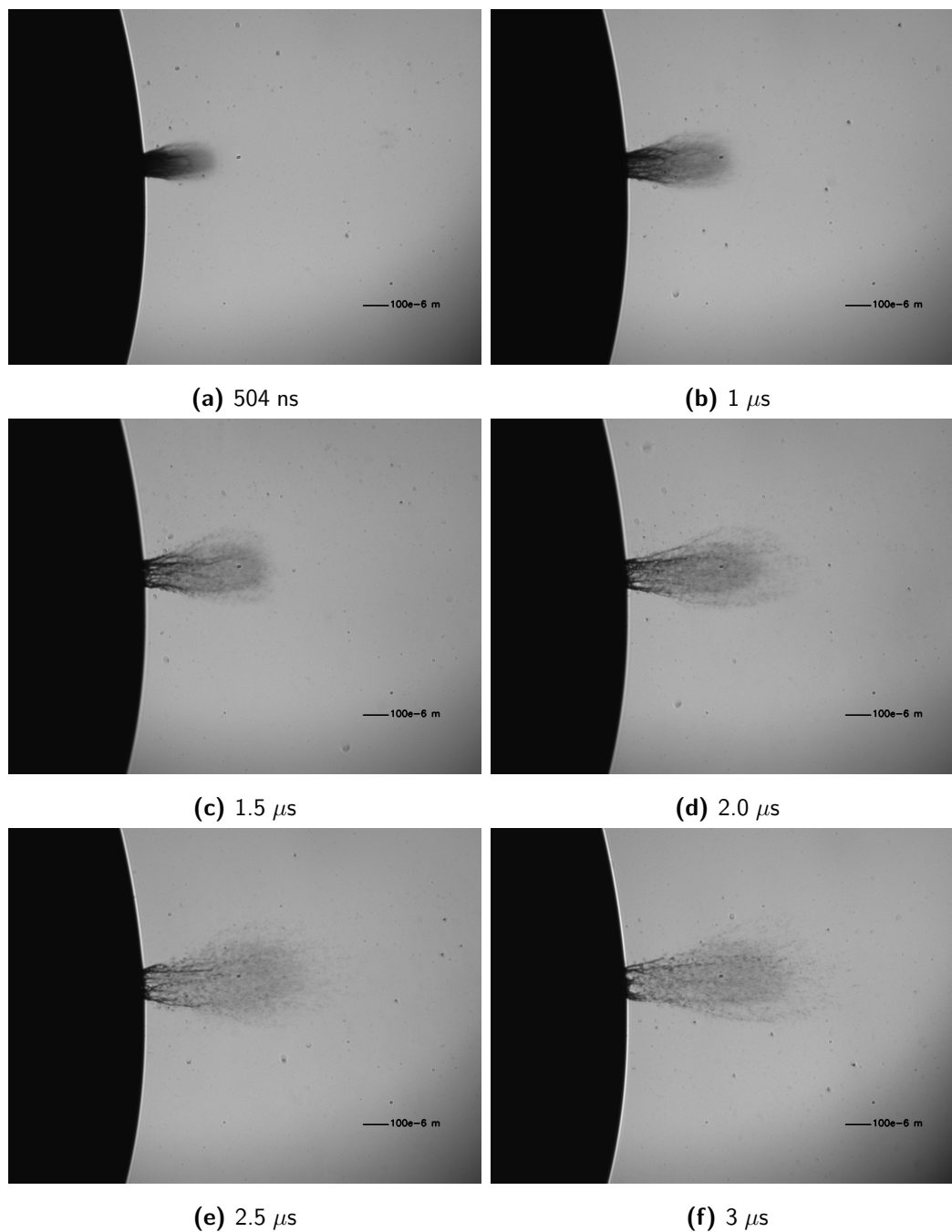
(d) 2.0 μs

(e) 2.5 μs

(f) 3 μs

Figure 2.15: Photographs of ionic liquid plumes created by a laser fluence of 752 ± 34 mJ/cm^2 ablation in ambient conditions (air and at room temperature). The black scale bar corresponds to 100 μm.

(a) 504 ns

(b) 1 μs

(c) 1.53 μs
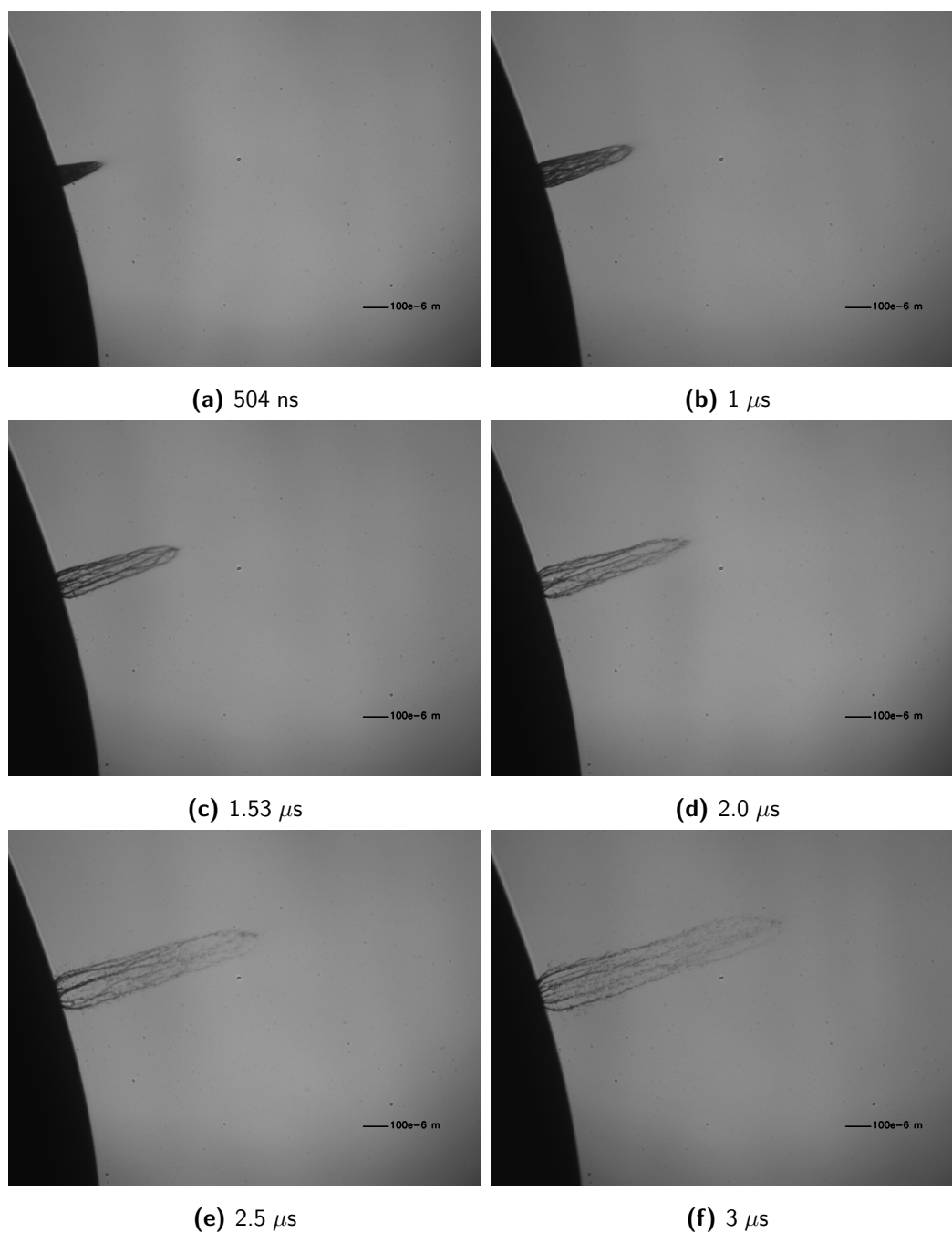
(d) 2.0 μs

(e) 2.5 μs

(f) 3 μs

Figure 2.16: Temporal progression of ionic liquid plumes created by a laser fluence of 241 ± 11 mJ/cm^2 ablation in vacuum (10^{-5} mbar). The black scale bar corresponds to 100 μm.

2.3. Remarks

Laser ablation of liquids in a vacuum is an under-explored area. Studying the behavior of these light-matter interactions and the ensuing dynamics could potentially provide answers to fundamental questions about the liquid state and tools to study a variety of systems at high strain rates. By carefully designing an experimental setup and selecting appropriate samples, we thoroughly studied the plume behavior of two vacuum-stable liquids at various fluences and pressures. The resulting plumes were primarily the result of two effects, photomechanical spallation, and phase explosion. The surprising observation of bubble formation in liquid glycerol at a particular fluence regime and below a specific pressure needs to be further investigated. In addition, the behavior of the ionic liquid during the ablation process is suggestive of a general feature of bubble formation. To better understand these findings, further research and analysis of the properties of the liquids and the ablation process are needed. In the next chapter, the bubble formation phenomenon observed in liquid glycerol will be explored in more detail.

2.3.1. Limitations

One of the limitations we have in the experiment is the shot-to-shot power variation we have with the ablation laser. To quantify the shot-to-shot variations, we monitored the ablation laser power with a photodiode for more than 12 hours. As for the shot-to-shot noise, the standard deviation is about 0.1197 V with a mean of 1.1301 V (recorded photodiode voltage amplitudes), which means that the ablation laser fluctuation is about 11%. This is a significant problem that unfortunately could not be solved.

Slight variation in the diameter of the focus beam at the ablation site is also a problem we have encountered. Droplet flow and variations in beam diameter due to the use of different neutral density filters can slightly change the focal spot diameter, which can

lead to an error between the reported fluence and the actual fluence. But for a beam of M^2 value 10-15[11], the Rayleigh length for a beam waist of 236 μm is greater than 1 mm. One millimeter is well within the range of droplet surface potential variations we observe, and in the case of significant droplet surface variations, the data are discarded.

The timing of the ablation event is determined by measuring the delay between two photodiodes. One triggered by the ablation laser and one triggered by the flash lamp[12]. The photodiodes have rise times of 2 ns and 14 ns, respectively, which introduce a systematic error into the delay measurement. The delay measurements can be overestimated by a maximum of about 20 ns when taking into account the other errors that can creep into delay estimation on oscilloscopes [76]. An inaccuracy of 20 nanoseconds is acceptable given that our interest in plume dynamics is mainly between $0 - 5$ μs with time steps an order of magnitude larger than the error.
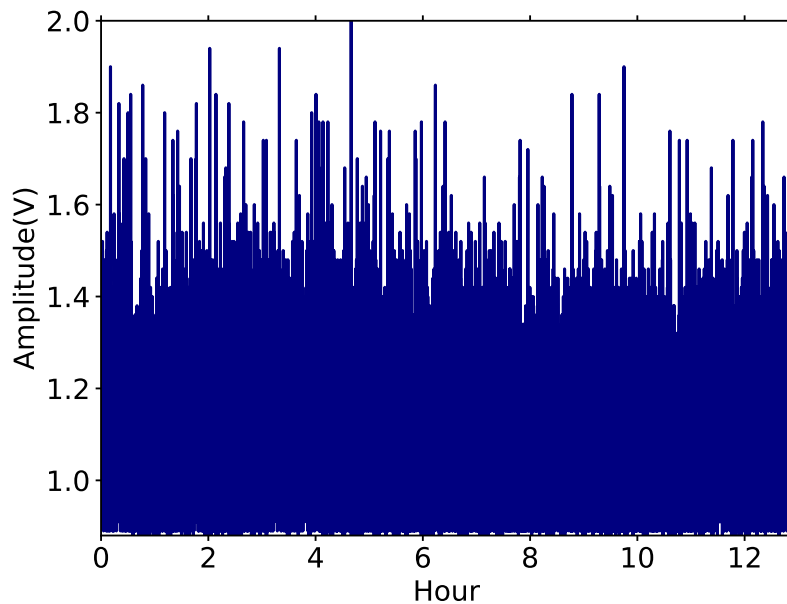

Figure 2.17: Ablation laser energy per shots measured using a photodiode vs time. The measurement was carried out for more than a whole workday to quantify the stability of the laser.

---

[11]The spatial profile of our ablation laser is quite different from a perfect Gaussian.

[12]The delay generator, Quantum composer, 9520 series, has a resolution of 250 ps and less than 50 ps jitter.

Chapter 3

Formation, growth, and rupture of laser-induced surface bubbles in liquid glycerol

In this chapter, I will discuss how to understand the dynamics of laser-driven glycerol bubbles by approaching the phenomenon from the angles of several disciplines. Some figures and parts of this chapter are adapted from the reference [21].

3.1. Bubble formation

Laser-induced bubbles similar to our observations, but with different origins and dynamics, have been widely observed [33, 77–79]. These bubbles are mainly formed during laser-induced cavitation[1] near a free surface and during laser-induced forward

---

[1]Homogeneous nucleation, which occurs due to local thermodynamic fluctuations in the absence of impurities, can be initiated by a short-pulsed ablation laser, and when such nucleation occurs near the free surface, material ejection is observed following the expansion of the vapor bubble.

transfer experiments[2] (LIFT) [78]. However, the mechanism of material ejection due to photomechanical stress waves differs from the phase explosion-induced material ejection in LIFT. In the latter case, the material is driven by an expanding vapor volume, whereas photomechanical spallation is the result of thermoelastic stress waves. Ideally, in photomechanical spallation, due to the absence of phase explosion, only a minimal amount of energy contributes to the phase change, apart from some vaporization within voids and cracks [23].

In the case of metal ablations, we can also find bubbles resulting from spallation [33], that have a similar origin compared to the bubbles described in this thesis. However, observations of metastable spall layer ejections in small molecule liquids, as we have observed, are rare [36].

3.1.1. Laser-induced stress waves and confinement conditions

For photomechanical spallation to occur, laser-induced transient stress waves above a certain threshold magnitude are required. To achieve this, the laser ablation process must satisfy two constraining criteria - thermal and stress confinement. Thermal and stress confinement are critical to maximize the stress generated [22, 23].

Stress-confined ablation typically occurs when the ablation laser has very short pulse lengths, allowing these lasers to deposit energy at a much higher rate than the system can dissipate it. Stresses induced in the system can be relaxed by molecular diffusion, and for glycerol the time it takes to release the stress is approximately a nanosecond [59]. Stress relaxation time[3] can also be determined by the absorption coefficient (μ_a) together with the velocity of sound in the material (c_s) [18]. For glycerol at room temperature with the ablation laser wavelength of 2.94 μm we find:

$$\tau_s < \frac{1}{\mu_a \times c_s} = \frac{1}{6.5 \times 10^5 \text{ m}^{-1} \times 1890 \text{ m/s}} \approx 814 \text{ ps} \tag{3.1}$$

---

[2]Laser Induced Forward Transfer is a digital printing technique that uses a pulsed laser beam as the driving force to project material from a donor thin film onto the receiving substrate.[80]

[3]Also known as acoustic energy dissipation time.

The criteria for thermal confinement are met for energy deposition below roughly a microsecond. In glycerol, thermal redistribution occurs on the order of 6×10^{-6} s [81]. Thus, in our ablation experiments ($\lambda_l \approx 2.94 \ \mu m$, $\tau_l = 400 \pm 50$ ps) we satisfy both thermal and stress confinement requirements.

3.1.2. Localized temperature increase after ablation

With respect to liquid ablation, there is a lack of studies on local temperature distributions, probably due to the challenges associated with the dynamic nature of the process [82], adding uncertainty to the modeling of such systems. In addition, there is a lack of access to certain parameter values, such as the Grüneisen parameter[4] and dynamic tensile strength, under extreme conditions.

However, with knowledge of the isochoric heat capacity (C_v), we can derive a qualitative understanding of the increase in temperature during ablation. For the pressure evolution that we may have in the system (> 100 MPa), the isochoric heat capacity of glycerol is not available from the literature. However, a very recent study by Ahmadi et al. [83] that suggests a value at a pressure of 55 MPa. At this pressure, we have a C_v of about 2142 J/Kg K for a 298 K isotherm.

The temperature increase can then be calculated if the volume of material interacting with the laser pulse is known. It is assumed that the area of laser-matter interaction is equal to the area covered by the average base radius of the bubble and that only the energy deposited in this area is responsible for the temperature increase.

With these assumptions, an upper estimate of the temperature increase can be made based on the different thicknesses at which the interaction can occur. For an absorption coefficient of $\mu_a = 6500 \ cm^{-1}$, 90% of the incident laser energy can be absorbed within 3.5 μm (assuming exponential attenuation). Thus, for a cylindrical volume with a height of 3.5 μm and a radius of 80 μm, about 39 μJ of the total laser pulse

---

[4]The Grüneisen parameter (Γ) is a dimensionless thermodynamic parameter named after the German physicist Eduard Grüneisen. It can be used to describe the pressure-temperature relationships during laser ablation events.

energy of 53 μJ can be absorbed[5].

Assuming that all 39 μJ is converted to heat, we get a local temperature increase of about 200 K (resulting in a shell temperature of about 493 K), well below the boiling point of glycerol (about 560 K at atmospheric pressure 1.013 bar [84]). However, in this limiting scenario, layers to a depth of less than 1.5 μm could be heated above the boiling point due to the exponential absorption of laser energy.

3.1.3. Photo mechanical spallation

In order to understand the formation of bubbles after laser ablation in our case, we need to examine the mechanical effects associated with laser ablation of materials. The mechanism of particular interest is known as photomechanical spallation. In the illuminating review article on the mechanical effects associated with laser ablation [23], Platauf and Dyer explain this topic well.

Thermoelastic compressive stress waves are generated following the incidence of the laser ablation pulse. These include the stress waves propagating into the medium as shown in Figure 3.1 and towards the free surface. Because of the acoustic impedance mismatch of the medium (in our case, glycerol) and the vacuum at the free surface, the wave propagating towards the free surface is reflected at the boundary. As a result, a component of the tensile stress wave is generated, which propagates into the medium with increasing amplitude as it propagates. At some depth, if the magnitude of the tensile component equals or exceeds the tensile strength[6], the material may fracture. This fracture can be followed by the ejection of a spall layer or fragments. Since the spallation occurs on the same side of the target with respect to the laser pulse incidence, the term "front surface spallation" has been used to describe this process. Refer to the article by Dingus et al. [35] for a more detailed look at front surface spallation with a focus on tissue ablation.

---

[5]The incident energy is calculated by integrating the fluence distribution over the top surface of the cylinder and taking 90% of that value. See Section 2.1.5.

[6]Temperature changes and strain rates in the system can affect the spall or tensile strength [85], but for simplicity we use the dynamic tensile strength measured for liquid glycerol at room temperature for all our calculations [86].
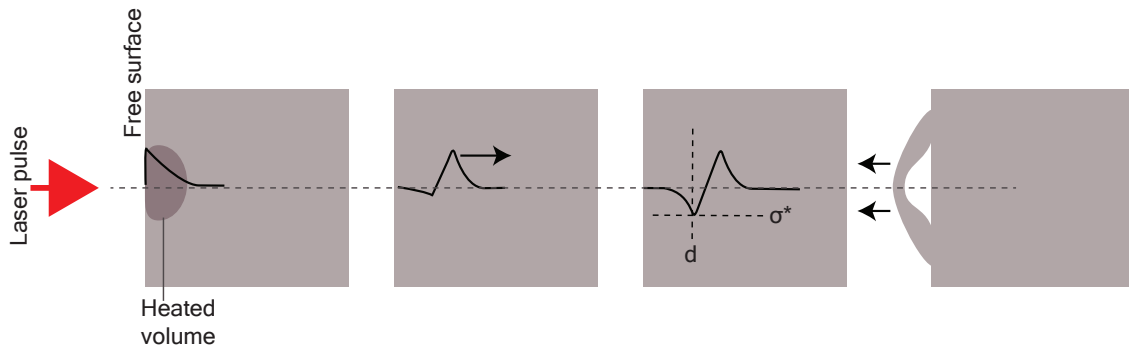
Figure 3.1: Laser ablation induces compressive stresses that propagate in all possible directions. At the free surface, a tensile component with an increasing amplitude is generated, which propagates into the sample due to the reflection of the compressive stress wave. At depth d, the tensile strength (σ^*) is exceeded and the formation of voids occurs, which later results in the surface bubble. Figure reproduced from [23].

There are computational fluid dynamics as well as molecular dynamics studies conducted prior to this work for liquid water for 2.94 μm ablation [26, 28, 29] that explore phase explosion in detail for early stages of the dynamics using much higher fluences than the studies of focus here. However, no such studies have been found for glycerol or other liquids under vacuum on time scales of a few microseconds where two- or three-dimensional modeling of the problem is desired. Also, unlike water, there are no reliable equations of state[7] for glycerol under these extreme conditions to study these phenomena. Several studies have attempted to explain the mechanism of spall fracture [85, 87], but due to modeling constraints, no complete model is available that visualizes the formation of the spall shell and the associated extended dynamics. Quantitative modeling of spall formation will require a model that incorporates the laser-matter interaction [88] and later fluid dynamics, which is beyond the scope of this thesis. Nevertheless, a qualitative description of such a process can be provided with the current understanding of photomechanical spallation problems, which will be discussed in detail later in the Section 3.1.4.

The formation of the spall layer, which occurs in the early stages of ablation as a result of photomechanical stress waves, can be viewed as the result of an amalgamation

---

[7]An equation of state is a thermodynamic equation that relates state variables such as pressure, volume, temperature, internal energy, etc., to describe the state of matter under a given set of physical conditions.

of several nucleation processes [85], as shown in Figure 3.2. As we discussed earlier, in the case of ablation of pure liquids, assuming the absence of other impurities, we have a homogeneous nucleation. Homogeneous nucleation refers to the creation of voids in liquids as a result of local thermodynamic changes. To elaborate, if we could focus down to the molecular level, we would be able to see that the liquid under observation is in a highly dynamic state, with minute local fluctuations in density. Sudden fluctuations in local pressure and temperature due to photomechanical stresses induced by the incidence of an ablation laser could result in the formation of voids larger than the critical radius[8]. The voids can grow and coalesce into a macroscopic scale separating a thin layer of liquid from the bulk due to the unstable mechanical equilibrium. The limiting pressure and temperature required to form such a void determine the tensile strength of the liquid.
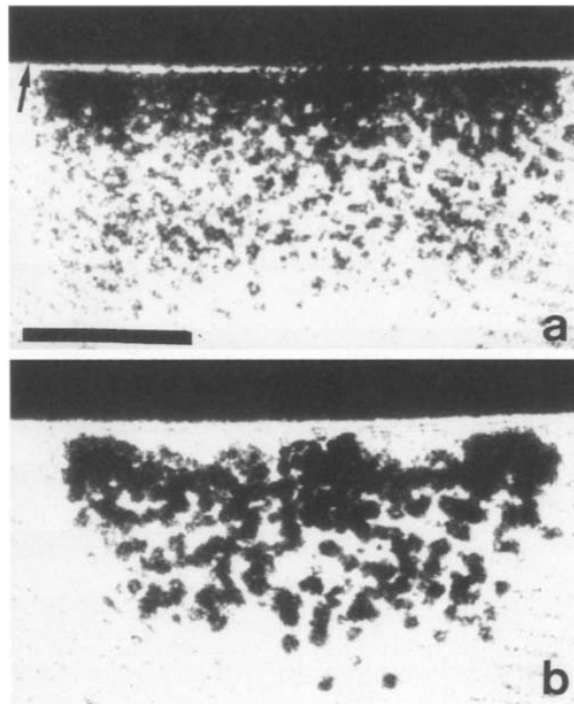

Figure 3.2: Images of cavitation in water taken with the gated video camera at delay times of 1.1 μs (**a**) and 5.1 μs (**b**) after the laser pulse has hit the surface (arrow in image **a**). The growth of these cavitation bubble clusters causes the spall fracture and ejection of material or shell. Taken from the article by Paltauf et al. [37] with permission. Copyright Springer 1996.

In 1972, Carlson and Henry developed an experimental technique to study dynamic

---

[8]The critical radius is the smallest radius formed by the clustering of particles before a nucleation bubble can grow due to internal pressure.

tensile fracture in fluids [89]. A later study [86] by Carlson and Levine determined the tensile strength of glycerol for a temperature range of $218 - 350$ K, where the tensile strength varied between $246 - 32$ MPa, giving a value of 85 MPa for glycerol at room temperature (293 K). Thus, a tensile stress with an amplitude greater than 85 MPa can induce spallation in liquid glycerol at 293 K.

3.1.4. One-dimensional thermoelastic wave equation in glycerol

A simple model describing the photomechanical responses in liquids after the absorption of laser pulses has been proposed by Carome et al. [90]. This model provides a qualitative understanding of the transient stresses induced during our ablations. We follow the slightly modified equations described by Paltauf et al. [23], which is for top-hat laser beams as opposed to the Gaussian beams we have in our case. Nevertheless, we can use Paltauf's model to get an estimate of the depth at which spallation can occur.

As introduced in Section 3.1.3, the initial shock wave propagating towards the free surface can be reflected at the surface. The magnitude of the reflected component is given by the reflection coefficient,

$$R_{ac} = \frac{Z_2 - Z_1}{Z_2 + Z_1} \tag{3.2}$$

where Z_1 and Z_2 are the acoustic impedances[9] of the liquid glycerol and the surrounding medium, giving us a value of -1 for R_{ac} in our case, since the surrounding medium is vacuum with an acoustic impedance of 0.

After reflection, the amplitude of the tensile wave traveling into the liquid may exceed the tensile strength of the liquid glycerol at some depth, causing a tensile fracture. We call the depth at which the tensile amplitude equals 85 MPa [86] the hypothetical

---

[9]The specific acoustic impedance (Z) is the ratio of acoustic pressure to particle velocity and is an inherent property of the medium and the nature of the wave. For the simplest case of a plane wave, the specific acoustic impedance is the product of the equilibrium density (ρ) of the medium and the speed of sound (c_s).

spallation depth (HSD).

To find the HSD, we need to know the stresses at $d > 0$, which is the sum of the three components p_1, p_2 and p_3 [23]:

$$p_\delta(d, t) = p_1 + p_2 + p_3 \qquad (3.3)$$

$$p_1 = \begin{cases} 0.5 \times p_{0,max} \times \exp(-\mu_a(d - c_s t)), & \text{if } d > c_s t \\ 0, & \text{Otherwise} \end{cases}$$

$$p_2 = \begin{cases} 0.5 \times p_{0,max} \times \exp(-\mu_a(d + c_s t)), & \text{if } d > 0 \\ 0, & \text{Otherwise} \end{cases}$$

$$p_3 = \begin{cases} 0.5 \times p_{0,max} \times R_{ac} \times \exp(-\mu_a(c_s t - d)), & \text{if } c_s t > d > 0 \\ 0, & \text{Otherwise} \end{cases}$$

with,

$$p_{0,max} = \mu_a \Gamma F_{peak} \qquad (3.4)$$

where Γ is the Grüneisen parameter, μ_a is the absorption coefficient of the ablation laser wavelength used, and F_{peak} is the peak fluence of the ablation laser.

To model our system as realistic as possible, it is necessary to account for the finite duration of our ablation pulse, which can be done by convolving the temporal nature of the pulse with the stress distribution.

$$p(d, t) = g(t) \otimes p_\delta(d, t) \qquad (3.5)$$

The influence of a finite laser pulse duration can also be included in the calculation by using a time-dependent pressure pulse derived from the temporal profile of the ablation pulse instead of $p_{0,max}$. In our modeling, we use $g(t)$ with a Gaussian time distribution with a sigma of about 170 picoseconds (corresponding to an FWHM of 400 ps) centered at about 600 picoseconds. Since the exact timing of spallation is unknown and is also determined by factors outside the description of our equations, we model the induced stresses over an arbitrary time period of 8 ns.

Based on the above procedure, using an input pressure distribution shown in Figure 3.3, the thermoelastic stress distribution $p(d, t)$ shown in Figure 3.5 is obtained.

A clear trend can be seen in Figure 3.6, where the depths at which the tensile stress
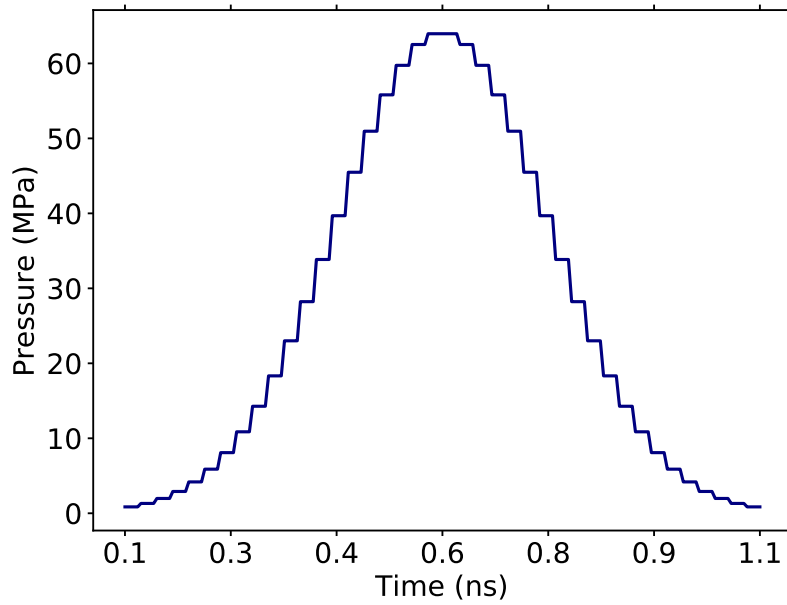
Figure 3.3: Induced pressure plotted against time that used as input to the one-dimensional thermoelastic wave equation solver.
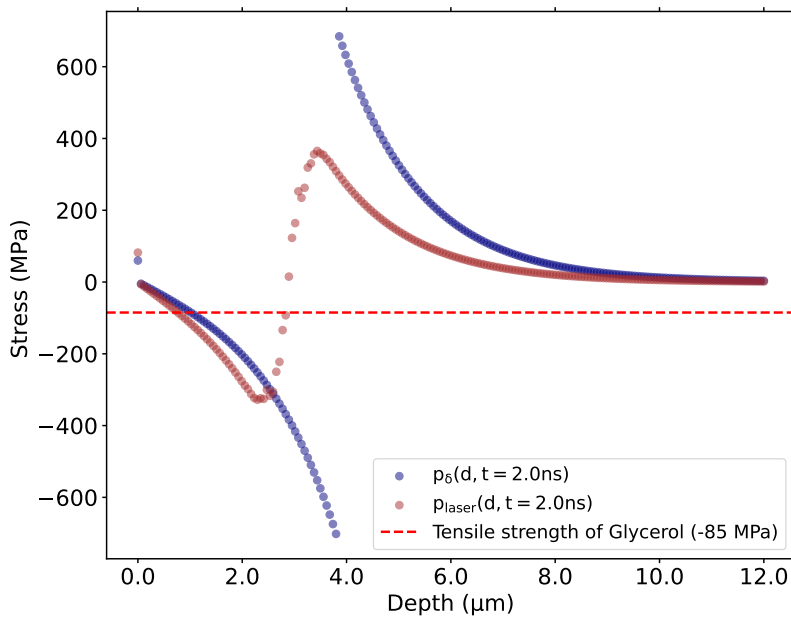

Figure 3.4: Pressure vs. depth derived using the one-dimensional thermoelastic wave equations. The instantaneous heating $\left(p_\delta(d, t)\right)$ is shown in blue and the finite laser pulse influence $\left(p_{laser}(d, t)\right)$ is shown in brown. plotted for a given time $t = 2$ ns.
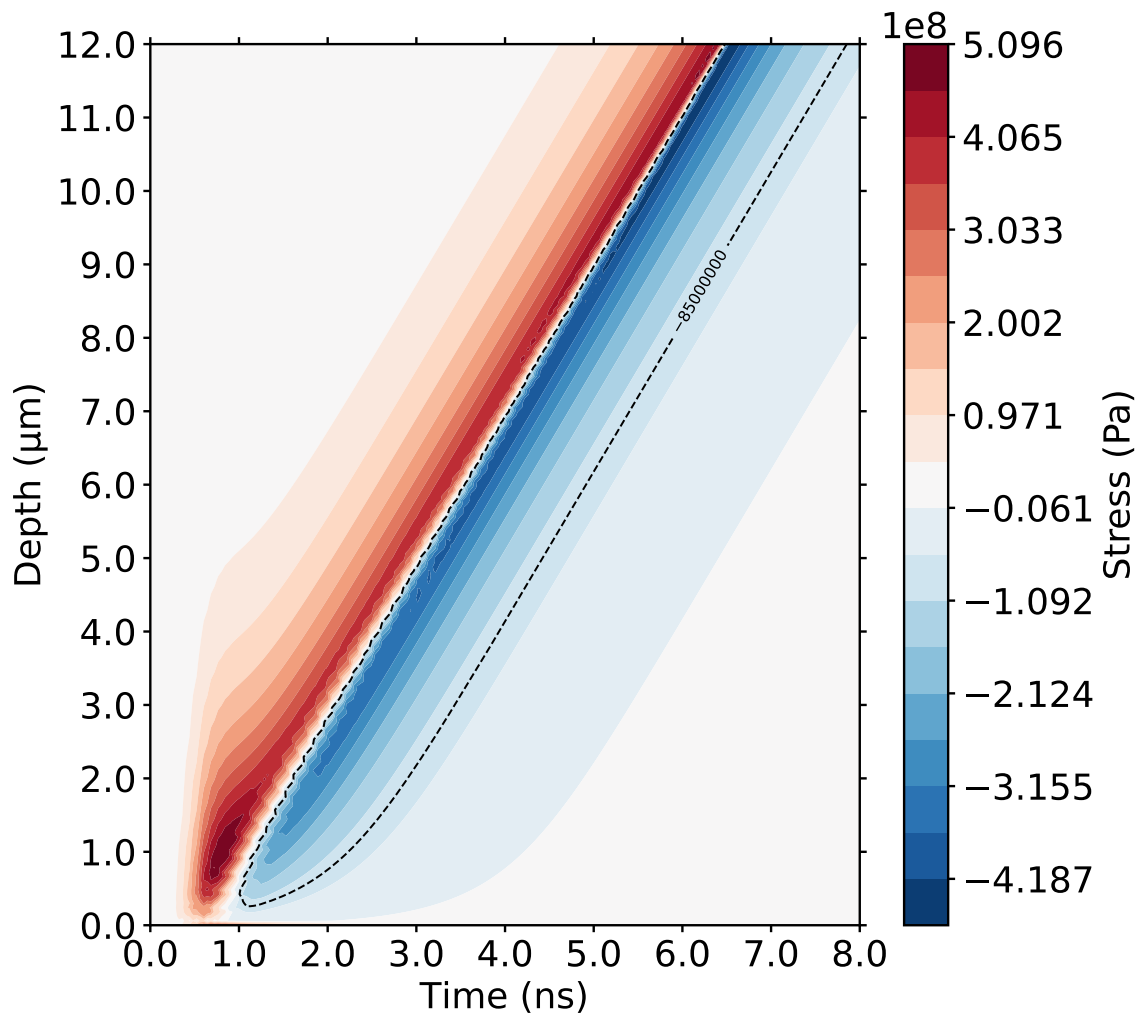
65

Figure 3.5: One-dimensional solution of the thermoelastic wave equation with compressive (red colors) and tensile (blue colors) stresses in liquid glycerol. Plotted as a function of depth from the bulk surface versus time for a pulse energy of 43 μJ. The dashed black line indicates the reported dynamic tensile strength of glycerol at 293 K. Figure adapted from [21].
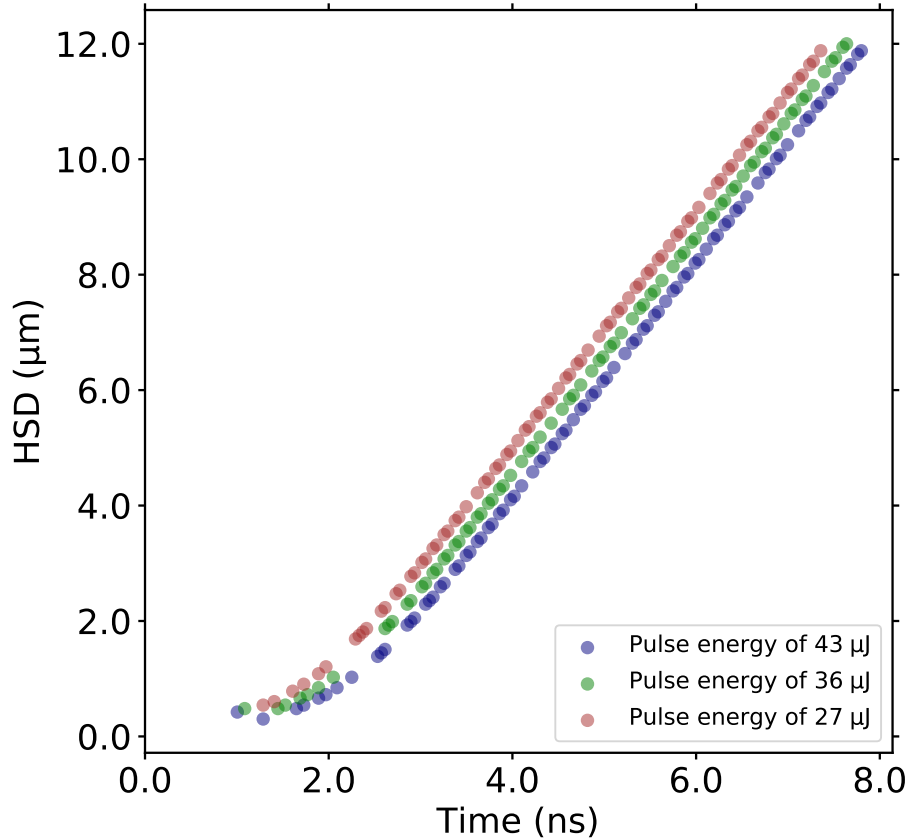
Figure 3.6: Hypothetical spallation depth vs. time assuming the spall fracture occurs at 85 MPa for glycerol for different ablation energies. Figure adapted from [21].

amplitude of 85 MPa is reached are plotted against time. Figure 3.6 shows an inverse proportionality for the depths reached at a given time to the pulse energy.

It can be concluded that the spatial intensity profile of the Gaussian laser beam can lead to a significant variation of the spallation depths at different parts of the bubble in the case of a single ablation. Assuming that the shell thickness has a direct correlation with the spallation depth, we expect to see an increase in thickness towards the region closer to the bulk.

The main limitations of this model are the temperature-dependent variations of the Grüneisen parameter and the fluence-dependent variations of the absorption coefficient. We do not have an estimate for these quantities for glycerol. Since the other inputs are direct observables, they will introduce a minimal error. However, the inadequacy of the model to provide information about the time of the spallation event is by far the biggest hurdle in determining an accurate spallation depth.

The fluence dependence of the absorption coefficient of glycerol at 2.94 μm has not

been investigated, in contrast to the case of water [91]. However, we do not expect significant deviations from the established value of 6500 cm^{-1} for the moderate fluences in our system. The same cannot be said for the Grüneisen parameter Γ. There are scenarios in which a significant reduction in Γ is observed with respect to temperature changes [92]. Thus, the estimation of fracture depth must be understood in conjunction with other observations. However, considering the comments on spallation fracture depth by Dingus and Scammon [35] along with our spallation depth estimates, the qualitative estimate for the actual spallation depth could be one to several times the penetration depth of the laser, in our case the penetration depth for 2.94 μm ablation laser wavelength is about 1.5 μm in glycerol.

3.2. Bubble growth

To understand the bubble growth process, we first looked at existing studies of laser-induced cavitation and LIFT, which we discussed in Section 3.1. In such cases, researchers use the Rayleigh-Plesset (RP) equation [36, 93], which is commonly used to describe the expansion of cavitation bubbles under the assumption that the bubble evolves in an infinite medium. Any flow other than the purely radial flow induced by the growth of the bubble is ignored, and then all information about the original flow is assumed to be contained in the form of the pressure inside the bubble P_b. This leads to the following second-order differential equation,

$$-\frac{(P_{ext} - P_b)}{\rho} = R\frac{d^2R}{dt^2} + \frac{3}{2}(\frac{dR}{dt})^2 + \frac{4\eta}{\rho R}\frac{dR}{dt} + \frac{2\sigma}{\rho R} \tag{3.6}$$

where R is the radius of the bubble, P_{ext} is the pressure in the liquid, P_b is the pressure inside the bubble and can have a time-dependent form $P_b(t)$, and ρ, η, and σ are the density, viscosity, and surface tension of the liquid, respectively. Additional terms can be added to the RHS of Equation 3.6 to account for the viscoelasticity of the medium, but this can quickly become extremely complex as there are different approaches to incorporate these contributions [94].

Our attempts to describe the motion of the bubble tip using the Rayleigh-Plesset equation have been unsuccessful for two possible reasons. First, laser-driven shell formation is the result of multiple cavitation events triggered by the photomechanical effects and not a vapor pressure-driven bubble expansion, whereas the Rayleigh-Plesset equation is primarily used to describe the growth of a single cavitation bubble. Second, it is possible that we have not been able to accurately incorporate the unexpected viscoelastic behavior into the equation, leading to discrepancies in our predictions.

However, the vertical motion of the tip of the bubble, marked in red in Figure 3.7, can be fitted to two simple functions of time, from which we can derive different insights into the dynamics of the shell. First, we have Newton's equation of motion, describing the motion of the bubble's tip ($h(t)$) as follows,

$$h(t) = ut + \frac{1}{2}at^2 \tag{3.7}$$

where u is the initial velocity and a is the acceleration. The least-squares fitting of Equation 3.7 with the measured tip position provides estimates of the initial velocity and deceleration of the bubble tip, which are documented in Table 3.1. The velocity and acceleration of the bubble tip are directly and inversely related to the ablation fluence, respectively.
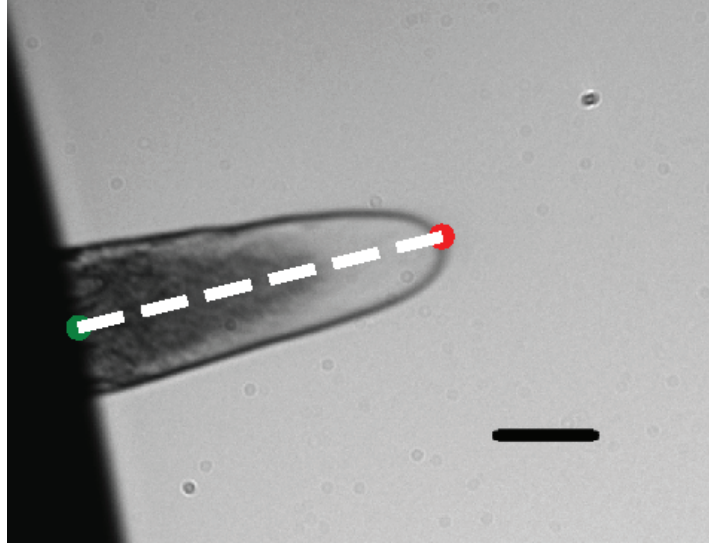

Figure 3.7: Illustration showing the bubble vertical distance measurement scheme.

Fluence $(\frac{mJ}{cm^2})$	u (m/s)	a (m/s^2)
242 ± 11	327 ± 7	$-62 \pm 4 \times 10^6$
206 ± 9	287 ± 7	$-38 \pm 4 \times 10^6$
174 ± 8	213 ± 7	$-29 \pm 5 \times 10^6$

Table 3.1: Parameters for Equation 3.7 derived from the fit for the bubble tip motion described in Figure 3.8.

The transverse vibration of a thin film in the z-direction can be effectively described by a two-dimensional wave equation [95] as follows,

$$\frac{\partial^2 z}{\partial x^2} + \frac{\partial^2 z}{\partial y^2} = \frac{1}{c^2} \times \frac{\partial^2 z}{\partial t^2} \tag{3.8}$$

where c is a constant. However, when the motion of the point is considered in only one dimension, such as the elongation of the bubble tip, the transverse motion is
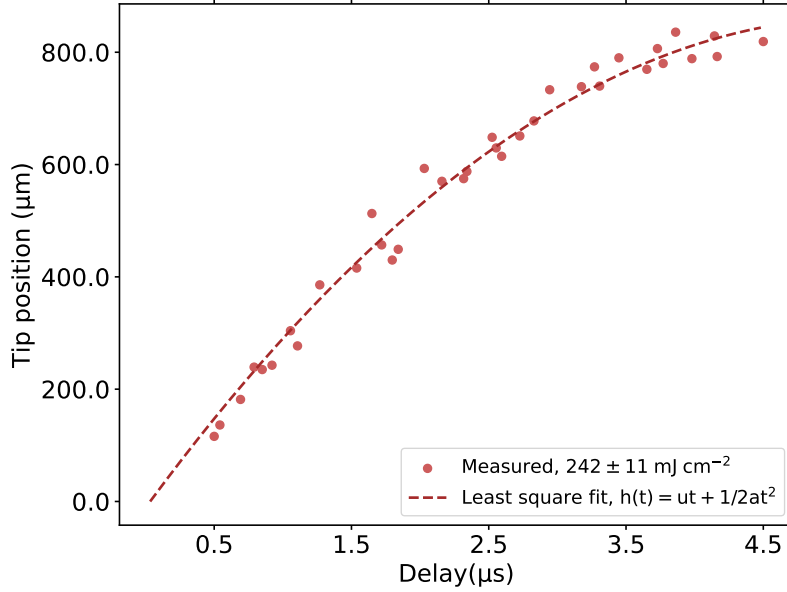
Figure 3.8: Bubble tip vs. delay, fitted with Equation 3.7, shown for an ablation fluence of 242 ± 11 mJ/cm^2.

characterized by a sinusoidal solution of the one-dimensional wave equation [95]. Interestingly, we have found that this sinusoidal description agrees remarkably well with the experimental data. From this sinusoidal motion we can derive an elastic modulus, in this case Young's modulus, which gives us an idea of the elastic properties of the shell. The following section outlines the evaluation of these elastic contributions.

In the 1660s, Robert Hooke came up with the idea that for relatively small deformations of an object, the deformation is directly proportional to the deforming force or load. This is known as Hooke's Law and it follows,

$$m\frac{d^2x}{dt^2} = -kx(t) \tag{3.9}$$

where k is a constant that describes the elastic properties of the material [10]. Solving Equation 3.9 yields,

$$x(t) = c_1 \times sin(\sqrt{\frac{k}{m}} \times t) + c_2 \times cos(\sqrt{\frac{k}{m}} \times t) \tag{3.10}$$

where k can be expressed in terms of the angular frequency ω given by $\omega = \frac{2\pi}{T}$ as $k = m\omega^2$. This angular frequency describes the simple harmonic motion of the elastic

---

[10]Since Equation 3.9 is widely used to describe the behavior of spring systems, we generally associate k with the spring constant.

material. Equation, 3.10, can be simplified and written as follows,

$$x(t) = A \ sin(\frac{2\pi}{T} \times t + \psi) \tag{3.11}$$

where A is the amplitude of the oscillation, i.e. the maximum displacement of the object from equilibrium. If $x = 0$ at $t = 0$, then $\psi = 0$ which simplifies Equation 3.11 as follows,

$$x(t) = A \ sin(\frac{2\pi}{T} \times t) \tag{3.12}$$

By characterizing the functional behavior of the bubble tip ($h(t)$) as the first quarter period of a sinusoidal motion, as defined in Equation 3.12, we get,

$$h(t) = h_{max} \times sin(\frac{2\pi}{T} \times t) \tag{3.13}$$

Where h_{max} is the amplitude. As shown in Figures 3.9 and 3.10, Equation 3.13 can accurately fit our tip motion and the fit parameters are documented in Table 3.2.
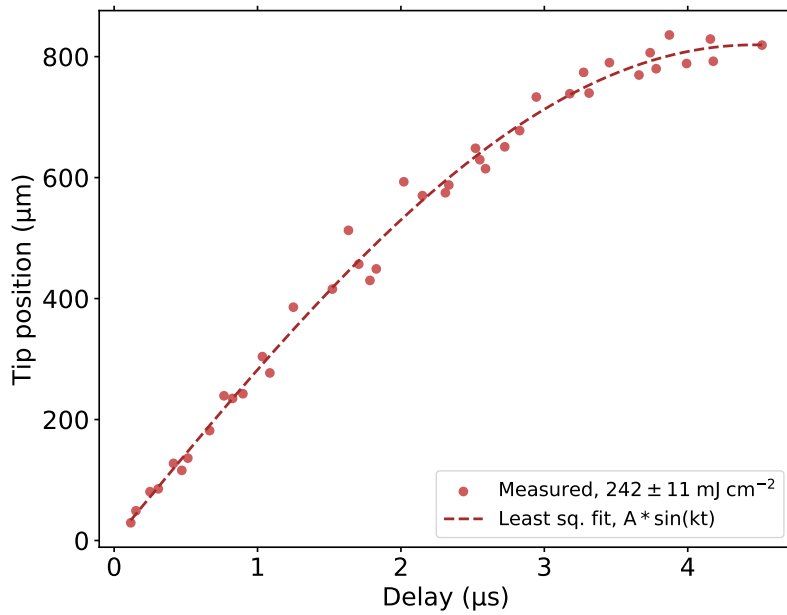

Figure 3.9: Bubble tip position plotted against delay for an ablation fluence of 242$\pm$11 mJ/cm^2 along with the least square fit for Equation 3.13.

To determine the elastic properties of the shell, we modeled the expansion of the bubble using a finite element solver[11], as described in the Appendix C. Using this
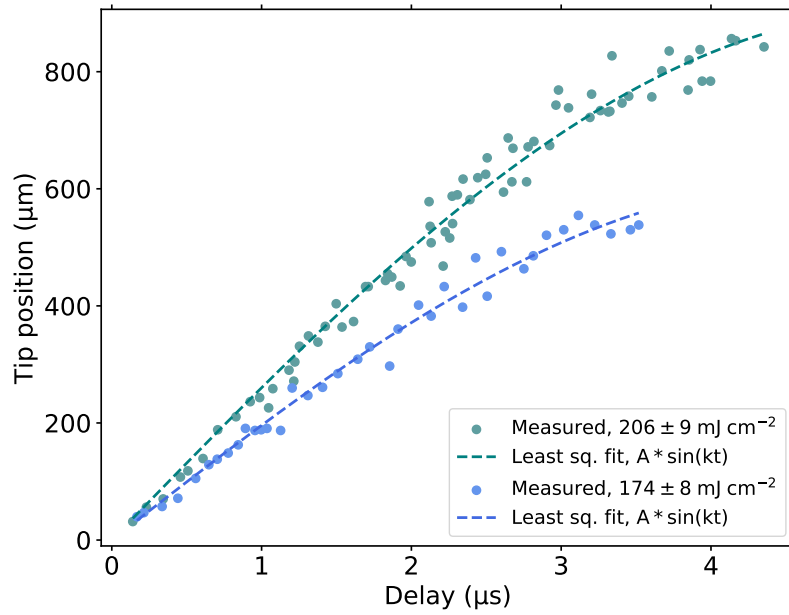
---

[11]COMSOL Multiphysics™

Figure 3.10: Bubble tip position plotted against delay for ablation fluences of 206 ± 9 mJ/cm^2 and 174 ± 8 mJ/cm^2 along with the least square fits for Equation 3.13.

procedure, we can determine the values of the dynamic Young's modulus (DYM) corresponding to the parameters h_{max} and $\frac{T}{2}$ that we derive for the least squares fits shown in Figures 3.9 and 3.10. The derived DYM values are given in Table 3.2 along with the fit parameters.

The magnitude of the DYM values is on the order of 0.2 MPa and is surprisingly high and of a rubber-like magnitude [38, 96]. It has been shown in shock loading experiments that the molecular diffusion relaxation time appears to increase with a direct dependence on strain rate [47, 58] for glycerol. Increased relaxation time can result in the manifestation of elasticity in Newtonian fluids. The trend of the DYM of the laser-driven liquid shell is consistent with a linear dependence on the laser fluence, as shown in Figure 3.11. The strain rate in the bubbles is also dependent on fluence, leading us to believe in the strain rate-driven source of elasticity.

Fluence ($\frac{mJ}{cm^2}$)	h_{max} (μm)	$\frac{T}{2}$ (μs)	Dynamic Young's modulus (E, MPa)
242 ± 11	819 ± 12	8.93 ± 0.03	0.21 ± 0.01
206 ± 9	906 ± 26	10.79 ± 0.04	0.19 ± 0.02
174 ± 8	614 ± 32	9.68 ± 0.07	0.15 ± 0.01

Table 3.2: Parameters for Equation 3.13 derived for the bubble tip motion described in Figures 3.9 and 3.10.
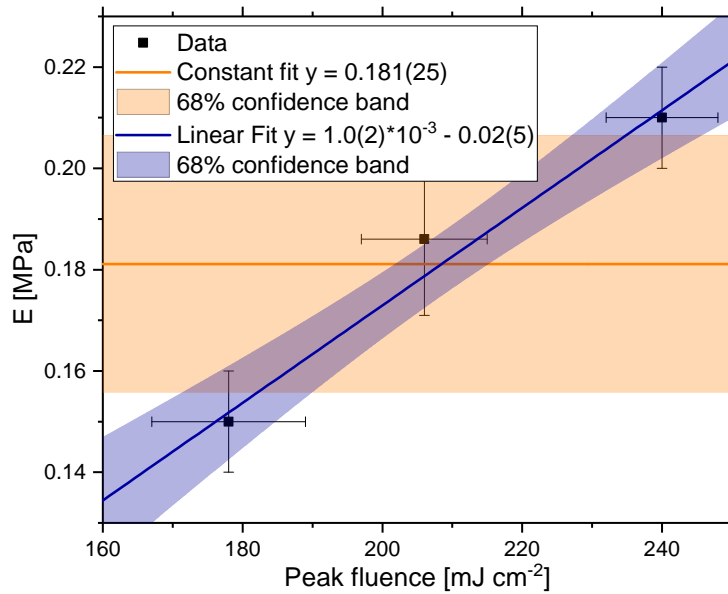

Figure 3.11: Dynamic Young's modulus calculated for the bubble vs. ablation fluence. The data are consistent with a linear increase in Young's modulus with increasing fluence. A constant fit is also applied to the data along with a linear fit. Figure adapted from [21].

3.3. Bubble rupture

We explore the bubble fracture mechanism as a complementary method to analyze the elastic contributions to bubble dynamics. This complementary approach becomes particularly relevant when the expansion of the shell has slowed considerably.
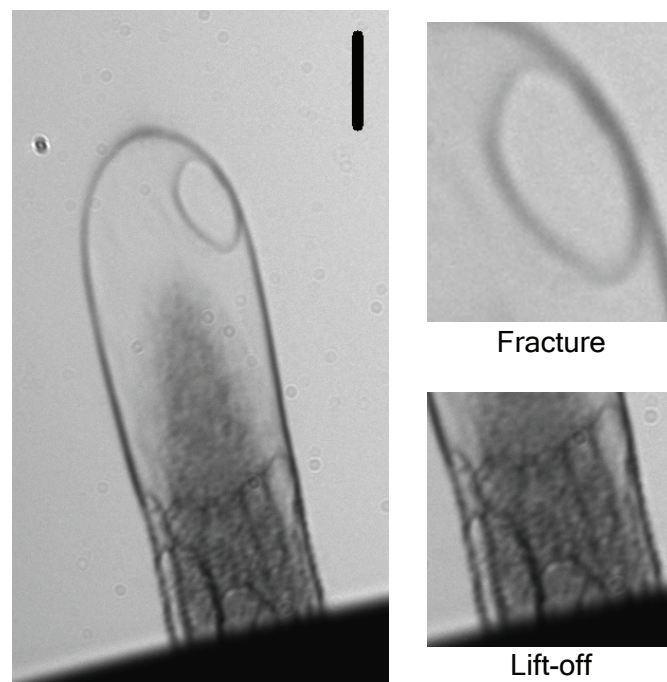

Figure 3.12: The figure illustrates the defects in the shell and the two terminologies used to describe them. The presence of multiple liquid droplets is thought to be responsible for the region of high contrast observed within the bubble.

We have divided the fractures that occur in the bubble into two categories, as shown in Figure 3.12. When the bubble begins to fracture at the base (where it touches the liquid surface), we call it lift-off[12], while a fracture that begins at the top of the bubble is simply called a fracture.

To analyze the growth of the hole and determine the elastic contributions, we study the fractures that develop near the top of the shell. This region is far away from

---

[12]As this fracture can give the impression that the shell will eventually detach from the bulk and take off like a rocket

the numerous droplets inside the bubble visible in Figure 3.12. We assume that the effect of the droplets on the fracture dynamics is insignificant. However, this cannot be assumed for lift-off, since there is a possibility that the droplets at the bottom of the shell could act as nucleation sites if they interact with the shell, reducing the stability of the shell where it is close to the bulk. In addition, it should be noted that the strain rates are lowest in the region closest to the bulk, which could also affect the lift-off dynamics.

Due to the stroboscopic nature of the measurements, we lack a complete understanding of the fracture evolution for a single bubble. Instead, we have data on the fracture radius for different bubbles at different delay points. In addition, we have calculated the probability of rupture for a given set of bubbles. This probability of rupture is plotted against the median delay of the representative group in Figure 3.13. As can
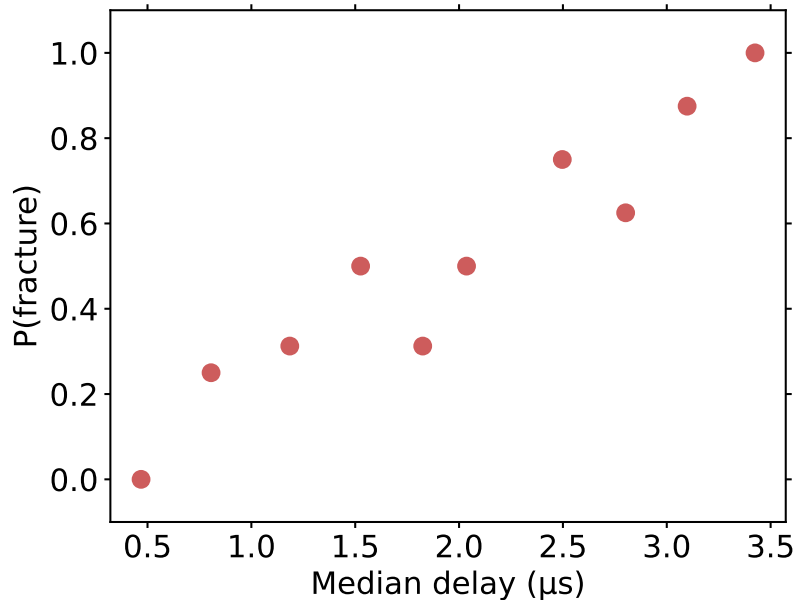

Figure 3.13: Probability of the fracture event vs. median delay time for an ablation fluence of 242 ± 11 mJ/cm^2.

be seen from Figure 3.13, the probability of fracture increases significantly from 0 for times less than 500 ns to 1 for times greater than 3.5 μs for an ablation fluence of 242 ± 11 mJ/cm^2. To analyze the rupture of the bubble, we must first determine the thickness of the bubble. The following subsection describes the method used to estimate the bubble thickness.

3.3.1. Estimating bubble shell thickness

Obtaining an accurate measurement of the bubble shell thickness is essential to understanding the unexpected deviation observed in the Taylor-Culick velocity (TCV), as the thickness is one of the parameters that determines the TCV. While we have some estimates of the possible bubble thickness from the spallation depth calculations described in the previous Section 3.1.4, a quantitative approach is required to determine the bubble thickness.

Conventional methods for determining bubble thickness, such as multi-color interferometry, require assumptions about bubble shell density [97, 98] similar to those used in the forthcoming segment, but offer no additional benefits. In addition, the integration of these methods into time-resolved measurements is very challenging. As an alternative to current approaches, we developed a purely computational and empirical approach to estimate bubble thickness.

The optical path length of a system in which pure absorption contributes to the intensity is described by the Beer-Lambert law,

$$A = \log(\frac{I}{I_0}) = \epsilon Z c \tag{3.14}$$

where A is the absorbance, I_0 and I are the intensity before and after absorption, ϵ is the absorptivity, Z is the optical path length and c is the concentration. This equation can also be rewritten as,

$$I = I_0 \times \exp(-a \times Z) \tag{3.15}$$

where a is a constant that includes contributions from the concentration (c) and the absorption properties of the material (ϵ).

In the present study, the mechanisms contributing to image formation are multifaceted, involving a combination of absorption, scattering, and diffraction, making explicit modeling challenging. It should be noted that a nonlinear dependence of the path length exponent can arise under such circumstances [99, 100]. Therefore, we cannot use Equation 3.15. However, we have been able to incorporate the nonlinear dependence of the effective path length Z_e by using the following equation which is

completely phenomenological,

$$I(Z_e) = I_1 + I_0 \times \exp(-a \times Z_e^b) \tag{3.16}$$

With Equation 3.16 describing the functional relationship between the geometric path length and the experimentally observed intensity profile, we can now proceed to estimate the shell thickness. To do this, we need to obtain values for the parameters I_1, I_0, a, and b for all possible thicknesses we encounter in the system. This is done by using very early spalls approximately at $\Delta t < 200$ ns. Two crucial assumptions must hold for these early spalls.

1. The structure of these early spalls has rotational symmetry about the z-axis.

2. The early spall and the later shell are liquid and have the same density (or close to it). And the early spall is completely filled with liquid glycerol.

Assumption 1 can be justified by the nearly Gaussian nature of our ablation pulse, which results in symmetric spallations. Assumption 2 can be justified on the fact that the bulk modulus for liquid glycerol is of the order of a few GPa [101]. In our cases, the initial shock pressures are well below 1 GPa. A significant change in density is therefore impossible. If the early spall is not completely filled, as shown in Figure 3.15, the final shell thickness estimate will be affected accordingly. A 50% filled early spall will result in a 50% thinner shell.

The shell thickness estimation procedure is carried out as described in the following steps. We identify a position on the z-axis (the red line in Figure 3.14) by examining the transmission intensities along the line where the pixel value reaches zero or 100% absorption only along the axis. The absorbing object is then assumed to be a filled disk with a uniform distribution of liquid. The effective path length for this material can be determined by simple geometric calculations and is shown in Figure 3.15.

Using an iterative procedure, we adjust the diameter of the disk according to the wings of the intensity profile shown in Figure 3.17 and fit the transfer function in Equation 3.16 with the corresponding Z_e to determine the parameters (I_1, I_0, a and b). This gives a very good fit to the intensity distribution, as shown in Figure 3.19. To accommodate the resolution limitation we have, the final fit is convolved with a Gaussian point spread function of FWHM 4.7 μm determined by a USAF[13] resolution

---

[13]The USAF Resolution Test Chart is a microscopic optical resolution test device originally defined by the U.S. Air Force.
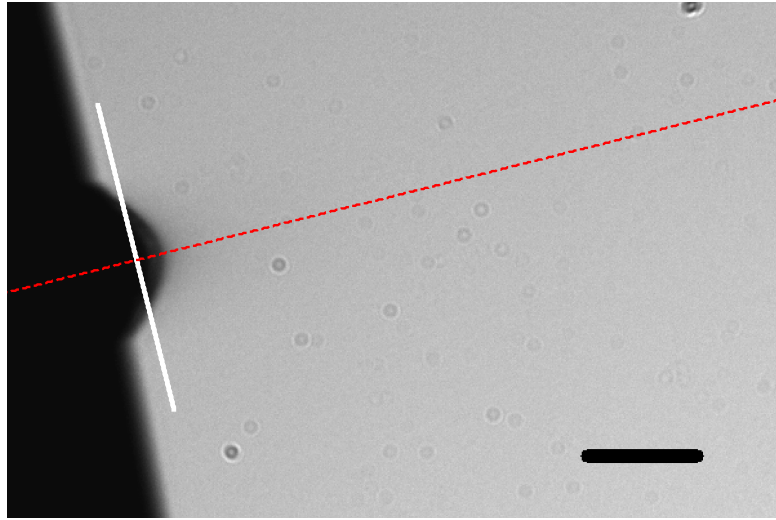
Figure 3.14: An early spall for a delay of $\Delta t = 190$ ns with the red dashed line indicating the z-axis along which the location of the intensity profile is determined. The white line indicates the location of the intensity profile shown in Figure 3.16. The black scale bar corresponds to 100 μm.
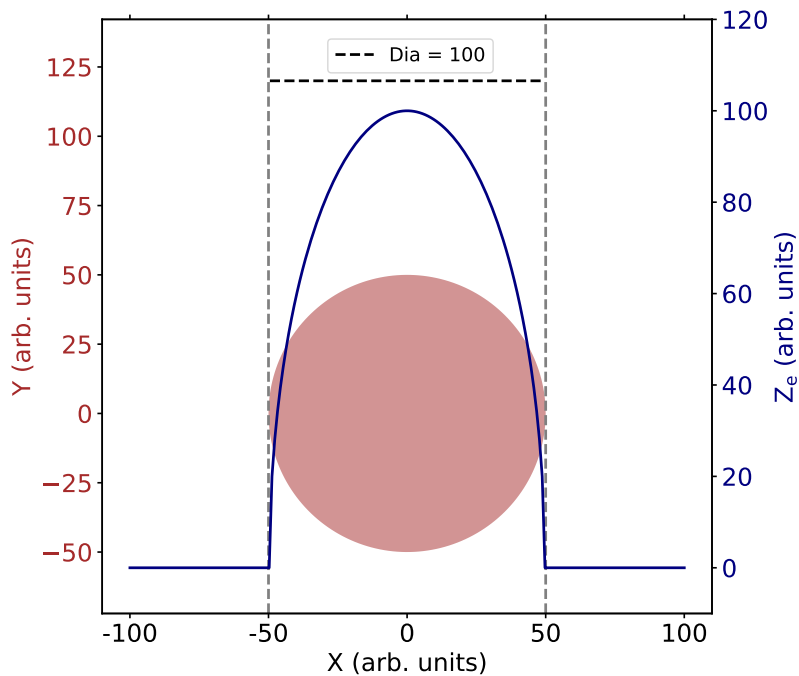

Figure 3.15: The effective path length (blue) and the corresponding filled disk (light brown)
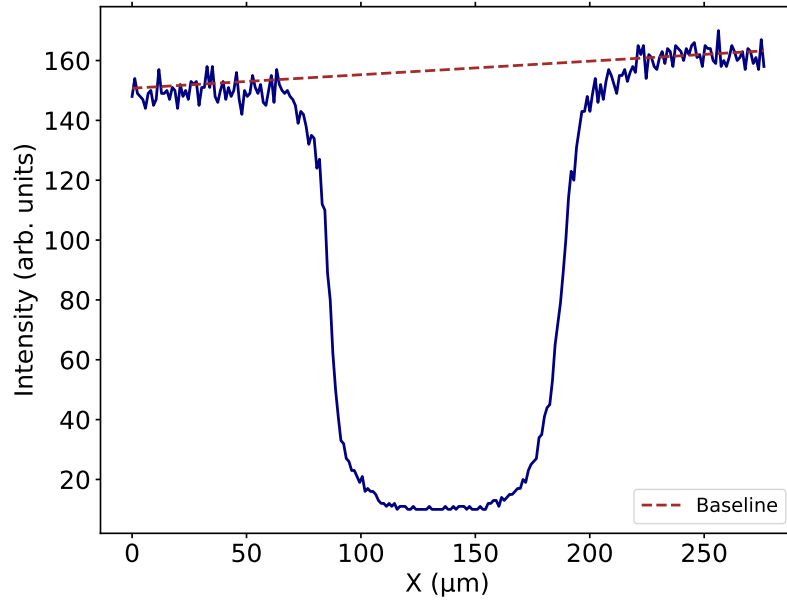
calibration target.

Figure 3.16: The intensity profile of the nascent spall at the location marked in Figure 3.14 in blue and the baseline (brown, dashed line).

Δt	a	b
152 ns	6.3×10^{-7}	3.4
202 ns	2.2×10^{-8}	4.1
172 ns	2.4×10^{-8}	4.1
190 ns	5.6×10^{-9}	4.5

Table 3.3: Parameters for Equation 3.16 used in thickness estimation.

With the parameters determined for a few different nascent bubbles, we can apply a similar procedure to bubbles at a later delay Δt and deduce the intensity profile from the fully determined transfer function. To do this, we create an effective path length determination function analytically using simple geometric calculations. An illustrative example is shown in Figure 3.20.
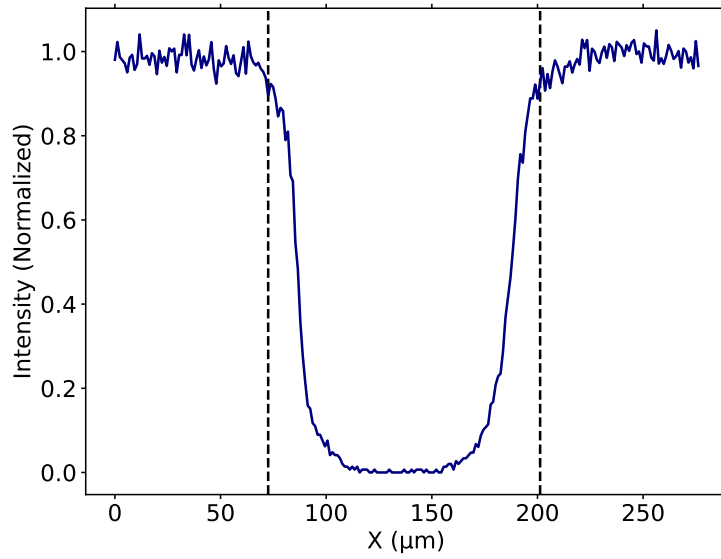
Figure 3.17: The baseline corrected normalized intensity profile (blue)

Figure 3.18: The baseline corrected normalized intensity profile (blue) and an appropriate effective path length (Z_e) derived from the wings marked by the black dashed lines.

Figure 3.19: The normalized intensity profile (blue) and the fit of $I(Z_e)$ with the Gaussian convolution (brown dashed line).
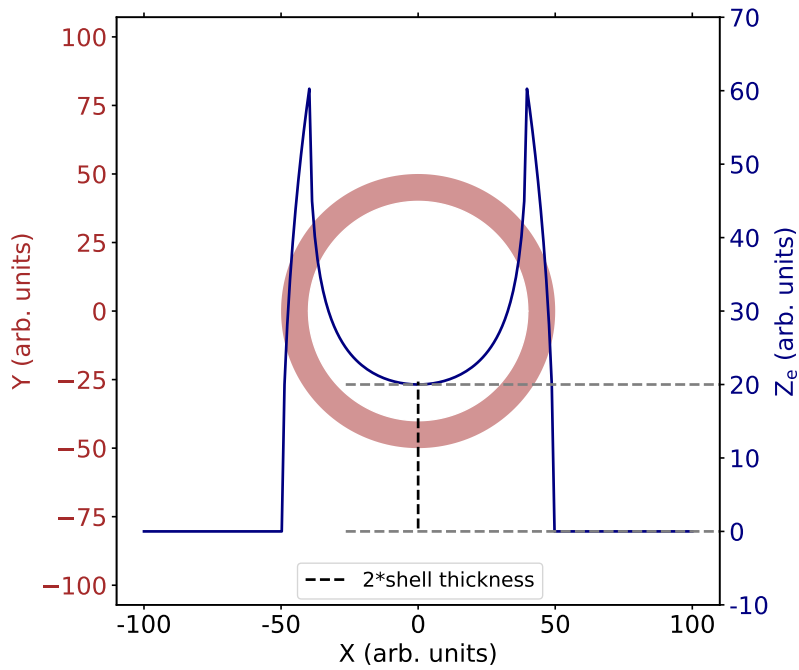
Figure 3.20: The effective path length (blue) and the corresponding shell of arbitrary thickness 10 (light brown).

Figure 3.21: A bubble for a delay of $\Delta t = 1.7\ \mu s$ with the red dashed line indicating the z-axis along which the location of the intensity profile is determined. The white line indicates the location of the intensity profile shown in Figure 3.22. The black scale bar corresponds to 100 μm.
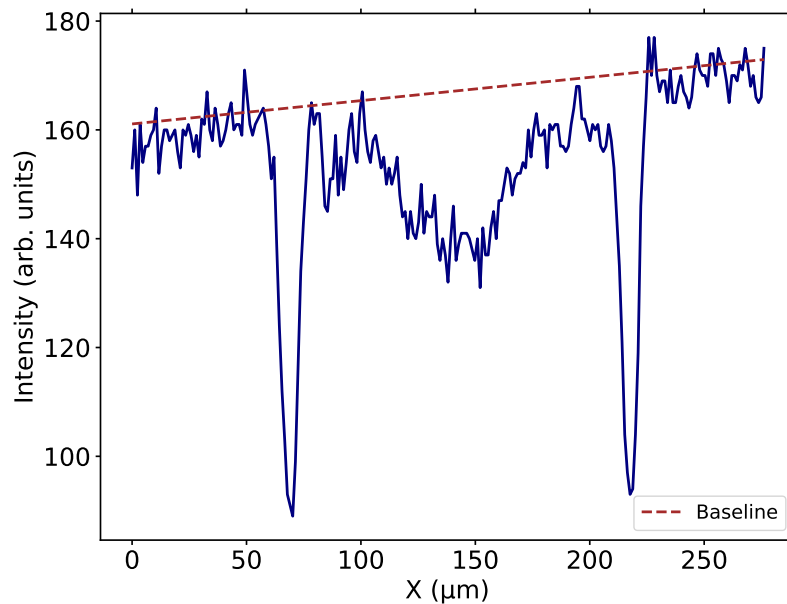
Figure 3.22: The intensity profile of the bubble at the location marked in blue in Figure 3.21 and the baseline (brown dashed line).
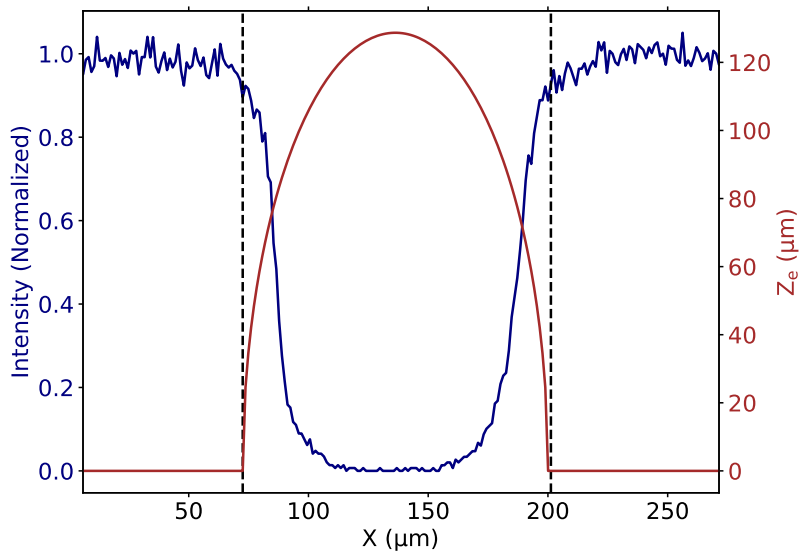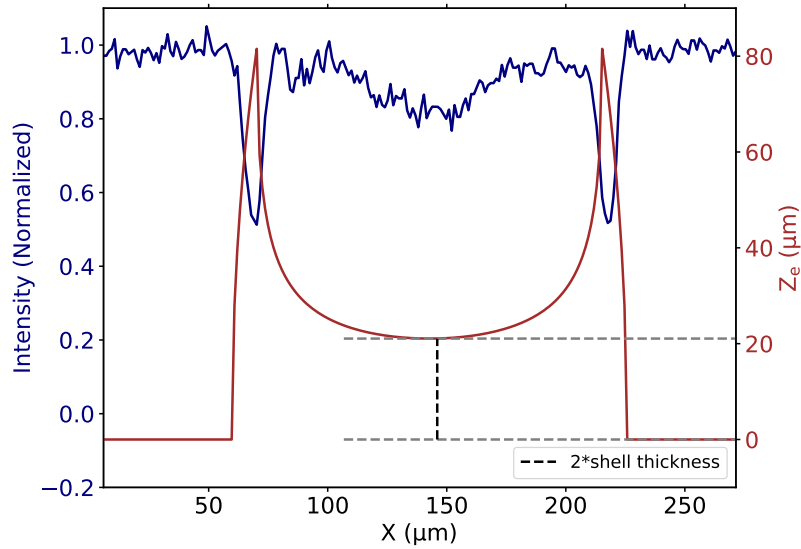
Figure 3.23: The baseline corrected normalized intensity profile (blue) and an appropriate effective path length (Z_e) derived from the wings marked by the black dashed lines.
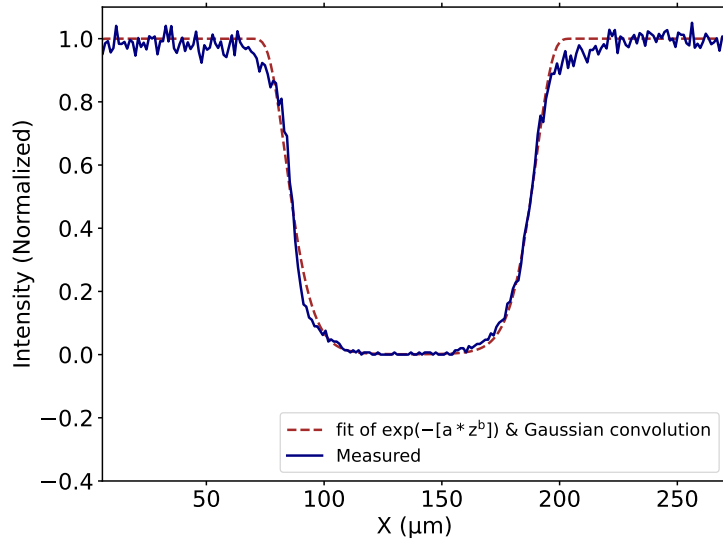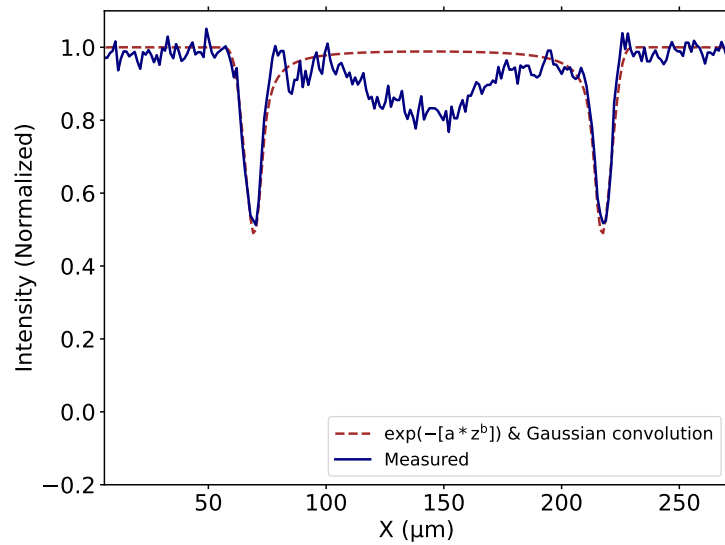

Figure 3.24: Normalized intensity profile (blue) and $I(Z_e)$ with Gaussian convolution (brown dashed line), where the parameters for $I(Z_e)$ were predetermined using the nascent spalls. When estimating the shell thickness, the intensity increase in the center of the bubble caused by the droplets is not taken into account.
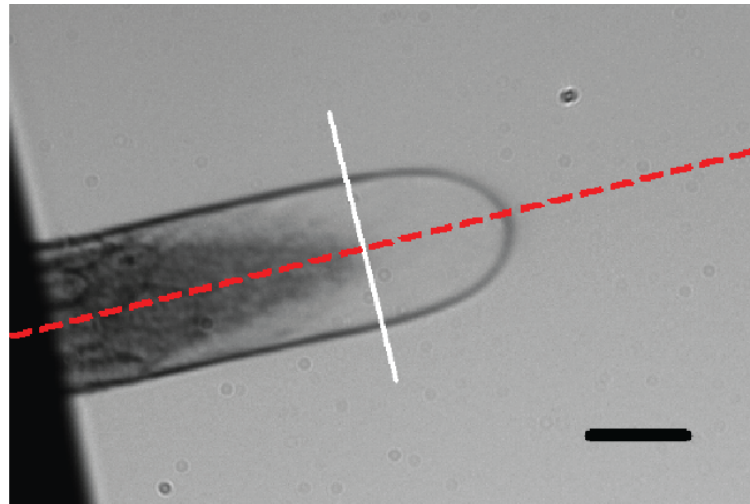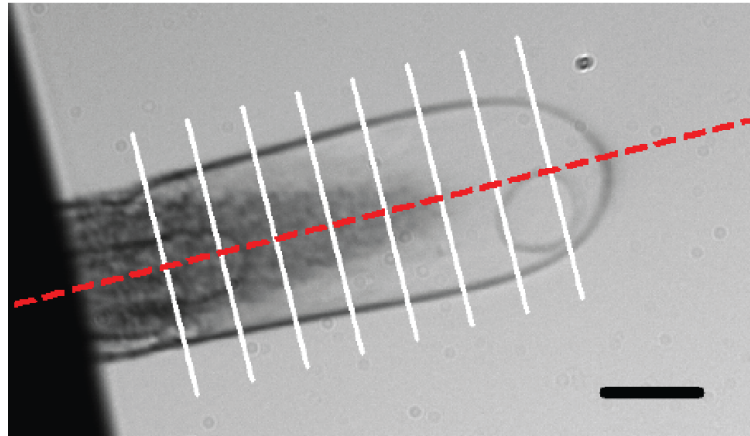
Figure 3.25: A bubble for a delay of $\Delta t = 2.0$ μs with the red dashed line indicating the z-axis along which the intensity profile locations are determined. The white line indicates the locations of the intensity profile used for thickness estimation in Figure 3.26. The black scale bar corresponds to 100 μm.
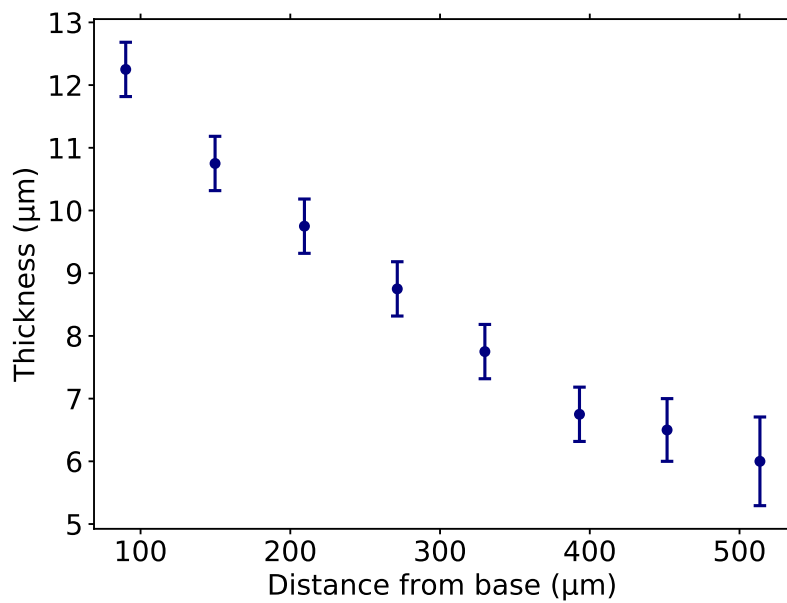
Figure 3.26: Intensity profile locations vs. shell thickness estimates, where the profile locations are shown in Figure 3.25.

The thickness determination has an estimated relative error of 20%. In addition, profiles with negative peaks consisting of less than three pixels were not considered for thickness estimation. The reduced number of data points on the intensity profile could lead to inaccurate estimates. Although the problem of reduced data points can be adequately addressed by interpolating the data, we did not do so because the method gave satisfactory results without interpolation. Therefore, for thicknesses below 3 μm, which are usually observed near the tip of the shell, the method described here is not used.

The results we obtained from the spall depth measurements and the thickness measurements are in agreement, suggesting a higher thickness for the parts closer to the bulk compared to those farther from the bulk. However, we cannot attribute spall depth alone as the cause of this feature, because other flow mechanisms, such as the one that causes bubble tip elongation discussed later, may be involved.

3.3.2. Bubble film retraction velocity

As mentioned in the introduction, studying the dynamics of fractures in bubbles provides valuable insights. A primary step in understanding the dynamic of such bubble fractures is to calculate the Taylor-Culick velocity (TCV), which can be determined as follows,

$$v_{TC} = \sqrt{\frac{2\sigma_{ST}}{\rho\delta}} \tag{3.17}$$

where σ_{ST} is the surface tension of the liquid, ρ is the density of the liquid, and δ is the thickness of the retracting film.

Using the thickness estimates ($5 - 15$ μm) we obtained from the Section 3.3.1 for bubbles produced using the ablation fluence of 242 ± 11 mJ/cm^2, the TCV is supposedly between $4.5 - 2.6$ m/s[14]. Note that the viscosity of glycerol is not included in the calculations. In the case of highly viscous films [102–104], the behavior of film retraction changes for the initial growth. Fracture growth is initially exponential for high-viscosity films. It later changes to linear behavior and again to constant velocity. The film retraction speed then converges to the TCV.

---

[14]Calculated for glycerol with surface tension $\sigma_{ST} = 63.4 \times 10^{-3}$ N/m and density $\rho = 1260$ kg/m^3

Bubble rupture mechanisms have been studied extensively, with a focus on resolving the influence of elasticity. Tammaro et al. and Sabadini et al. studied this by creating bubbles with viscoelastic mixtures of micelles and oligomers [45, 105, 106] and observing the rupture using time-resolved imaging techniques. They found that when elasticity comes into play, the fracture retraction speed increases. In their system with known viscoelasticity, this was up to 30 times the velocity predicted by Equation 3.17[15]. Fitting the bubble fracture radius vs. delay data with a simple linear
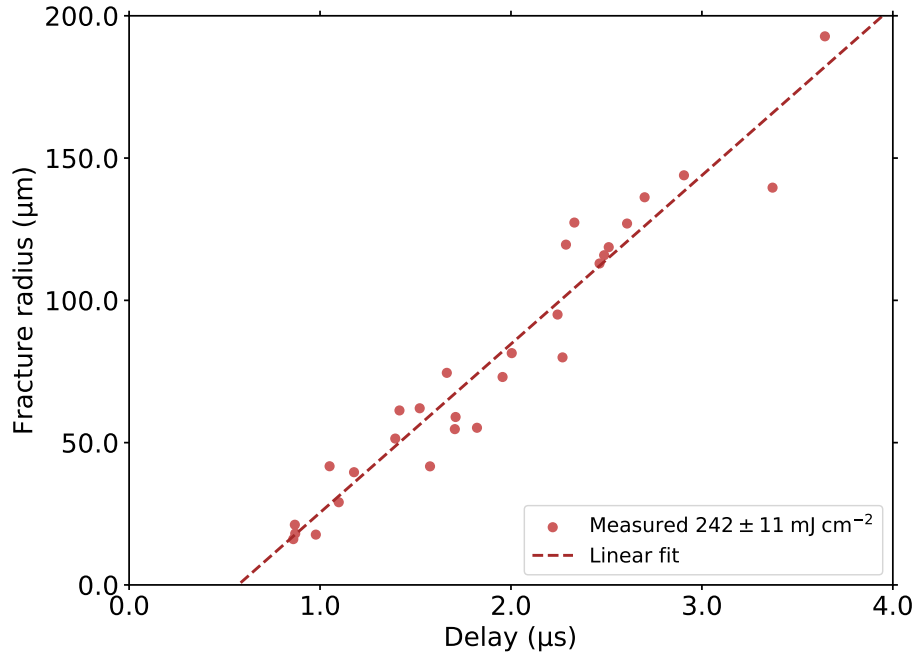
Figure 3.27: The radius of fracture versus delay time and the linear fit to the data.

fit as shown in Figure 3.27 gives us a velocity of $v_{exp} = 59 \pm 3$ m/s, which is about $15 - 20$ times higher than the Taylor-Culick velocity we calculated using Equation 3.17. It is possible that v_{exp} underestimates the TCV in our situation because the linear fit assumes that all holes are created at approximately $t_b = 0.57$ μs.

The method used to measure the diameter of the fracture assumes that the fracture occurs on a hypothetical flat 2D surface, whereas the bubble shell has a 3D curvature. Therefore, the measured diameter may not reflect the actual distance traveled by the edge during the fracture. In addition, the fractures may appear non-circular depending on their location on the shell and also due to the 3D curvature, as shown in Figure 3.28. To account for this discrepancy, the greatest distance between two

---

[15]TCV calculated without considering elasticity

points of the fracture on the projected image is used as the fracture diameter. While this may result in an underestimate of the actual fracture radius for certain fracture locations, it provides a good estimate of the fracture radius in most cases.
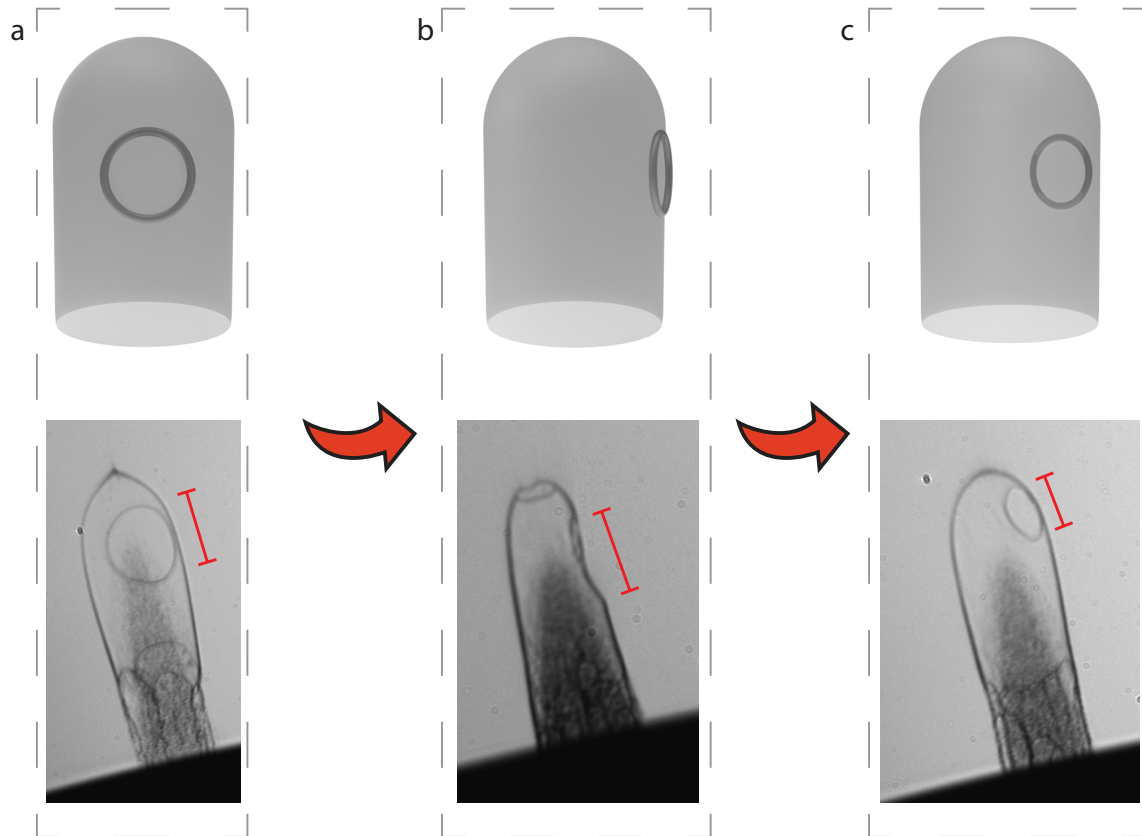
Figure 3.28: The figures show representative experimental projections of hole positions compared with abstracted representations: **a)** Shows both experimental and abstracted hole positions that retain a circular projection. **b)** Demonstrates a hole position on the wall rotated almost 90° from the viewing direction, which corresponds to a 90° clockwise rotation of the projection shown in A around the cylindrical symmetry axis. **c)** Depicts a hole position on the back wall facing away from the camera, which corresponds to about 120° clockwise rotation of the projection shown in A around the cylindrical symmetry axis. Figure adapted from [21].

3.3.3. Estimation of elastic moduli from bubble fracture

According to Taylor and Culick, when a thin film[16] is punctured, the hole growth with a constant velocity v can be described by the energy balance between surface tension forces and inertia[43],

$$F = \frac{d}{dt}(mv) = v\frac{dm}{dt} = 2\sigma_{ST} \tag{3.18}$$

where σ_{ST} is the surface tension. Equation 3.18 can be written in terms of energy conservation, expressed in polar coordinates (r, α), where r_0 is the radius of the hole and α_0 is the azimuthal angle, as follows,

$$\sigma_{ST}r_0^2\alpha_0 = \frac{1}{2}\rho r_0^2\alpha_0\delta v^2 \tag{3.19}$$

where LHS is the free surface energy of the fracture region (usually determined by the surface tension σ_{ST}) and RHS is the kinetic energy of the rim. Previous approaches to introduce elasticity [107] have been to add elastic components to the RHS. This was done for static viscoelastic films where the characteristic time scale t_0 was significantly longer than the viscoelastic relaxation time τ_{rel}. The reasoning was that the energy required for the elastic transformations of the moving rim would come from the surface energy, resulting in a reduced TCV.

However, t_0 is comparable to τ_{rel} in our case. Therefore, we can introduce an elasticity term (E_{el}) to the LHS of Equation 3.19, resulting in an increased surface energy compared to situations with only surface tension contributions. To aid in this process, we can think of the bubble as a membrane that exhibits neo-Hookean elastic behavior. Neo-Hookean materials exhibit a characteristic elastic behavior in which the stress-strain behavior is linear up to a certain point, after which the strain reaches a plateau. The model is typically used to predict the behavior of materials such as rubber under tension [108].

Assuming that the bubble is a neo-Hookean membrane, we can derive the elastic energy of the shell. The volumetric energy for a neo-Hookean incompressible material is given by [108],

$$E_{el} = \frac{1}{2}G(t)\Lambda \tag{3.20}$$

---

[16]Typically used for soap and low viscosity films.

Where $G(t)$ is the shear relaxation modulus and Λ contains strain ratios for three principal axes ($\Lambda = \lambda_1^2 + \lambda_2^2 + \lambda_3^2 - 3$). These strain ratios can be used to describe the transition from an undeformed (x_0, y_0, z_0) to a deformed (x, y, z) state under affine deformation assumptions.

$$x = \lambda_1 \times x_0, \ y = \lambda_2 \times y_0, \ z = \lambda_3 \times z_0 \tag{3.21}$$

Where an affine transformation consists of a linear transformation that preserves parallelism (e.g., rotation, shearing, stretching, and compression), but not necessarily Euclidean distances and angles.

The shear relaxation modulus, $G(t)$, sometimes referred to as rigidity, is a property we will encounter as we explore the field of viscoelasticity. It can be thought of as the shear stress remaining in a material at time t after an initial shear strain has been applied. The storage modulus ($G'(\omega)$)[17], which is often encountered as a result of the dynamic mechanical analysis measurements used to characterize viscoelasticity, and $G(t)$ are related as follows,

$$G_\infty = \lim_{\omega \to \infty} G'(\omega) = \lim_{t \to 0} G(t) \tag{3.22}$$

where G_∞ is the high frequency shear modulus. Both $G(t)$ and $G'(\omega)$ are measures of the elastic energy stored in a material. One may intuitively associate these quantities thinking that a dynamic measurement at ω frequency could be equivalent to a transient measurement at $t = 1/\omega$, but this is not the case. $G'(1/t)$ and $G(t)$ can be very different in all situations other than $t \to 0$ or $\omega \to \infty$ [109].

Solving for the TCV after including the elastic term (E_{el}) yields,

$$v_{el} = \sqrt{\frac{G(t)\Lambda}{2\rho} + \frac{2\sigma}{\delta\rho}} = \sqrt{\frac{G(t)\Lambda}{2\rho} + v_0} \tag{3.23}$$

where v_0 is the TCV before elasticity was introduced. Solving for $G(t)$ gives,

$$G(t) = (v_{el}^2 - v_0^2) \times \frac{2\rho}{\Lambda} \tag{3.24}$$

If $v_{el} \gg v_0$ we have,

$$G(t) \approx v_{el}^2 \times \frac{2\rho}{\Lambda} \tag{3.25}$$

The inflation dynamics of the bubble can be thought of as the biaxial elongation of a sheet [108], and in this case Λ is well described as follows,

$$\Lambda = \lambda_1^2 + \lambda_2^2 + \lambda_3^2 - 3 \tag{3.26}$$

---

[17]Refer to the Appendix B

Assuming incomprehensibility for the shell, we describe the strain ratio along the third principal axis in terms of the other two ($\lambda_3 = \frac{1}{\lambda_1 \times \lambda_2}$),

$$\Lambda = \lambda_1^2 + \lambda_2^2 + \frac{1}{\lambda_1^2 \times \lambda_2^2} - 3 \tag{3.27}$$

From the increased strain we observe for the bubble along the z-axis, we believe that the strain ratios along the z-axis (λ_1) and along the circumference (λ_2) are different as $\lambda_1^2 >> \lambda_2^2$. But the holes developing on the shell do not seem to deviate from circular symmetry as they should if our assumption ($\lambda_1^2 >> \lambda_2^2$) is correct. Therefore, we can assume that the two strain ratios are approximately equal ($\lambda_1 \approx \lambda_2 = \lambda$). This reduces Equation 3.26 and we get,

$$\Lambda = 2\lambda^2 + \frac{1}{\lambda^4} - 3 \approx 2\lambda^2 - 3 \tag{3.28}$$

Using this Λ in Equation 3.25, we get,

$$G(t) \approx v_{el}^2 \times \frac{\rho}{\lambda^2 - 1.5} \tag{3.29}$$

Knowing the bubble surface area and thickness at a delay of $\delta t = 2$ μs, we inferred $\lambda^2 = 11$, corresponding to the change in shell thickness assuming no material flow. Substituting this value into Equation 3.29, we get $G(t) = 0.48$ MPa. This is an upper estimate for two reasons. First, the denominator in Equation 3.25 is reduced by the assumption of equi-biaxial straining. Second, to obtain $\lambda = 11$, we assumed a location-independent shell thickness, which is incorrect because the shell typically becomes thinner toward the tip and the local strain ratios may eventually exceed the average. However, the elasticity values that we derived using the bubble fracture and bubble growth model are on the same order of magnitude, giving us a qualitative understanding of their magnitude.

As we discussed earlier, $G(t) \neq G'(\omega = 1/t)$. However, it may still be illustrative to compare the value we have for $G(t)$ with existing measurements. For this we used an estimated relaxation time of 10 μs during which our bubble dynamics occur. Table 3.4 summarizes the elasticity-related dynamic mechanical analysis measurements made in liquid glycerol over time at various frequencies and the corresponding storage modulus ($G'(\omega)$) values, including our estimated storage modulus.

Frequency	G'	Temperature
$f > 25$ GHz	2.4 GPa	293 K [110]
14.7 MHz	23 MPa	295 K [111]
10 MHz	15.4 MPa	293 K [112]
0.1 MHz (this work)	0.48 MPa	> 295 K
$f < 1$ Hz	100 Pa	295 K [52]

Table 3.4: G' values from literature and our estimate. Table adapted from [21].

3.3.4. Bubble-tip elongation

One of the interesting results of the lift-off is the jetting we observe at the tip of the bubbles for delays longer than 3.0 μs, as shown in Figure 3.29 a and b. Above this delay, a special needle-like jet forms at the top of the bubble, which increases in length with time. We measured the elongation of this jet with respect to the delay as shown in Figure 3.29 c. A linear fit to the data points gives an elongation velocity of 92 ± 8 m/s.

The formation of the jet at the tip of the bubble results from mass transport across the shell. Liquid transport of a similar nature is also observed in the LIFT process [80], which is based on a pressure gradient. Comparable jetting has also been reported after spallation of molten metals [113], which is explained by capillary forces. However, due to the high capillary number of about 6400 for the laser-driven glycerol bubbles (see Appendix E), the effect of capillary forces can be considered negligible. In contrast, we are of the opinion that this mass transport is a consequence of the elastic energy storage in the shell. This can be compared to the case of an inflated balloon. When the balloon is popped at one pole (here, lift-off from the bulk), the shell is pulled to the opposite pole. In our case, the lateral momentum components in the plane of the bulk surface cancel out for the rotationally symmetric influx to the tip, but the unbalanced z-components culminate in a narrow jet in the z-direction.
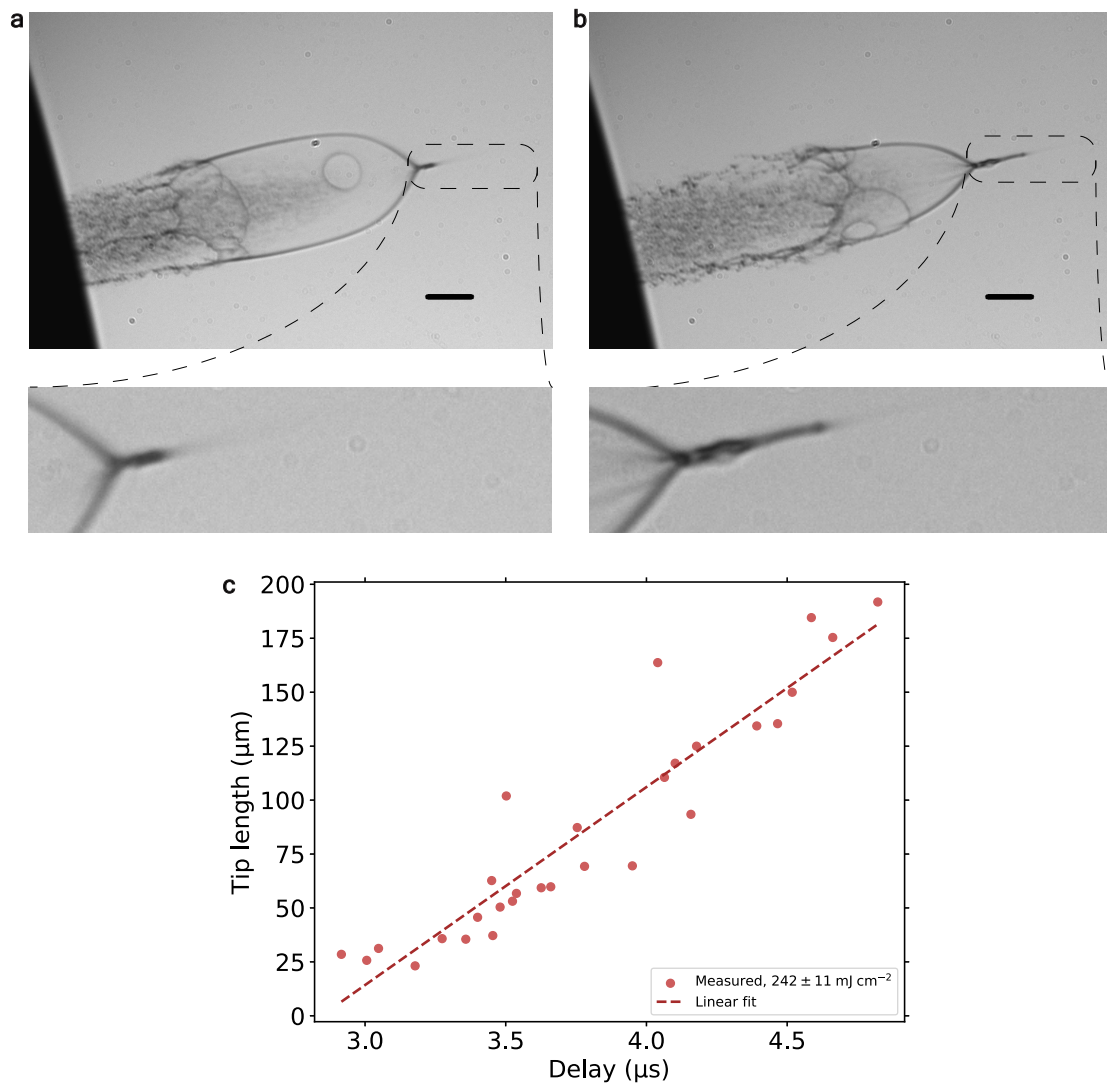
Figure 3.29: The figures show observations of bubble lift-off and tip jetting at a peak laser fluence of 242 ± 11 mJ/cm^2: **a)** At a delay of 3.6 μs, a snapshot of the bubble shows lift-off from the bulk and the onset of tip jetting (with a tip length of approximately 60 μm). A zoomed image is also provided. The black scale bar represents 100 μm. **b)** Similar to (**a**), but taken with a delay of 4.4 μs, the bubble has significantly disintegrated and the tip jet has grown to a length of about 130 μm. The black scale bar corresponds to 100 μm. **c)** A plot of the tip jet length versus delay, along with the linear fit to the data. From the linear fit, we get a tip elongation speed of 92 ± 7 m/s. Figure adapted from [21].

3.4. Remarks

The photomechanical spallation-induced metastable bubbles observed in our experiments are a novel discovery in the field. Through careful analysis of the data covering areas such as laser-matter interaction, rheology, and bubble fracture, we were able to provide a clear explanation for the formation, growth, and rupture of the laser-induced surface bubbles.

At the strain rates we observe in this system for a specific time window well above the molecular relaxation time, glycerol appears to behave more like a simple Maxwell material[18] than a Newtonian fluid. The simplest macroscopic model to explain the dynamics of such a system is a Maxwell-like model $\eta_A = \tau_A \times G'$ with dynamic viscosity η_A, apparent relaxation time τ_A and a $G' << G_\infty$, where $G_\infty = \eta/\tau_m$ is the instantaneous shear modulus [53]. Following such a description, the bubble formation can be described in terms of the elastic manifestation of the viscosity below the apparent relaxation time τ_A.

The viscosity of glycerol is shown to increase significantly[19] during shock loading studies[58], suggesting an increased relaxation time[47]. We cannot give a conclusive estimate of the viscosity changes in our system, as we are still observing the hole-opening dynamics of the type of non-viscous fluid.[20]. Therefore, we do not have a good estimate for the relaxation time (τ_A).

An increase in viscosity can explain an increase in relaxation time (τ_A) [47]. Such an increased relaxation time of a few tens of microseconds can also explain the appearance of elasticity that we have in our bubble. The rubber-like elasticity observed in liquid glycerol is the first of such direct observations of the property outside of indirect rheological measurements, which examined the low-frequency elasticity in liquid glycerol [52, 59].

---

[18]Maxwell materials exhibit properties of viscous flow over long periods of time, with additional elastic resistance in response to rapid deformations.

[19]Approximately $\eta_A = 10$ Pa.s for glycerol at a strain rate of 10^6 s^{-1} [58].

[20]The fracture edge moves at a constant velocity in our system. In the case of highly viscous fluids, the fracture growth is initially exponential. However, it is not yet clear whether an order of magnitude increase in viscosity from 1.4 Pa.s $\rightarrow$ 10 Pa.s can produce this effect.

However, the molecular origin of these unexpected behaviors in liquids still lacks satisfactory explanations. Therefore, further theoretical modeling and investigation of the phenomena must be actively pursued to better understand the most fundamental questions about the nature of the liquid phase. In conclusion, the laser-driven bubble has provided a means of studying the fundamental elastic properties of liquids from a new vantage point.

Part II

Chapter 4

Fundamentals of gas and liquid phase electron diffraction

This chapter presents the current state of the art in gas and liquid electron diffraction. The discussion includes a demonstration of how to simulate the diffraction pattern and the radial distribution function, providing a simple implementation approach using any high-level programming language.

Electron diffraction is a technique used to study matter by firing electrons at a sample and analyzing the resulting interference patterns[1]. In the case of gaseous samples, inter-atomic distances in a molecule can be resolved with very high spatial resolution by analyzing the interference of the scattered electron waves. Time-resolved electron diffraction takes this capability a step further by allowing the direct determination of atomically resolved structural changes in a system over time. Ultrafast electron diffraction (UED) is a specific branch of time-resolved electron diffraction that focuses on capturing dynamics on the femtosecond (10^{-15} seconds) timescale. In UED, an ultrafast[2] electron pulse probes a sample that has been excited by an ultrafast laser pulse, as shown in Figure 4.1. The temporal resolution of the dynamics is typically determined by the pulse length of the electron pulse. UED allows the study

---

[1]Electrons, as elementary particles, exhibit the dual properties of both particles and waves. They have the ability to both collide with other particles and undergo diffraction, similar to light.

[2]As technology advances, the definition of "ultrafast" evolves accordingly. Currently, we refer to pulse lengths τ_l below a few picoseconds as categorically ultrafast.

of rapid structural changes and dynamics in materials with unprecedented temporal resolution. UED has become a powerful tool for studying ultrafast processes such as chemical reactions [114], phase transitions [115], and lattice dynamics [116], providing valuable insights into the fundamental mechanisms governing these phenomena. To understand the significance of the research described in this thesis, it is helpful to review the history of electron diffraction and some of its milestones. A detailed review of the early development of electron diffraction with special emphasis on gas-phase electron diffraction can be found in the reference [117], and reviews of time-resolved gas-phase and condensed-phase electron diffraction can be found in the references [118, 119].
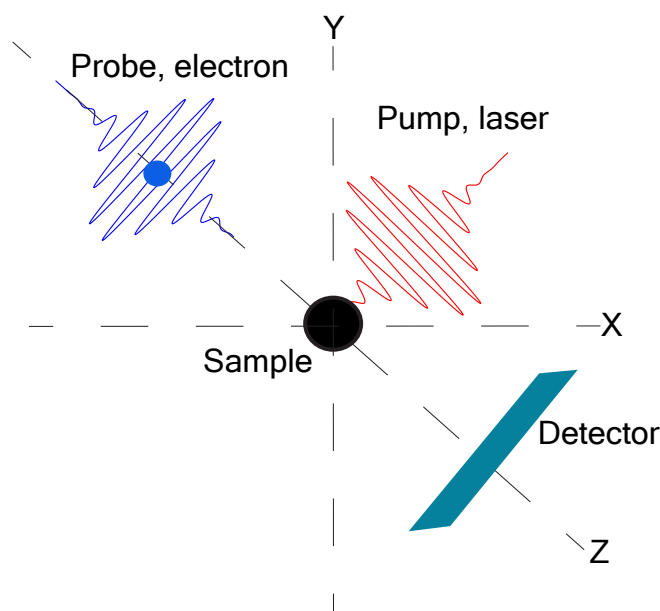
Figure 4.1: Simplified description of a time-resolved electron diffraction measurement. The arrangement of the pump-probe geometry can vary depending on the application. The probe electron pulse is shown in blue, while the pump laser pulse is shown in red. Valuable information about the time-dependent transformations taking place in the sample is obtained by analyzing the variation of the electron diffraction pattern as a function of the time delay between the pump and probe pulses.

With the advent of ultrafast amplified lasers and more efficient detectors in the late 1990s, Ahmed Zewail's group demonstrated the usefulness of time-resolved diffraction with gaseous samples [120] on picosecond time scales not previously achievable. In the early 2000s, the field was pushed further into better time resolution of a few hundred

femtoseconds on solid samples by Siwick et al. [115]. Currently, the field has evolved to reach the fundamental timescales necessary (few tens of femtoseconds) to study atomically resolved dynamics. With the increasing prevalence of advanced measurement techniques such as serial electron diffraction, microcrystal electron diffraction, mega-electron-volt (MeV) electron diffraction, etc., it may become possible to elucidate the atomically resolved dynamics of moderately large molecular systems with excellent time resolution. However, a remaining bottleneck in the field is the stringent requirements that the sample of interest must meet in order to perform the above mentioned studies. Much research has been done to improve the accessible sample space for electron diffraction with mixed results.

The gas nozzle sample delivery mechanism for time-resolved electron diffraction is a proven method for gases and high vapour pressure liquids such as 1,3-cyclohexadiene (CHD)[3] [114, 121]. However, the sample space is limited due to the inherent limitations of the available systems of interest. Gas nozzle design and integration into an electron diffraction instrument becomes difficult for corrosive and polymerizing substances such as CF_3I and CHD. Another hurdle in the gas nozzle technique is the issue of velocity mismatch [122]. When an optical pulse and a non-relativistic electron pulse propagate through a medium, their group velocities[4] can differ. This group velocity mismatch can cause two initially overlapping pulses to lose their temporal overlap after a certain distance of propagation. Consequently, as the pulses propagate through a relatively large volume of gas produced by the gas nozzle, this group velocity mismatch can result in significant smearing of the time resolution [123]. However, the velocity mismatch problem in gas phase UED has recently been overcome by using MeV electrons as the probe [124].

For solid samples, there is a well-established method of sample delivery. Ideally, thin slices less than 100 nanometres thick should be cut from either single crystals, polycrystals or amorphous samples. The use of thin samples also avoids the problem of velocity mismatch when probing the system with non-relativistic electron pulses. In addition, thin samples reduce the likelihood that an electron, once scattered by one atom, will be scattered by another atom, which could affect the information acquired about the sample.

---

[3]A commonly studied sample known to exhibit interesting ultrafast ring opening and closing dynamics.

[4]Group velocity refers to the velocity at which the envelope of a pulse propagates through a medium.

99

When using time-resolved electron diffraction to study changes in the molecular structure of solid samples, it is critical to consider an important limitation. The molecular structure of the sample can be significantly altered by interaction with a pump pulse, potentially rendering the sample unsuitable for subsequent experiments, especially if the structural change is not reversible. This limitation is particularly relevant in experiments that rely on the accumulation of pump-probe measurements to obtain meaningful information.

The use of thin liquid sheets confined by air [125] and thin liquid cells confined by a solid window material [126], as in the case of liquid electron microscopy, have attracted considerable attention as methods for liquid sample delivery. Recent publications based on these approaches [127, 128] have shown encouraging results. Theoretical advances have also been made in the analysis of electron diffraction data obtained from liquid phases [129]. However, it is important to recognise that these techniques are still at an early stage of development.

A notable challenge in the implementation of thin liquid films for sample delivery, particularly in smaller electron diffraction machines, is the establishment of a functional vacuum. In addition, the relatively high sample consumption is not ideal, especially when working with limited sample quantities. Overcoming the interference of confinement windows in liquid cells is also a significant hurdle.
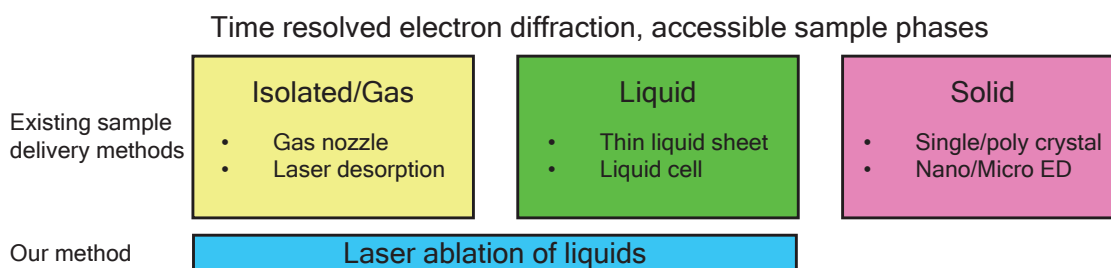
Figure 4.2: Existing sample delivery techniques for electron diffraction and their different accessible sample phases are compared. In contrast, the proposed laser liquid ablation technique offers unique advantages.

The idea of using laser ablation as a sample delivery tool for time-resolved electron diffraction is not new. Zewail's group has attempted to use plumes generated by laser desorption, described in detail in this thesis [130], for electron diffraction with thermally labile compounds. The delivery mechanism uses a glassy carbon substrate

dusted with powdered sample material[5], which is ablated by a nanosecond Nd:YAG laser[6]. Laser desorption coupled with electron diffraction has yielded some interesting results [6–8], but the delivery mechanism cannot be used for a wide sample space and therefore may not be ideal for general use in smaller electron diffraction instruments. The first part of this thesis demonstrated that it is possible to produce thin liquid bubbles and isolated gas plumes from vacuum-stable liquids by manipulating the fluence and accessing the photomechanical spallation and phase explosion regimes, respectively. By using these plumes as sample carriers, the liquid laser ablation technique could serve as a versatile tool for studying the dynamics in the isolated and condensed phases. To investigate the feasibility of using liquid laser ablation as a sample delivery mechanism, we retrofitted an existing ultrafast electron diffraction instrument and performed time-resolved electron diffraction of the ablated glycerol plumes. We reasoned that after a substantial expansion of about 4 μs, the bubble would reach a thickness that would allow electrons to probe it, or the resulting post-fracture droplets would provide a liquid phase suitable for study. In addition, by using high fluence ablation, we could also generate the gas phase.

4.1. Electron diffraction pattern simulation

The theory of electron diffraction and methods for interpreting a diffraction image have been discussed on several occasions, some of which can be found here [119, 129, 131]. Gas phase electron diffraction can be traced back to the beginning of the electron diffraction technique itself [7]. The 1936 review by Brockway [133] gives us a detailed description of the early days of electron diffraction, with emphasis on gas-phase electron diffraction.

An electron diffraction experiment produces an image with an interference pattern as a result of the scattering of electrons by the sample through which the beam has

---

[5]The glassy carbon belt is in continuous motion for sample replenishment.

[6]Neodymium-doped yttrium aluminium garnet (Nd:YAG) is a crystal used as a laser medium in solid-state lasers. These lasers typically produce infrared light with a wavelength of 1064 nm.

[7]Davisson and Kunsman in 1923 showed that structural information could be derived from electron scattering using a platinum target [132].

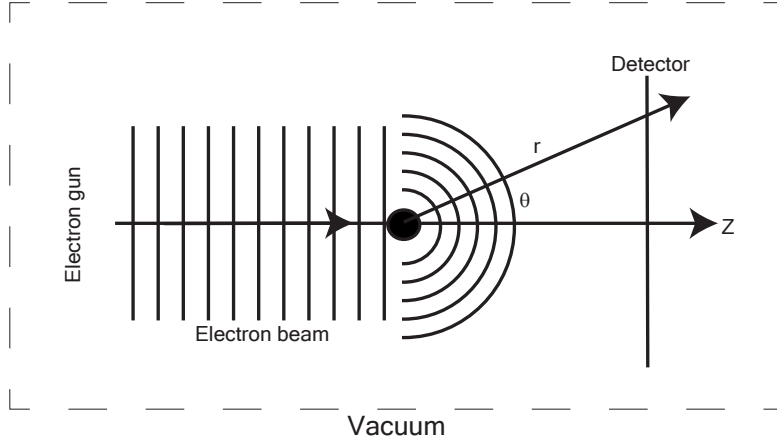passed as shown in Figure 4.3. We have to understand the possible contributions

Figure 4.3: An electron beam emitted from the photo-cathode or an electron gun travels along the z-axis and interacts with an atom. Part of the incoming electron plane wave is scattered as an outgoing spherical wave when it interacts with an atomic scattering centre. The intensity of the scattered electrons, detected at a distance r on a detector, depends on the angle θ.

contained in these images and try to untangle them in order to derive structural information about the sample. For that purpose, an electron diffraction pattern can be thought of as an intensity distribution,

$$I_{\text{tot}}(x, y) = I_{\text{sample}}(x, y) + I_{\text{bg}}(x, y) \tag{4.1}$$

where $I_{\text{tot}}(x, y)$ is the total intensity we see in the detector, I_{sample} corresponds to the contribution from the sample, and I_{bg} corresponds to other contributions[8].

To start the simulation process, it is convenient to move from real to momentum space. If we know the center of the diffraction peak and some details of the experimental setup, we can rewrite the intensity terms of Equation 4.1 in terms of the momentum transfer vector (s), which can be derived by the following steps,

$$d = \sqrt{(x - x_0)^2 + (y - y_0)^2} \times \text{pixel\_size} \tag{4.2}$$

$$\theta = \tan^{-1}\left(\frac{d}{\text{det\_dist}}\right) \tag{4.3}$$

$$s = \frac{4\pi}{\lambda_e}\sin\left(\frac{\theta}{2}\right) \tag{4.4}$$

---

[8]These are mostly due to multiple scattering, sensor defects, etc.

Where x_0, y_0 is the center of the diffraction peak, pixel_size is the pixel size of the detector, det_dist is the distance to the detector from the sample, and λ_e is the wavelength of the electron beam used, we can rewrite the diffraction pattern in terms of the momentum transfer vector s. The total intensity observed at the detector can then be written as follows[9] [133],

$$I_{\text{tot}}(s) = I_{\text{atom}}(s) + I_{\text{mol}}(s) \tag{4.5}$$

where I_{atom} is the atomic component and I_{mol} is the molecular component. The atomic and molecular components for randomly-oriented isolated molecules can then be written as follows [133],

$$I_{\text{atom}}(s) = \sum_{i=1}^{N} |f_i(s)|^2 \tag{4.6}$$

$$I_{\text{mol}}(s) = \sum_{i=1}^{N} \sum_{j \neq i}^{N} |f_i(s)||f_j(s)|\cos(\eta_i(s) - \eta_j(s))\frac{\sin(s \times r_{ij})}{s \times r_{ij}} \tag{4.7}$$

Where $f_i(s)$ and $f_j(s)$ are the scattering factors, which measure the scattering amplitude of incident waves[10] by the atom, $r_{ij} = |\vec{r_i} - \vec{r_j}|$ is the distance between atom i and atom j as shown in Figure 4.4. The term, I_{mol}, is used in electron diffraction experiments to extract structural information. The particular model we use ignores the phenomenon of multiple scattering. This means that once an electron has been scattered by one atom, it will not be scattered by another. We also assume that the scattering signal from the atomic bonds within the molecule is insignificant, treating the atoms as if they were independent of each other. This assumption is commonly known in the literature as the independent atom model [123].

The phase information contained in the factor $\cos(\eta_i(s) - \eta_j(s))$ of Equation 4.7 is only important if the difference in atomic numbers in a system is relatively large, since different elements can produce different phase shifts. In our case, with relatively small differences in the atomic numbers of the elements in the molecule, the molecular component can be simplified to,

$$I_{\text{mol}}(s) = \sum_{i=1}^{N} \sum_{j \neq i}^{N} |f_i(s)||f_j(s)|\frac{\sin(s \times r_{ij})}{s \times r_{ij}} \tag{4.8}$$

---

[9]Note: Both intensity terms must be multiplied by a pre-factor $\frac{K^2}{R^2}$, where $K = \frac{8\pi^2 m_e e^2}{h^2}$ and R is the distance between the scattering center and the observation point. However, these constants cancel each other out when calculating the modified scattering intensity. Therefore, to avoid complexity, they are omitted in the following equations.
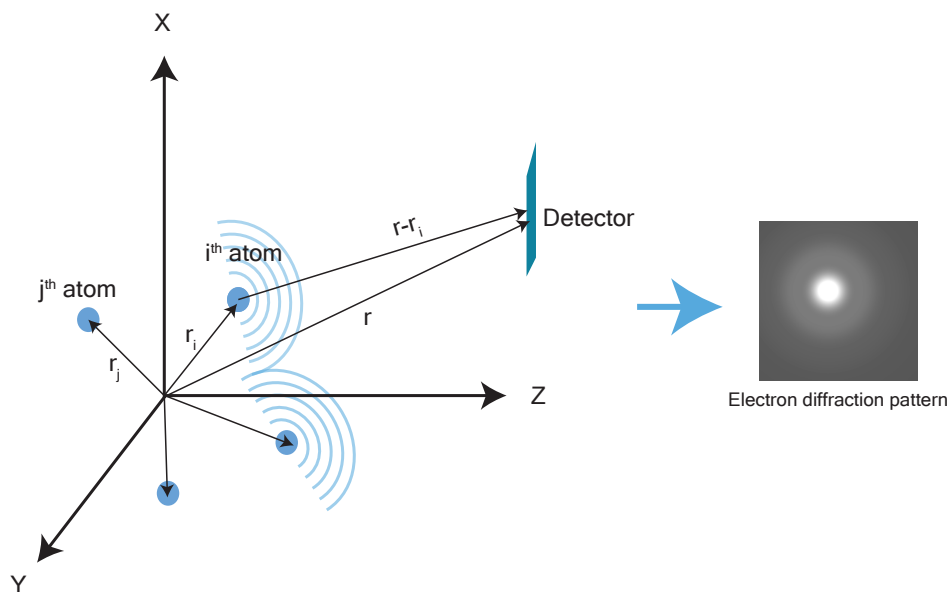
[10]In our case, electron wave.

Figure 4.4: In molecular scattering, the outgoing spherical waves interfere with each other on the detector to produce the electron diffraction pattern, which serves as a signature of the atomic positions from which the electron beam is scattered and can be used to derive structure information such as bond distances.

Obtaining structural information can be challenging when relying solely on the electron diffraction pattern. An alternative approach is to simulate a diffraction pattern based on the theoretically calculated molecular geometry and compare it with the measured diffraction pattern. Using Equation 4.5 the simulation of the electron diffraction pattern is relatively uncomplicated given that we already have information about the detector, the experiment, and the molecular geometry of the sample. The remaining parameters we need to find for the simulation of the electron diffraction patterns are the elastic scattering factors ($f_i(s)$) for the atoms of the sample.

4.1.1. Electronic scattering factors

There are several methods for calculating the electron scattering amplitude of elements, and a detailed discussion of electronic scattering factors can be found in reference [134]. For the simulation of the diffraction pattern described in this thesis,

we used the scattering factors calculated by Kirkland (1998) [131] and Lobato et al (2014). [134]. According to Kirkland, the scattering factor can be written as follows,

$$f_e(q) = \sum_{i=1}^{3} \frac{a_i}{q^2 + b_i} + \sum_{i=1}^{3} c_i \exp(-d_i q^2) \tag{4.9}$$

where a_i, b_i, c_i and d_i are the coefficients are available from [131].

In the case of Lobato et al., the scattering factor can be written as follows,

$$f_e(q) = \sum_{i=1}^{5} \frac{a_i(2 + b_i q^2)}{(1 + b_i q^2)^2} \tag{4.10}$$

where a_i and b_i are the coefficients are available from [134].

Therefore, for glycerol, the calculation of the electron diffraction pattern is a matter of choosing the correct geometry of the molecules.

To compensate for the steep decrease of the total intensity with respect to s and to make comparisons between experimental and theoretical data easier to understand, it is a common practice to use the so-called modified scattering intensity:

$$sM(s) = s \frac{I_{\mathrm{mol}}(s)}{I_{\mathrm{atom}}(s)} \tag{4.11}$$

In case of real experiments, Equation 4.11, can be written as:

$$sM(s) = s \frac{I_{\mathrm{tot}}(s) - I_{\mathrm{bg}}(s)}{I_{\mathrm{atom}}(s)} \tag{4.12}$$

4.1.2. Electron pair distribution function

The description of a crystal structure includes both the contents of the unit cell and the translation vectors that define that cell. With this information it is possible to determine the arrangement of the atoms within the crystal. However, in the case of a disordered or amorphous material, the arrangement of the atoms does not follow a strict lattice rule. As a result, it is in principle impossible to determine the exact atomic composition at any given point. Instead, the structure of such a material is characterised by a pair distribution function (PDF) [135].

The pair or radial distribution function describes the probability of finding an atom at a given distance r from another atom. By using the pair distribution function it is possible to determine interatomic and intramolecular distances, allowing us to understand the short and medium range order within these systems. To calculate the pair distribution function, a sine transformation can be applied to $sM(s)$ derived from Equation 4.11 as follows [130],

$$PDF(r) = \int sM(s)\sin(s \times r)ds \tag{4.13}$$

Generally, in gas phase electron diffraction analysis, a damping envelope function $(\exp(-ks^2))$ is used to remove ringing artifacts introduced by the truncated nature of the s domain. The electron pair distribution function then becomes,

$$EPDF(r) = \int sM(s)\sin(s \times r)\exp(-ks^2)ds \tag{4.14}$$

Where a value of $k = 0.02$ Å is typically used when it comes to gas-phase electron diffraction [130].

To benchmark the electron diffraction pattern and pair distribution function simulation programs, I generated electron diffraction patterns for CCl_4 and CO_2. These are molecules with readily available information regarding their geometry, and preexisting electron diffraction study [136]. In the case of glycerol, a pre-existing neutron diffraction study is available to verify the simulation results [137].

Based on Equations 4.5, 4.6 and 4.8 we have calculated the electron diffraction pattern for CCl_4[11], which is shown in Figure 4.5. The calculation of the electron diffraction pattern used the same experimental parameters as for the electron diffraction measurements of the laser-ablated glycerol plumes. From the simulated electron diffraction patterns we determined the electron pair distribution function using Equation 4.14, as shown in Figure 4.6.

The radial distribution function in Figure 4.6 shows very clearly two prominent peaks corresponding to the intra-molecular distances of r_{C-Cl} and r_{Cl-Cl}, in agreement with the known values of about 1.81 Å and 2.96 Å respectively.

The same procedure was repeated for the CO_2[12] to further validate the simulation procedure. The electron pair distribution curve shown in Figure 4.7 again clearly

---

[11]Geometry file from `https://cccbdb.nist.gov/` calculated with density functional theory: BLYP/aug-cc-pVDZ.

[12]Geometry file from `https://cccbdb.nist.gov/` calculated with density functional theory: B3LYP/aug-cc-pVDZ.

(a)
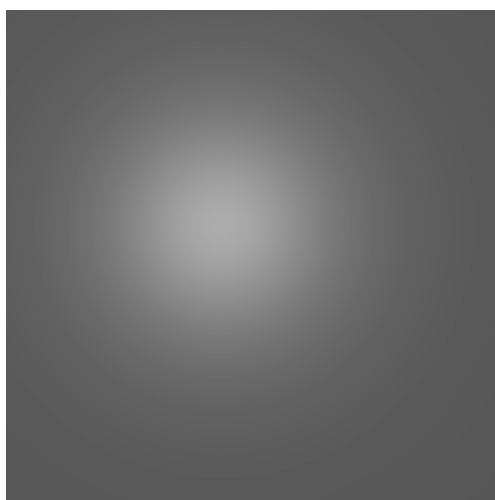
(b)

(c)

Figure 4.5: a) Simulated electron diffraction patterns according to our experimental specifications with both molecular and atomic contributions using Equation 4.5 of CCl_4, **b)** Simulated electron diffraction pattern with only atomic contribution using Equation 4.6, **c)** Simulated electron diffraction pattern with only molecular contribution using Equation 4.8. All calculations are performed using the Kirkland scattering factors [131], as given in Equation 4.9.
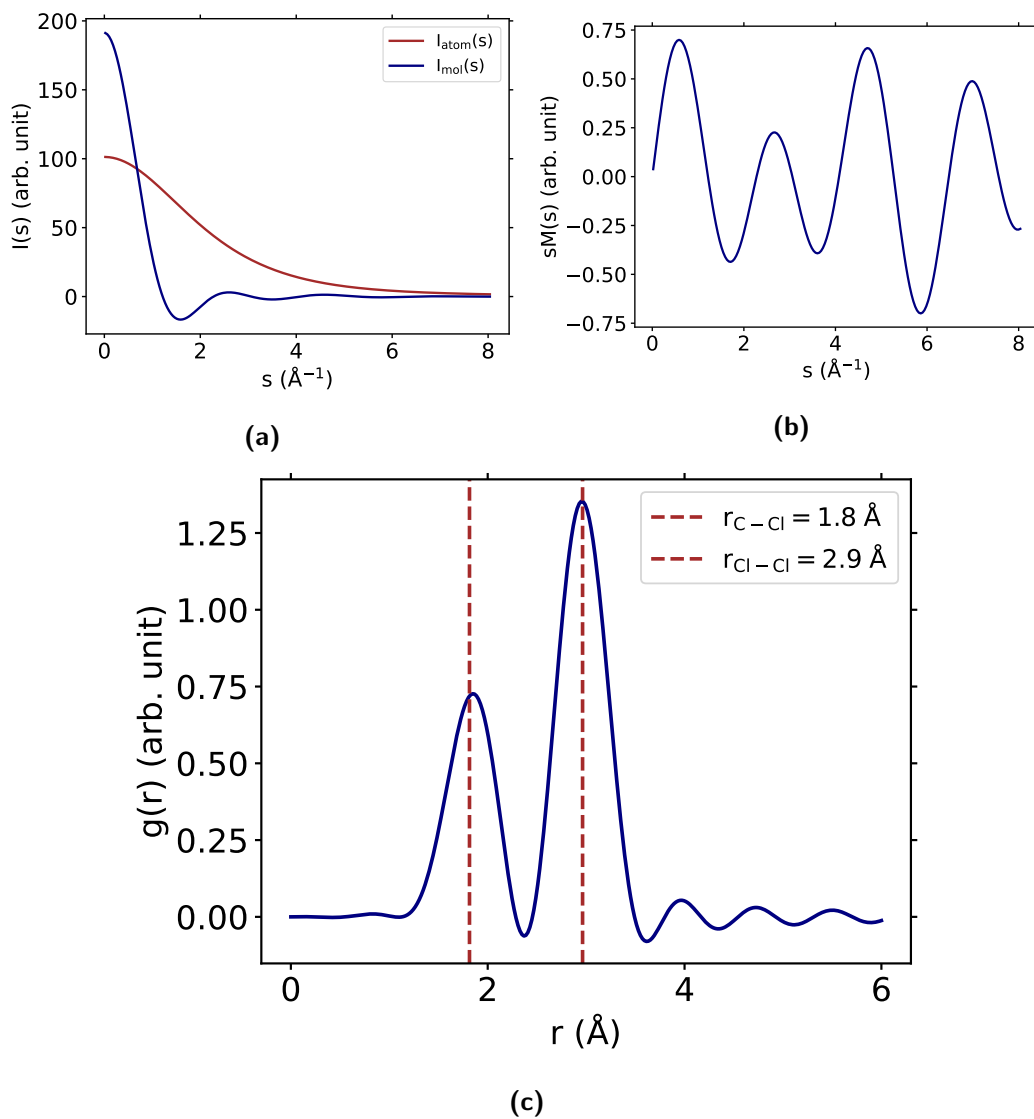
(a)

(b)

(c)

Figure 4.6: a) Azimuthal average of the total and atomic diffraction patterns of CCl_4, **b)** Modified scattering intensity calculated using Equation 4.11 vs. momentum transfer vector of CCl_4, **c)** Electron pair distribution function of CCl_4 calculated using Equation 4.14.

shows the two prominent peaks corresponding to the intra-molecular distances of r_{C-O} and r_{O-O} with the known values of about 1.17 Å and 2.3 Å, respectively.
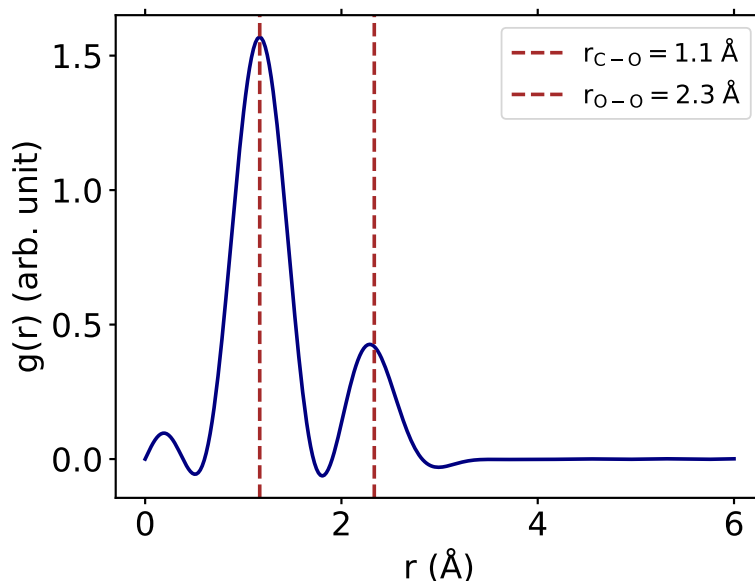

Figure 4.7: Electron pair distribution function of CO_2 calculated as per Equation 4.14.

We performed simulations for both the electron diffraction pattern and the radial distribution function of glycerol in two states: isolated glycerol and liquid glycerol. To simulate the isolated glycerol, we used an available geometry based on a conformer obtained by energy minimisation procedures[13]. On the other hand, for the liquid glycerol we used the atomic positions of hundreds of molecules to simulate the electron diffraction pattern. These atomic positions in liquid glycerol were determined using molecular dynamics (MD) simulations described in Appendix D.

As glycerol consists of 14 atoms, the electron diffraction pattern could be influenced by different conformers depending on the energy of the system after laser ablation. Although the differences in atomic spacing between different conformers are relatively small, the presence of multiple conformers may result in broader peaks in the radial distribution function.

---

[13]Geometry file from `https://cccbdb.nist.gov/` calculated using density functional theory: BLYP/aug-cc-pVDZ.

Chapter 5

Electron diffraction of ablated glycerol plumes

The chapter outlines the instrumentation used for the time-resolved electron diffraction of ablated glycerol plumes. In addition, the results of the proof-of-concept experiments are presented. Some figures and parts of this chapter are adapted from the article [20].

5.1. Experiment design

The instrumentation used for these experiments can be divided into four main components: sample delivery, electron imaging and diffraction system, optical imaging system and ablation laser. Figure 5.1 provides a visual representation of all components involved in this electron diffraction and brightfield imaging instrumentation.
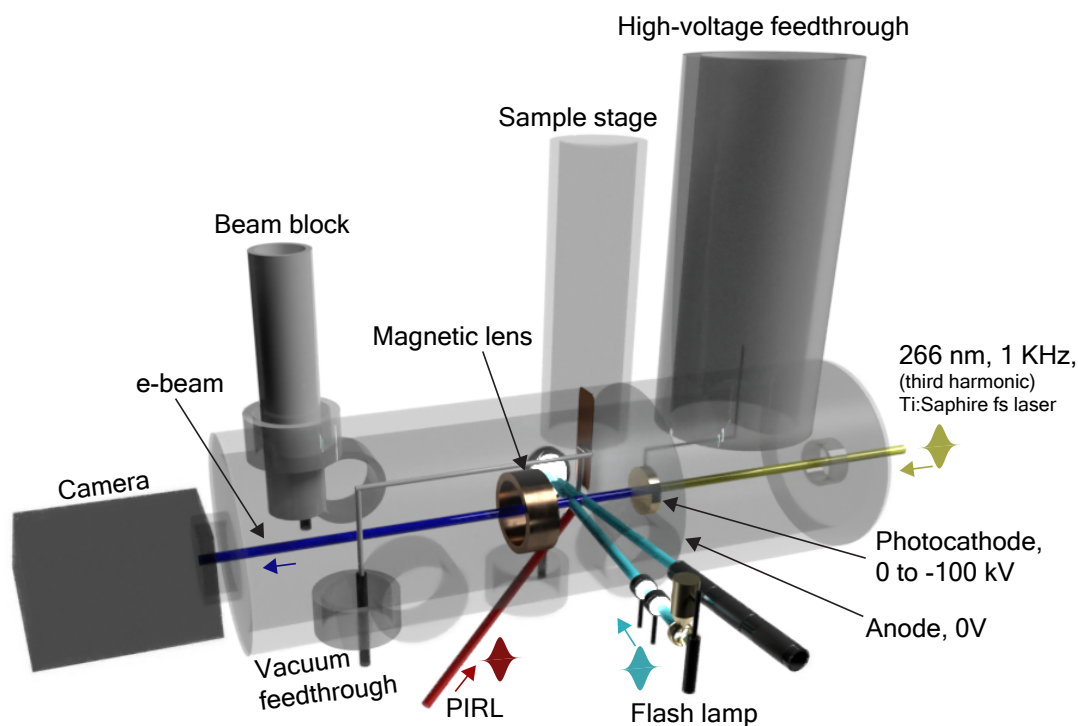
Figure 5.1: The electron diffraction and brightfield imaging apparatus is shown in a schematic diagram (not to scale). The measurements are performed in a pump-probe mode. A measurement involves the use of three pulses: a picosecond pump pulse (shown in red), which triggers the ablation of the liquid sample, and two probe pulses: a femtosecond electron pulse (shown in dark blue) and a nanosecond light pulse (shown in light blue). The electron pulse is generated by directing an ultraviolet femtosecond pulse onto a photocathode. Reproduced from [20], with the permission of AIP Publishing.

5.1.1. Brightfield imaging and sample delivery

The brightfield imaging setup has been modified and adapted to the geometric constraints of the electron diffraction instrumentation. The light source remains the same, a discharge flash lamp with a pulse duration of a few nanoseconds and a broadband white light spectrum, as described in Chapter 2. However, the illumination geometry has been modified as shown in Figure 5.2.

In the modified setup, a collector lens with a focal length of 60 mm first collects the light, followed by a field lens with a focal length of 400 mm which focuses the beam. Since there is no viewport in a convenient position[1] in the setup, a mirror is used to direct the beam to the point where the ablation laser interacts with the sample and then to the far-field microscope. The illumination path is carefully adjusted so that the plume is in the focal plane of the field lens, ensuring maximum and as uniform illumination as possible. A microscope (Qioptiq, USA) with a focal length of 300 mm is used to image the generated plume. The image was then routed to a monochrome CCD camera (DMK23U274) from Imagingsource, Germany.

To perform electron diffraction measurements, a continuous supply of sample is required. This is achieved using a sample delivery system as shown in Figure 5.3. The sample reservoir is mounted on a height adjustable frame in close proximity to the vacuum chamber shown in Figure 5.1.

The sample delivery system consists of connecting one end of a Teflon tube to the outlet of the reservoir and the other end to a stainless steel needle. This stainless steel needle is positioned inside the vacuum chamber on a sample translation stage and can be moved to position the needle tip exactly at the point of interaction where the ablation laser interacts with the sample. The internal diameter of the needle is approximately 0.45 mm.

To regulate the back pressure in the sample reservoir, one of the other outlets is connected to a turbo vacuum pump. All outlets are equipped with valves that can be finely adjusted to create the optimum pressure differential. This allows precise control of the glycerol flow.

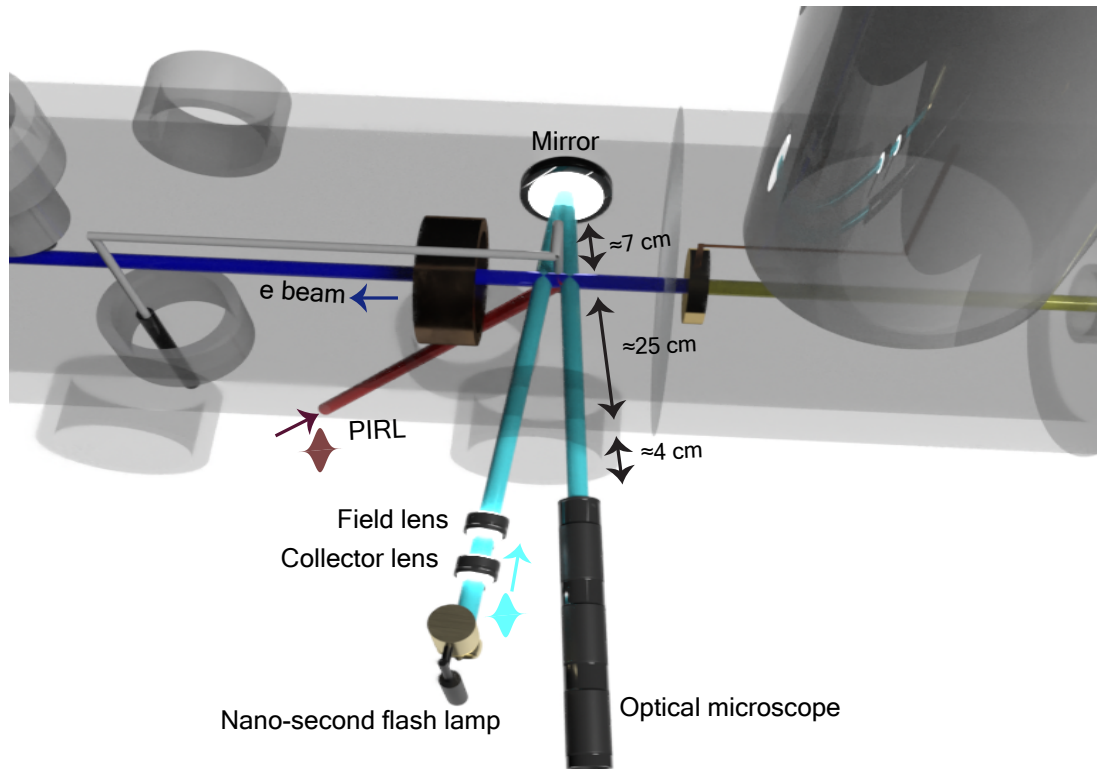
[1]Facing the arc lamp.

Figure 5.2: Schematics of the optical imaging setup. Not to scale. Reproduced from [20], with the permission of AIP Publishing.
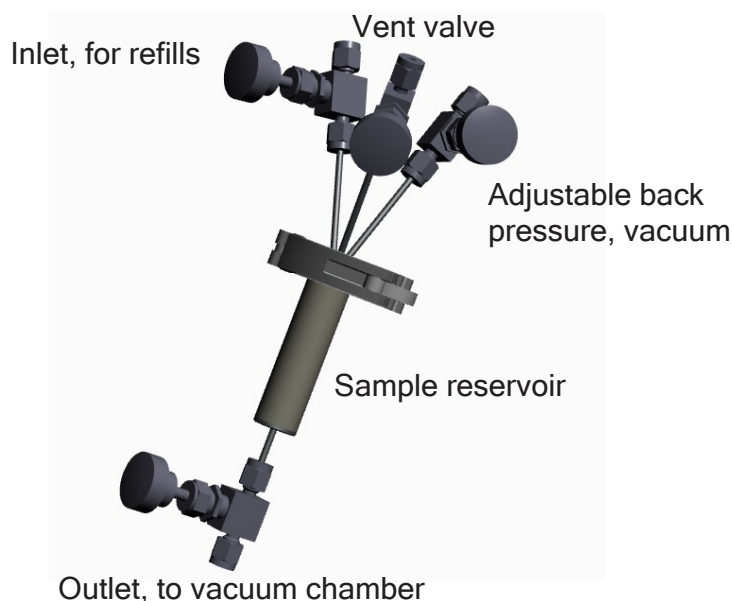
Figure 5.3: The sample reservoir for feeding vacuum stable liquids into vacuum.

5.1.2. Electron imaging and diffraction

Figure 5.1 illustrates various components of the electron diffraction instrument. The electron pulse used to probe the laser-driven plumes is generated by the interaction of a femtosecond ultraviolet laser pulse with a gold-plated photocathode. The third harmonic[2] ($\lambda_l = 266$ nm) of the Ti:sapphire laser[3] is used to excite the photocathode, which is connected to a high voltage feedthrough. A grounded anode plate with a hole for the electron pulse is positioned about 8 mm away from the photocathode. The electric field between the photocathode and the anode accelerates the photoelectrons to energies determined (50 keV in our studies) by the potential difference.

To ensure safe operation and prevent accidental electrical discharges caused by the

---

[2]Third harmonic generation is a non-linear frequency conversion process that produces optical frequencies three times higher than those of the input laser beam. The most common use of third-harmonic generation is to produce ultraviolet light.

[3]Titanium-sapphire lasers are tunable lasers that operate most efficiently at wavelengths near 800 nm.

high potential difference between the cathode and the anode, the anode is mounted on a flange that allows differential pumping between the electron gun chamber and the sample source chamber. This configuration allows the gun chamber to operate at a higher vacuum level. Two turbopumps are used to evacuate the two chambers.

A magnetic lens is mounted between the sample stage and the detector. By adjusting the electric current flowing through the magnetic lens, the magnetic field strength generated by the lens, and therefore the focal length, can be changed. This flexibility allows the plume to be imaged in both real and reciprocal space by manipulating the current through the magnetic lens [138].

5.1.3. Synchronization

The brightfield microscopy setup was synchronized in a similar way to the experiment described in Section 2.1.6, but with the addition of another probe system.

The photodiode signal from the ablation laser was used as the master trigger. Two delay generators (Quantum composer Inc., USA) were used to synchronize both the flashlamp illumination source and the femtosecond laser pulse that drove the photocathode for the electron probe pulses to the ablation pulse. The ablation and femtosecond laser systems were synchronized to operate at a repetition rate of 1 kHz. To accommodate the limitations of the flash lamp, the brightfield imaging system was set at a lower repetition rate of 1 Hz. The delay between the flash lamp, femtosecond laser and ablation laser could be adjusted using the configured delay generators.

5.2. Results and discussion

The experimental setup made it possible to perform optical imaging and simultaneous imaging in real or reciprocal space (diffraction) using electrons. Real-space imaging of the plumes using electrons was achieved by capturing the contrast derived from the cumulative number of particles intercepted by the electron beam.

The diffraction results obtained played an important role in revealing structural information about the ablated plume under investigation. These results have been analyzed and presented in forthcoming separate sections.

5.2.1. Gas phase glycerol

Referring back to the theoretical explanation given in Chapter 4, we can use the known gas phase geometry of glycerol to calculate the modified scattering function $(sM(s))$ and the electron pair distribution function $(g(r))$. The results of these calculations are shown in Figure 5.4.

Unlike simpler molecules such as CCl_4 and CO_2, for moderately complex molecules such as glycerol it is not possible to directly assign peak positions in the radial distribution to specific bond lengths or intramolecular distances as discussed in the theory section. Therefore, the most practical approach is to compare the experimental results, as shown in Figure 5.5, with the simulated results. The electron scattering amplitudes decrease rapidly with increasing s (roughly proportional to s^{-4}) [139]. The total diffraction intensity (I_{tot}) multiplied by s^2 to make the interference features more visible.

In the case of gas and liquid electron diffraction , the experimental background response contribution to the total scattering can be approximated by fitting a smooth power curve $(I_{bg} = A \times s^n)$ to I_{tot} [127] where A is a constant. Following the background removal and calculating sM(s) according to Equation 4.12, the radial dis-

tribution function can be derived from the experimental diffraction patterns. The comparison of the experimental and theoretical pair distribution function is shown in Figure 5.6.

Based on this comparison, it can be concluded that the experimental diffraction pattern obtained for plumes generated at higher ablation fluences, where phase explosion contributes to the ablation of material, contains contributions from the gas phase.

(a)

(b)

(c)
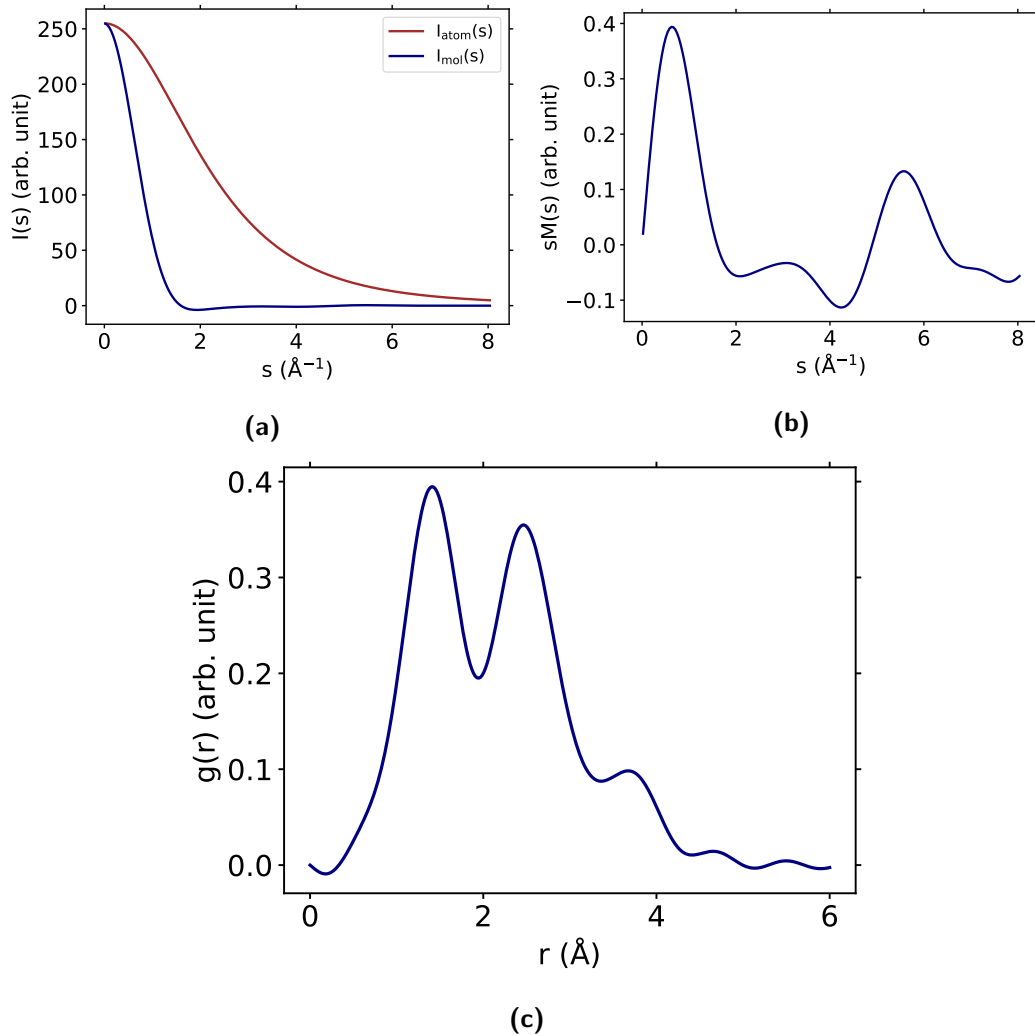
Figure 5.4: a) Azimuthal average of the total and atomic diffraction patterns, **b)** Modified scattering intensity calculated using Equation 4.11 vs. momentum transfer vector, **c)** Electron pair distribution function of gaseous glycerol calculated using Equation 4.14.

Figure 5.5: 1st row: Optical images (averaged over 50 frames) of the laser-driven glycerol plume at an ablation fluence of 450 mJ/cm^2. The white scale bar corresponds to 200 μm. **2nd row**: Electron real space images (averaged over 550 frames) of the laser-driven glycerol plume. The white scale bar corresponds to 200 μm. **3rd row**: Electron diffraction images ($I_{tot} \times s^2$, averaged over 2750 frames) of the laser-driven glycerol plume. Each row corresponds to a different delay as overlaid above. The white scale bar corresponds to 20 nm^{-1}. Reproduced from [20], with the permission of AIP Publishing.
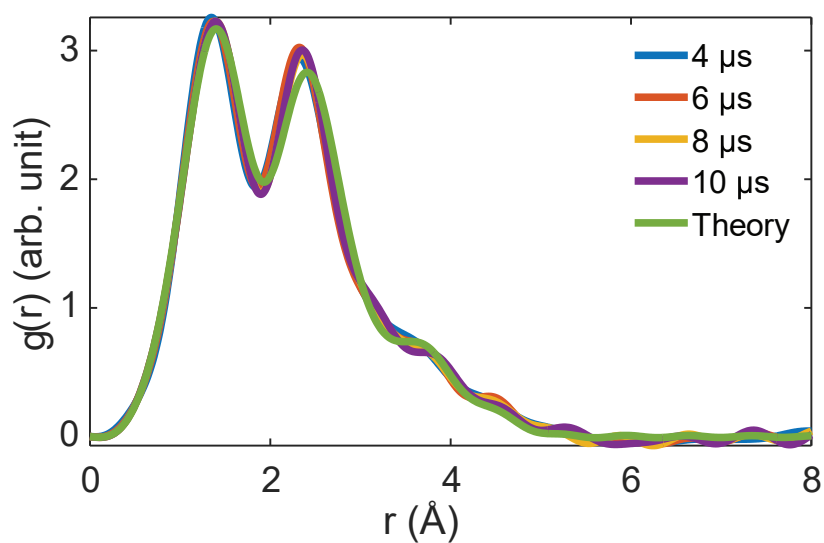
Figure 5.6: The electron pair distribution curves for plumes generated by a 450 mJ/cm^2 ablation fluence at different delays, plotted against the theoretical electron pair distribution for isolated glycerol. Reproduced from [20], with the permission of AIP Publishing.

5.2.2. Liquid phase glycerol

The theoretical radial distribution function for the liquid phase, shown in Figure 5.7c, is derived using the theory explained in Section 4.1. The structural information used in the derivation is generated by molecular dynamics simulations as described in Appendix D.

When the laser-driven bubble is probed with an average ablation fluence of 220 mJ/cm^2, a clear and prominent interference ring is seen in the inner part of the diffraction image. This ring, clearly visible for 4 μs delay in Figure 5.8, corresponds to the intermolecular interactions that exist in liquid glycerol. The presence of this feature at a scattering vector of 1.6 Å^{-1} is consistent with the results of a neutron diffraction study by Towey et al. [137] using liquid glycerol. In addition to the absence of the feature in the plume generated at high fluence of 450 mJ/cm^2, where there is no laser-induced bubble formation, the feature also disappears at later delays when the laser-induced bubbles have completely disintegrated. This supports the idea that the observed feature may be related to the presence of the laser-induced bubbles.

Figure 5.9 shows a comparison between simulated and measured radial distribution curves for liquid phase glycerol. From this comparison it can be concluded that the experimental diffraction pattern obtained for plumes generated at lower ablation fluences, where photomechanical spallation contributes to bubble generation, predominantly contains contributions from the liquid phase.
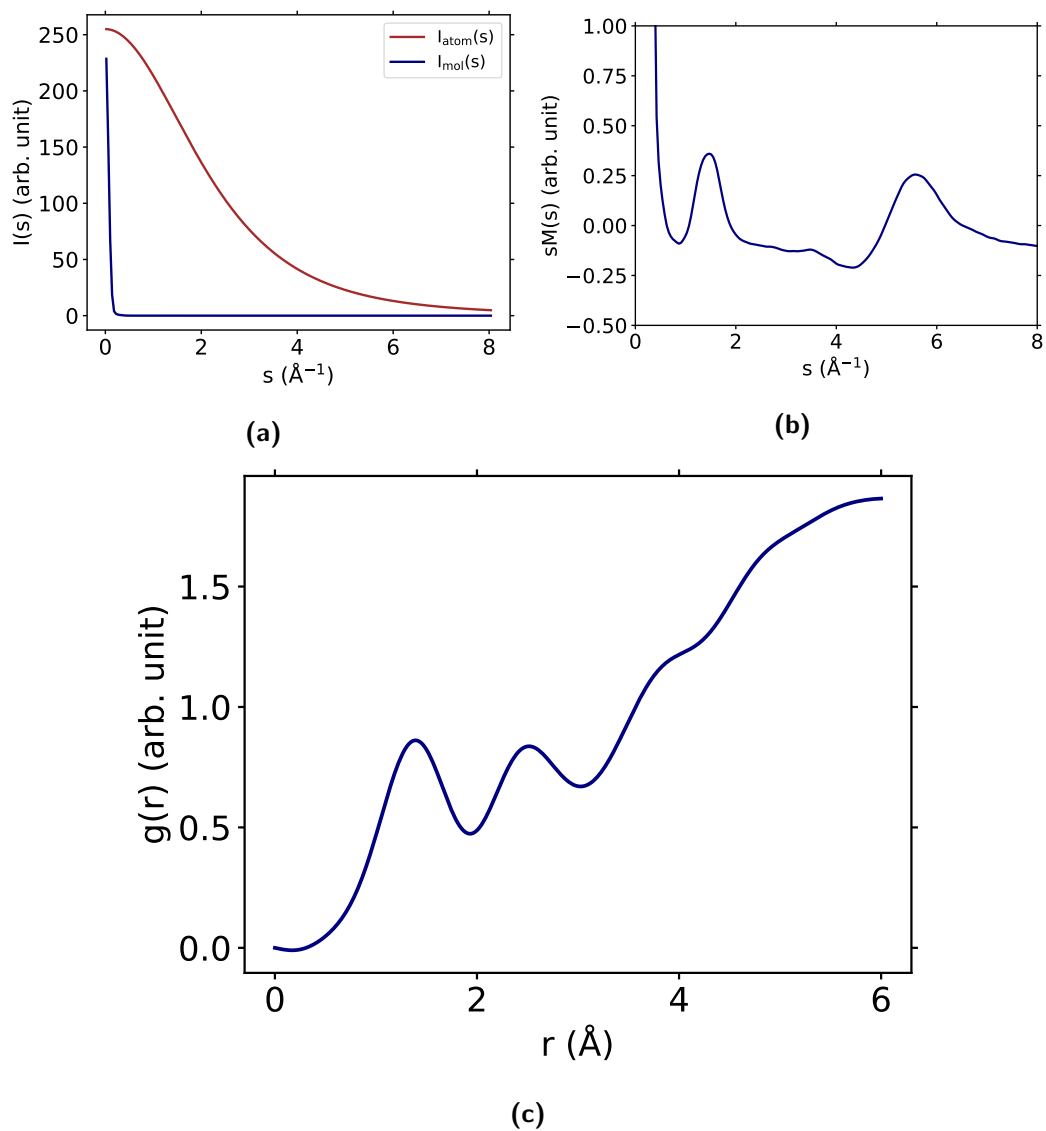
Figure 5.7: a) Azimuthal average of the total and atomic diffraction patterns, **b)** Modified scattering intensity calculated using Equation 4.11 vs. momentum transfer vector, **c)** Electron pair distribution function of liquid glycerol calculated using Equation 4.14.
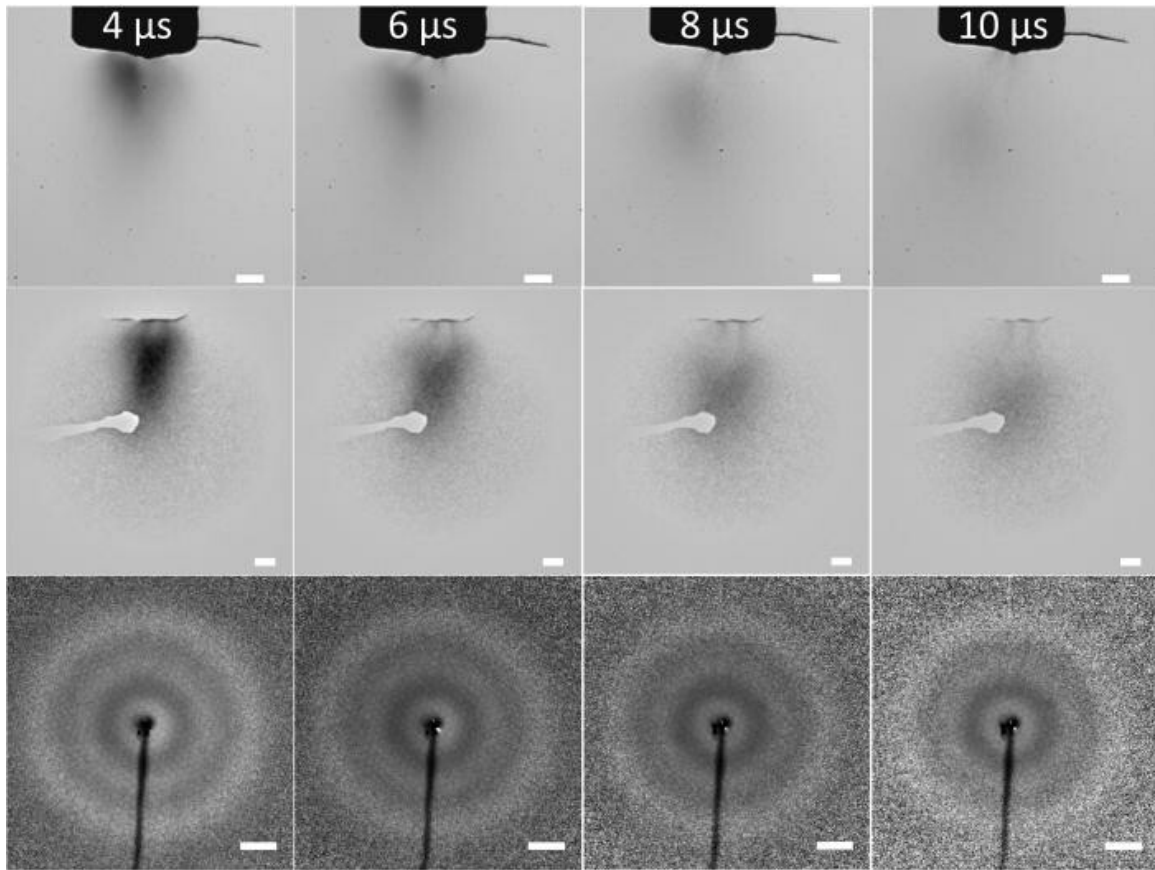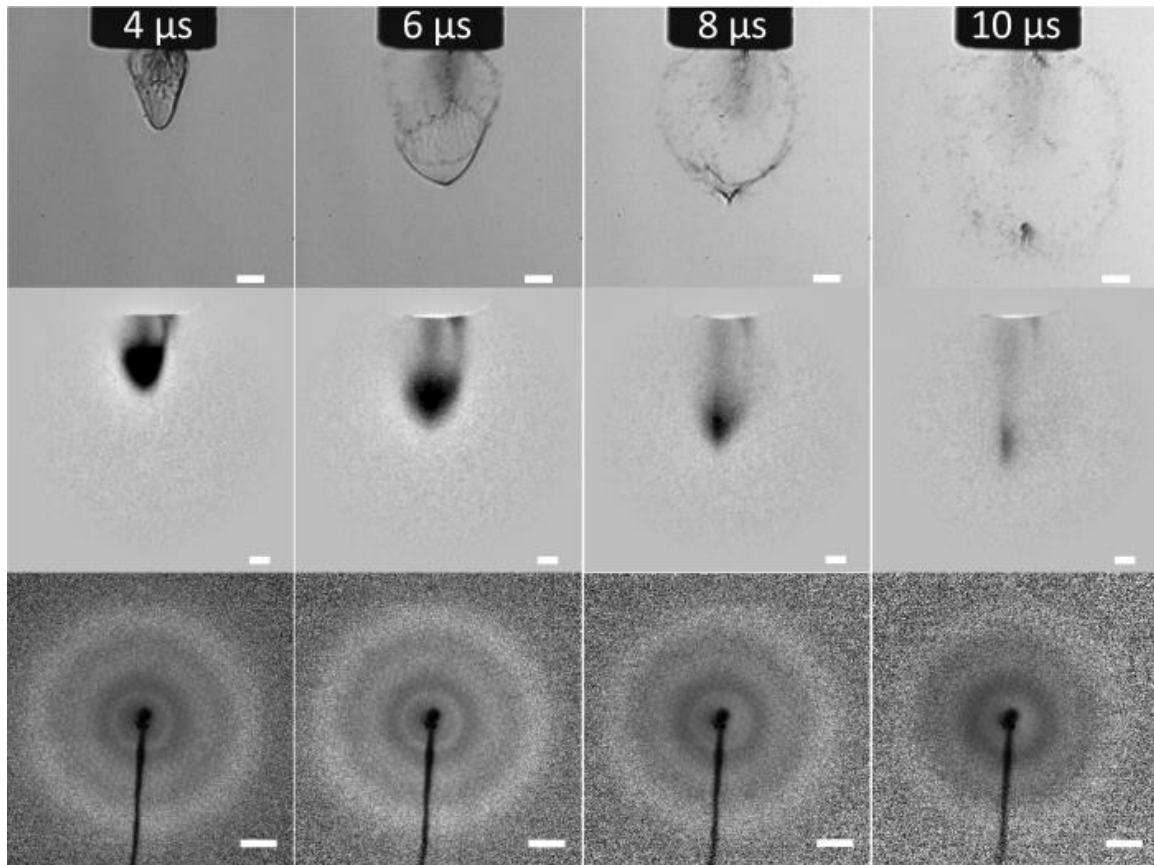
Figure 5.8: 1st row: Optical images (single shot) of the laser-driven glycerol plume at an ablation fluence of 220 mJ/cm^2. The white scale bar corresponds to 200 μm. **2nd row**: Electron real space images (averaged over 550 frames) of the laser-driven glycerol plume. The white scale bar corresponds to 200 μm. **3rd row**: Electron diffraction images ($I_{tot} \times s^2$, averaged over 2750 frames) of the laser-driven glycerol plume. Each row corresponds to a different delay as overlaid above. The white scale bar corresponds to 20 nm^{-1}. Reproduced from [20], with the permission of AIP Publishing.
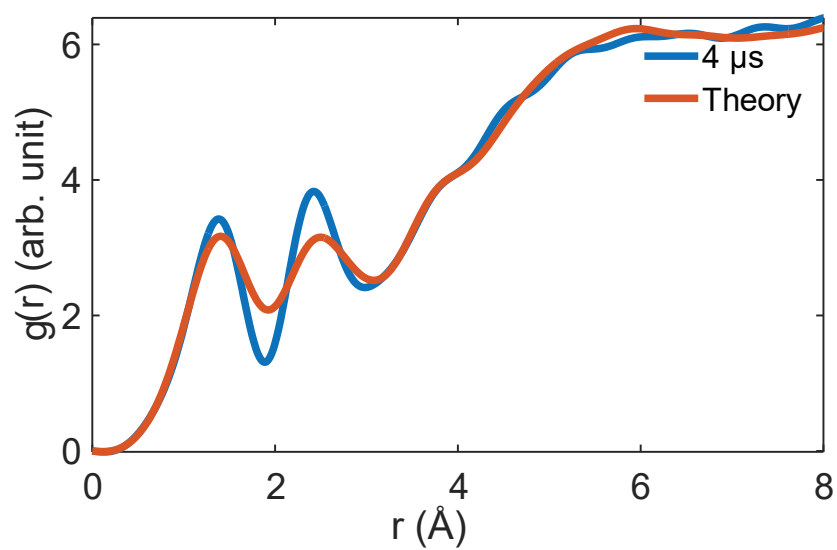
Figure 5.9: The electron pair distribution curve for plumes generated by a 220 mJ/cm^2 ablation fluence a delay of 4 μs, plotted against the theoretical electron pair distribution for liquid glycerol. Reproduced from [20], with the permission of AIP Publishing.

5.3. Remarks

By controlling the fluence of the ablation laser, we have successfully used laser-driven glycerol plumes as a sample source, allowing us to obtain structural data for both liquid and gaseous glycerol. To the best of our knowledge, our experiment represents the first instance of such an implementation.

In addition to its novelty, laser ablation of liquids has the advantage of overcoming the sample consumption problem associated with other sample delivery techniques used in X-ray diffraction methods. Based on previous thickness estimates (we assume a shell thickness of 5 μm for simplicity) and the base radius of the bubble shell (80 μm), a rough estimate for the primary sample ejection is 100 picoliters. Secondary recoil ejections can deplete a similar volume, giving us a depletion rate of 200 picoliters per shot. The repetition rate of our ablation laser is 1 kHz, but to avoid cumulative heating effects we have an ablation window of 100 ms, resulting in 100 shots per second. We need 2750 shots to produce an integrated diffraction image with a sufficient signal-to-noise ratio, resulting in a sample consumption of 550 nanolitres for a diffraction image. With more electrons in a pulse, the number of shots required to produce a usable diffraction pattern can be decreased, further reducing sample consumption. However, further testing with a variety of vacuum-stable liquids, not just glycerol, is important to broaden the scope of this method. Exploring the feasibility of incorporating embedded nanocrystals, microcrystals or other target molecules dissolved in the liquid is a potential avenue for future investigation. It should be noted, however, that this approach may be challenging and will require advances in several areas. Firstly, increased electron flux would be required to adequately probe the embedded particles or molecules. In addition, the development of sufficiently powerful analytical methods would be crucial to differentiate and analyze the contributions from both the solvent and the embedded entities.

Conclusion

The work presented in this dissertation occupies an interdisciplinary field of study involving a particular type of laser-matter interaction and the resulting novel dynamics. The results provide new insights into liquid elasticity in Newtonian fluids [21] and open the door to many more challenges to our understanding of a fundamental state of matter. Furthermore, it motivates us to explore the application of laser-driven ablation of liquids as a sample delivery source [20] or for structural studies of the liquid itself.

In the first part, I presented the in-vacuum laser ablation imaging system for liquids and the resulting measurements of the ablation of vacuum-stable liquids with varying external pressure and fluence conditions. Through our experiments, we demonstrate the occurrence of laser-induced front surface spallation in a small molecule liquid. This discovery subsequently reveals the presence of rubber-like elasticity in a Newtonian fluid. A deep dive into the phenomena of photomechanical spallation and subsequent analysis of bubble growth and bursting dynamics revealed a transient state for liquid glycerol exhibiting solid-like behaviour. In early studies of an ionic liquid that has different molecular interactions than glycerol, we observed a remnant of a laser-induced transient bubble. This observation suggests a broader potential for sub-nanosecond mid-infrared lasers to generate surface bubbles through photomechanical effects.

The process of photomechanical spallation has been studied by solving the one-dimensional thermoelastic wave equation in liquid glycerol. We have developed a practical and robust method for the thickness analysis of our axially symmetric shells, purely from the two-dimensional images. Using finite element modelling and the fracture rim velocity analysis, we showed that equilibrium surface tension and viscosity alone cannot explain the dynamics of the laser-induced bubble. We found a sys-

tem with flow dominated by elastic forces to an extent not previously observed in Newtonian fluids. These results extend recent studies pointing to the observation of non-Newtonian behaviour of known Newtonian fluids such as glycerol [58, 59, 140] below millimetre scale confinement. It is important to note that comparing our time domain observations with previous frequency domain dynamic mechanical analyses is not a straightforward task [141, 142]. In addition, our observations show a divergence in the high strain dynamics of the system, while the low and high frequency observations are made at minute strains[1]. We observe strain rate-driven elasticity in the liquid glycerol shell, with a linear dependence on the ablation fluence for the range studied. This strain rate-dependent increase in relaxation time has been observed in other shock loading experiments with glycerol [58], and may explain the metastable state [47].

An atomistic understanding of the origin of this elasticity beyond the molecular relaxation time τ_m is still lacking. While heterogeneity has been proposed as a microscopic explanation for the deviations from non-Newtonian behaviour observed in supercooled liquid glycerol [71], it is unknown whether such an explanation is correct in our case, as we operate in a different temperature range.

The second part of the thesis describes a proof-of-concept experiment that effectively uses electron diffraction to study laser-driven glycerol plumes. This experiment successfully demonstrates the use of a single sample delivery technique for electron diffraction, yet allows the study of both isolated gas and condensed liquid phases. By carefully adjusting the ablation laser fluence, we were able to generate two distinct phases (liquid shell and isolated gas) from liquid glycerol.

---

[1]In a recent article [143], Noirez et al. mention that the observed low-frequency elasticity is lost with increasing amplitude of applied strain, resulting in a viscous response at high strain.

Reflections and outlook

Reflecting on the four years of research described in this dissertation, I would like to point out some possible improvements to the experiments that should be considered in future investigations.

The imaging was initially set up to quantify the plume characteristics so that they could be used in an electron diffraction measurement. This resulted in the experimental design being more focused on helping us answer relatively simple questions such as the fluence-dependent spatial dimensions of the plume, the ablation threshold for phase explosion, etc. If I were to design the brightfield experiment again, I would ensure a more uniform illumination at the sample position. A homogeneous illumination makes the further image processing and analysis, which was discussed in Chapter 3, much easier.

We had the problem that the liquid droplet surface changes with time during the electron diffraction measurements. We got around this problem by discarding data with significant droplet surface variations. However, an improvement will be to create a stable liquid surface that does not change over time with a continuous delivery system. A local droplet temperature measurement setup is also advantageous to study post ablation heat dissipation, which we did not have in the experiments. These relatively less complex changes can be considered in the design of a liquid ablation imaging instrument.

Looking back, we have opened an area of research by creating perfect spallation conditions for studying liquid glycerol at a high strain rate. The knowledge gained from these studies is important for understanding the liquid state, and looking ahead, the possibilities for new insights are promising. The photomechanical spallation and subsequent analysis of the observations have shown that we need to further explore the field of laser-induced spallation in simple liquids. This method, coupled with

spectroscopic [48] and other more sophisticated imaging techniques, could become a powerful tool for studying the elastic properties of highly strained liquids in a time regime that is not well understood by existing methods. This could also be a way to study the molecular mechanics leading to elasticity. Scattering experiments (X-ray, neutron or electron) could also help us to understand the short, medium and long range correlations that occur in the metastable shell.

Ultrafast continuous imaging of laser-induced bubbles instead of the stroboscopic measurement we have implemented could be the next step, along with exploring the plume behavior in other vacuum-stable liquids ablated with tunable mid-IR lasers. The implementation of a time-resolved photoelastic measurement system with polarized light imaging [144] will also be helpful in understanding the strain distributions in the bubble.

A complete theoretical modelling of the laser-sample interaction is also of considerable interest. Especially as large-scale molecular dynamics simulations become accessible, a simulation approach could be valuable in understanding the inherent mechanisms that are difficult to resolve experimentally. Computational fluid dynamics simulations, which can take into account the elastic properties of fluids, could also be used in these cases. An experimental method to measure the thickness of the bubble in addition to our computational analysis is also of great interest, as this could help us to better understand the transport of material through the bubble.

Our research shows that the presence of a vacuum is essential for the formation of these elastic bubbles. While achieving a vacuum was feasible for glycerol due to its lower vapor pressure, it remained elusive for liquid water, which begins to boil at pressures below its vapor pressure of 32 mbar. The potential significance of elastic bubble formation in water is considerable, as these findings may also be relevant in biological settings. Consequently, future experiments could be conducted to further explore these possibilities.

Bibliography

1. Steen, W. M. "Laser material processing—an overview". *Journal of Optics A: Pure and Applied Optics* **5,** S3–S7 (2003).

2. Bakshi, V. *EUV lithography* (SPIE Press, 2009).

3. Azadgoli, B. & Baker, R. Y. "Laser applications in surgery". *Annals of translational medicine* **4** (2016).

4. Apitz, I. & Vogel, A. "Material ejection in nanosecond Er:YAG laser ablation of water, liver, and skin". *Appl. Phys. A* **81,** 329–338 (2005).

5. Günther, D., Horn, I. & Hattendorf, B. "Recent trends and developments in laser ablation-ICP-mass spectrometry". *Fresenius' Journal of Analytical Chemistry* **368,** 4–14 (2000).

6. Gahlmann, A., Park, S. T. & Zewail, A. H. "Structure of Isolated Biomolecules by Electron Diffraction-Laser Desorption: Uracil and Guanine". *Journal of the American Chemical Society* **131,** 2806–2808 (2009).

7. Gahlmann, A., Lee, I.-R. & Zewail, A. H. "Direct Structural Determination of Conformations of Photoswitchable Molecules by Laser Desorption-Electron Diffraction". *Angewandte Chemie International Edition* **49,** 6524–6527 (2010).

8. Lee, I.-R., Gahlmann, A. & Zewail, A. H. "Structural Dynamics of Free Amino Acids in Diffraction". *Angewandte Chemie* **124,** 103–106 (2012).

9. Martiel, I., Müller-Werkmeister, H. M. & Cohen, A. E. "Strategies for sample delivery for femtosecond crystallography". *Acta Crystallogr D Struct Biol* **75,** 160–177 (2019).

10. Miguet, J., Rouyer, F. & Rio, E. "The life of a surface bubble". *Molecules* **26,** 1317 (2021).

11. Prosperetti, A. "Bubbles". *Physics of fluids* **16,** 1852–1865 (2004).

12. Barcikowski, S., Plech, A., Suslick, K. S. & Vogel, A. "Materials synthesis in a bubble". *MRS Bulletin* **44,** 382–391 (2019).

13. Karimi, A. & Martin, J. "Cavitation erosion of materials". *International Metals Reviews* **31,** 1–26 (1986).

14. Wang, S.-P., Zhang, A.-M., Liu, Y.-L., Zhang, S. & Cui, P. "Bubble dynamics and its applications". *Journal of Hydrodynamics* **30,** 975–991 (2018).

15. Brennen, C. E. "Cavitation in medicine". *Interface focus* **5,** 20150022 (2015).

16. Dollet, B., Marmottant, P. & Garbin, V. "Bubble dynamics in soft and biological matter". *Annual Review of Fluid Mechanics* **51,** 331–355 (2019).

17. Wu, J. & Nyborg, W. L. "Ultrasound, cavitation bubbles and their interaction with cells". *Advanced drug delivery reviews* **60,** 1103–1116 (2008).

18. Fan, X., Little, M. W. & Murray, K. K. "Infrared laser wavelength dependence of particles ablated from glycerol". *Applied Surface Science* **255,** 1699–1704 (2008).

19. Leisner, A., Rohlfing, A., Röhling, U., Dreisewerd, K. & Hillenkamp, F. "Time-Resolved Imaging of the Plume Dynamics in Infrared Matrix-Assisted Laser Desorption/Ionization with a Glycerol Matrix". *The Journal of Physical Chemistry B* **109,** 11661–11666 (2005).

20. Huang, Z., Kayanattil, M., Hayes, S. A. & Miller, R. D. "Picosecond infrared laser driven sample delivery for simultaneous liquid-phase and gas-phase electron diffraction studies". *Structural Dynamics* **9,** 054301 (2022).

21. Kayanattil, M., Huang, Z., Gitaric, D. & Epp, S. W. *Rubber-like elasticity in laser-driven free surface flow of a Newtonian fluid.* In press, PNAS. 2023.

22. Vogel, A. & Venugopalan, V. "Mechanisms of Pulsed Laser Ablation of Biological Tissues". *Chemical Reviews* **103,** 577–644 (2003).

23. Paltauf, G. & Dyer, P. E. "Photomechanical Processes and Effects in Ablation". *Chemical Reviews* **103,** 487–518 (2003).

24. Shugaev, M. V. *et al.* in *Handbook of Laser Micro-and Nano-Engineering* 83–163 (Springer, 2021).

25. Guo, B., Sun, J., Lu, Y. & Jiang, L. "Ultrafast dynamics observation during femtosecond laser-material interaction". *International Journal of Extreme Manufacturing* **1,** 032004 (2019).

26. Chen, Z., Bogaerts, A. & Vertes, A. "Phase explosion in atmospheric pressure infrared laser ablation from water-rich targets". *Applied Physics Letters* **89,** 041503 (2006).

27. Chen, Z. & Vertes, A. "Early plume expansion in atmospheric pressure midinfrared laser ablation of water-rich targets". *Physical Review E* **77** (2008).

28. Franjic, K. & Miller, R. J. D. "Vibrationally excited ultrafast thermodynamic phase transitions at the water/air interface". *Physical Chemistry Chemical Physics* **12,** 5225 (2010).

29. Wu, B. "From supercritical hydrodynamic expansion to explosive phase change: Thermodynamic evolution of water during its interaction with high-intensity infrared nanosecond-pulsed laser". *Journal of Applied Physics* **105,** 053502 (2009).

30. Franjic, K., Cowan, M. L., Kraemer, D. & Miller, R. J. D. "Laser selective cutting of biological tissues by impulsive heat deposition through ultrafast vibrational excitations". *Opt. Express* **17,** 22937–22959 (2009).

31. Kanel, G. "Spall fracture: methodological aspects, mechanisms and governing factors". *International journal of fracture* **163,** 173–191 (2010).

32. Utkin, A. V., Sosikov, V. A., Bogach, A. A. & Fortov, V. E. *Tension of liquids by shock waves.* in *AIP Conference Proceedings* **706** (2004), 765–770.

33. Krivokorytov, M. S. *et al.* "Cavitation and spallation in liquid metal droplets produced by subpicosecond pulsed laser radiation". *Physical Review E* **95** (2017).

34. Lai, S. *et al.* "Submicron bubbles/voids formation in the subsurface region of soda-lime glass by single pulse fs laser-induced spallation". *Applied Surface Science* **502,** 144134 (2020).

35. Dingus, R. S. & Scammon, R. J. *Grüneisen-stress-induced ablation of biological tissue.* in *Laser-Tissue interaction ii* **1427** (1991), 45–54.

36. Stan, C. A. *et al.* "Negative pressures and spallation in water drops subjected to nanosecond shock waves". *The journal of physical chemistry letters* **7,** 2055–2062 (2016).

37. Paltauf, G. & Schmidt-Kloiber, H. "Microcavity dynamics during laser-induced spallation of liquids and gels". *Applied Physics A* **62,** 303–311 (1996).

38. Krishnan, J. M., Deshpande, A. P. & Kumar, P. S. *Rheology of complex fluids* (Springer, 2010).

39. Dexter, A. & Matheson, A. "The mechanical response of viscous liquids". *Advances in Molecular Relaxation Processes* **2,** 251–318 (1972).

40. Mark, J. E. "Rubber elasticity". *Journal of Chemical Education* **58.** Publisher: American Chemical Society, 898 (Nov. 1, 1981).

41. Ghabache, E., Antkowiak, A., Josserand, C. & Séon, T. "On the physics of fizziness: How bubble bursting controls droplets ejection". *Physics of Fluids* **26,** 121701 (Dec. 2014).

42. Veron, F. "Ocean Spray". *Annual Review of Fluid Mechanics* **47,** 507–538 (Jan. 3, 2015).

43. Taylor, G. I. "The dynamics of thin sheets of fluid. III. Disintegration of fluid sheets". *Proceedings of the Royal Society of London. Series A. Mathematical and Physical Sciences* **253,** 313–321 (1959).

44. Culick, F. E. "Comments on a ruptured soap film". *Journal of applied physics* **31,** 1128–1129 (1960).

45. Sabadini, E., Ungarato, R. F. S. & Miranda, P. B. "The Elasticity of Soap Bubbles Containing Wormlike Micelles". *Langmuir* **30,** 727–732 (2014).

46. Frenkel, J. *Kinetic Theory of Liquids eds. RH Fowler, P. Kapitza, NF Mott.* 1947.

47. Bannikova, I., Zubareva, A., Utkin, A., Uvarov, S. & Naimark, O. "Metastable states, relaxation mechanisms, and fracture of liquids under severe loading conditions". *Physical Mesomechanics* **20,** 399–406 (2017).

48. Pelton, M., Chakraborty, D., Malachosky, E., Guyot-Sionnest, P. & Sader, J. E. "Viscoelastic flows in simple liquids generated by vibrating nanostructures". *Physical Review Letters* **111,** 244502 (2013).

49. Bolmatov, D. "The Phonon Theory of Liquids and Biological Fluids: Developments and Applications". *The Journal of Physical Chemistry Letters* **13,** 7121–7129 (2022).

50. Joseph, D. D. "Historical perspectives on the elasticity of liquids". *Journal of Non-Newtonian Fluid Mechanics* **19,** 237–249 (1986).

51. Badmaev, B., Bal'zhinov, S., Damdinov, B. & Dembelova, T. "Low-frequency shear elasticity of liquids". *Acoustical physics* **56,** 640–643 (2010).

52. Noirez, L. & Baroni, P. "Revealing the solid-like nature of glycerol at ambient temperature". *Journal of Molecular Structure* **972,** 16–21 (2010).

53. Joseph, D. D., Riccius, O. & Arney, M. "Shear-wave speeds and elastic moduli for different liquids. Part 2. Experiments". *J. Fluid Mech.* **171,** 309 (1986).

54. Joseph, D. D., Narain, A. & Riccius, O. "Shear-wave speeds and elastic moduli for different liquids. Part 1. Theory". *J. Fluid Mech.* **171,** 289 (1986).

55. Riccius, O., Joseph, D. D. & Arney, M. "Shear-wave speeds and elastic moduli for different liquids Part 3. Experiments-update". *Rheol Acta* **26,** 96–99 (1987).

56. Derjaguin, B. V., Bazaron, U. B., Lamazhapova, K. D. & Tsidypov, B. D. "Shear elasticity of low-viscosity liquids at low frequencies". *Phys. Rev. A* **42,** 2255–2258 (4 1990).

57. Utkin, A., Sosikov, V. & Bogach, A. "Impulsive Tension of Hexane and Glycerol under Shock-Wave Loading". *Journal of applied mechanics and technical physics* **44,** 174–179 (2003).

58. Uvarov, S., Bannikova, I. & Naimark, O. *Pulse loading of glycerol by electric explosion of wire.* in *Journal of Physics: Conference Series* **653** (2015), 012034.

59. Kume, E., Zaccone, A. & Noirez, L. "Unexpected thermo-elastic effects in liquid glycerol by mechanical deformation". *Physics of Fluids* **33,** 072007 (2021).

60. White, R. M. & Geballe, T. H. *Long Range Order in Solids: Solid State Physics* (Elsevier, 2013).

61. Trachenko, K. & Brazhkin, V. "Collective modes and thermodynamics of the liquid state". *Reports on Progress in Physics* **79,** 016502 (2015).

62. Teschke, O., Mendez Soares, D. & Valente Filho, J. F. "Floating liquid bridge tensile behavior: Electric-field-induced Young's modulus measurements". en. *Applied Physics Letters* **103,** 251608 (2013).

63. Krutilin, A. *et al.* "Sampling of Tissues with Laser Ablation for Proteomics: Comparison of Picosecond Infrared Laser and Microsecond Infrared Laser". *J. Proteome Res.* **18,** 1451–1457 (2019).

64. *Water.* National Center for Biotechnology Information. PubChem Compound Database, Accessed : 2023-04-03.

65. XFEL. *Gaussian function — SCS documentation* .

66. Busse, F., Kruber, S., Robertson, W. D. & Miller, R. J. D. "Digital interference microscopy and density reconstruction of picosecond infrared laser desorption at the water-air interface". *Journal of Applied Physics* **124,** 094701 (2018).

67. Robergs, R. A. & Griffin, S. E. "Glycerol: Biochemistry, Pharmacokinetics and Clinical and Practical Applications". *Sports Medicine* **26,** 145–167 (1998).

68. Gull, M. & Pasek, M. A. "The Role of Glycerol and Its Derivatives in the Biochemistry of Living Organisms, and Their Prebiotic Origin and Significance in the Evolution of Life". *Catalysts* **11,** 86 (2021).

69. Cammenga, H. K., Schulze, F. W. & Theuerl, W. "Vapor pressure and evaporation coefficient of glycerol". *Journal of Chemical and Engineering Data* **22,** 131–134 (1977).

133

70. Mobius, M., Xia, T., Van Saarloos, W., Orrit, M. & Van Hecke, M. "Aging and solidification of supercooled glycerol". *The Journal of Physical Chemistry B* **114,** 7439–7444 (2010).

71. Zondervan, R. *et al.* "Soft glassy rheology of supercooled molecular liquids". *Proceedings of the National Academy of Sciences* **105,** 4993–4998 (2008).

72. "Introduction: Ionic Liquids". *Chemical Reviews* **117,** 6633–6635 (2017).

73. Ghandi, K. "A Review of Ionic Liquids, Their Limits and Applications". *GSC* **04,** 44–53 (2014).

74. Welton, T. "Ionic liquids: a brief history". *Biophys Rev* **10,** 691–706 (2018).

75. Armstrong, J. P. *et al.* "Vapourisation of ionic liquids". *Physical Chemistry Chemical Physics* **9,** 982 (2007).

76. Rovera, G. D., Siccardi, M., Römisch, S. & Abgrall, M. "Time delay measurements: estimation of the error budget". *Metrologia* **56,** 035004 (2019).

77. Xiong, R. *et al.* "Bubble Formation Modeling During Laser Direct Writing of Glycerol Solutions". *Journal of Micro and Nano-Manufacturing* **3** (2015).

78. Brown, M. S., Kattamis, N. T. & Arnold, C. B. "Time-resolved dynamics of laser-induced micro-jets from thin liquid films". en. *Microfluid Nanofluid* **11,** 199–207 (2011).

79. Brennen, C. E. *Cavitation and bubble dynamics. Oxford engineering science series* **44.** 282 pp. ISBN: 978-0-19-509409-1 (Oxford University Press, New York, 1995).

80. Serra, P. & Piqué, A. "Laser-Induced Forward Transfer: Fundamentals and Applications". *Advanced Materials Technologies* **4,** 1800099 (2019).

81. Jackson, S. N., Kim, J.-K., Laboy, J. L. & Murray, K. K. "Particle formation by infrared laser ablation of glycerol: implications for ion formation". *Rapid Communications in Mass Spectrometry* **20,** 1299–1304 (2006).

82. Weber, R. *et al.* "Heat accumulation during pulsed laser materials processing". *Optics express* **22,** 11312–11324 (2014).

83. Ahmadi, P., Chapoy, A. & Burgass, R. "An investigation on the thermophysical properties of glycerol". *The Journal of Chemical Thermodynamics* **178,** 106975 (2023).

84. Tan, H., Aziz, A. A. & Aroua, M. "Glycerol production and its applications as a raw material: A review". *Renewable and sustainable energy reviews* **27,** 118–127 (2013).

85. Kuksin, A. Y., Norman, G. E., Pisarev, V. V., Stegailov, V. V. & Yanilkin, A. V. "Theory and molecular dynamics modeling of spall fracture in liquids". *Phys. Rev. B* **82,** 174101 (2010).

86. Carlson, G. A. & Levine, H. S. "Dynamic tensile strength of glycerol". *Journal of Applied Physics* **46,** 1594–1601 (1975).

87. Dekel, E. *et al.* "Spallation model for the high strain rates range". *Journal of Applied Physics* **84,** 4851–4858 (1998).

88. Wu, C. & Zhigilei, L. V. "Microscopic mechanisms of laser spallation and ablation of metal targets from large-scale molecular dynamics simulations". *Applied Physics A* **114,** 11–32 (2014).

89. Carlson, G. A. & Henry, K. W. "Technique for studying dynamic tensile failure in liquids: application to glycerol". en. *Journal of Applied Physics* **44,** 2201–2206 (1973).

90. Carome, E., Clark, N. & Moeller, C. "Generation of acoustic signals in liquids by ruby laser-induced thermal stress transients". *Applied Physics Letters* **4,** 95–97 (1964).

91. Shori, R., Walston, A., Stafsudd, O., Fried, D. & Walsh, J. "Quantification and modeling of the dynamic changes in the absorption coefficient of water at = 2.94 m". *IEEE J. Select. Topics Quantum Electron.* **7,** 959–970 (2001).

92. Mausbach, P., Köster, A., Rutkai, G., Thol, M. & Vrabec, J. "Comparative study of the Grüneisen parameter for 28 pure fluids". *The Journal of chemical physics* **144,** 244505 (2016).

93. Franc, J.-P. in *Fluid dynamics of cavitation and cavitating turbopumps* 1–41 (Springer, 2007).

94. Gaudron, R., Warnez, M. T. & Johnsen, E. "Bubble dynamics in a viscoelastic medium with nonlinear elasticity". *Journal of Fluid Mechanics* **766,** 54–75. ISSN: 0022-1120, 1469-7645 (2015).

95. Isenberg, C. *The science of soap films and soap bubbles* (Dover Publications, 1981).

96. Santangelo, P. & Roland, C. "Temperature dependence of mechanical and dielectric relaxation in cis-1, 4-polyisoprene". *Macromolecules* **31,** 3715–3719 (1998).

97. Vannoni, M., Sordini, A., Gabrieli, R., Melozzi, M. & Molesini, G. "Measuring the thickness of soap bubbles with phase-shift interferometry". *Optics Express* **21,** 19657 (2013).

98. Mandracchia, B. *et al.* *Interferometric measurement of film thickness during bubble blowing.* in *Optical Methods for Inspection, Characterization, and Imaging of Biomaterials III* (eds Ferraro, P., Ritsch-Marte, M., Grilli, S. & Hitzenberger, C. K.) (SPIE, Munich, Germany, 2017), 63. ISBN: 978-1-5106-1111-5 978-1-5106-1112-2.

99. Tolbin, A. Y., Pushkarev, V. E. & Tomilova, L. G. "A mathematical analysis of deviations from linearity of Beer's law". *Chemical Physics Letters* **706,** 520–524 (2018).

100. Mamouei, M., Budidha, K., Baishya, N., Qassem, M. & Kyriacou, P. "An empirical investigation of deviations from the Beer–Lambert law in optical estimation of lactate". *Scientific Reports* **11,** 1–9 (2021).

101. Slie, W., Donfor Jr, A. & Litovitz, T. "Ultrasonic shear and longitudinal measurements in aqueous glycerol". *The Journal of Chemical Physics* **44,** 3712–3718 (1966).

102. Debrégeas, G., Martin, P. & Brochard-Wyart, F. "Viscous bursting of suspended films". *Physical review letters* **75,** 3886 (1995).

103. Debrégeas, G. d., De Gennes, P.-G. & Brochard-Wyart, F. "The life and death of" bare" viscous bubbles". *Science* **279,** 1704–1707 (1998).

104. Brenner, M. P. & Gueyffier, D. "On the bursting of viscous films". *Physics of Fluids* **11,** 737–739 (1999).

105. Tammaro, D. *et al.* "Elasticity in Bubble Rupture". *Langmuir* **34,** 5646–5654 (2018).

106. Tammaro, D. *et al.* "Flowering in bursting bubbles with viscoelastic interfaces". *Proceedings of the National Academy of Sciences* **118** (2021).

107. Evers, L., Shulepov, S. Y. & Frens, G. "Bursting dynamics of thin free liquid films from Newtonian and viscoelastic solutions". *Physical review letters* **79,** 4850 (1997).

108. Treloar, L. R. G. *The physics of rubber elasticity: by L.R.G. Treloar* 3rd ed (Clarendon Press ; Oxford University Press, Oxford : New York, 2005).

109. Joseph, D. D. *Fluid dynamics of viscoelastic liquids* (Springer New York, 1990).

110. Klieber, C. *et al.* "Mechanical spectra of glass-forming liquids. II. Gigahertz-frequency longitudinal and shear acoustic dynamics in glycerol and DC704 studied by time-domain Brillouin scattering". en. *The Journal of Chemical Physics* **138,** 12A544 (2013).

111. Piccirelli, R. & Litovitz, T. A. "Ultrasonic Shear and Compressional Relaxation in Liquid Glycerol". *The Journal of the Acoustical Society of America* **29,** 1009–1020 (1957).

136

112. Bund, A. & Schwitzgebel, G. "Viscoelastic Properties of Low-Viscosity Liquids Studied with Thickness-Shear Mode Resonators". *Analytical Chemistry* **70,** 2584–2588 (1998).

113. Inogamov, N., Zhakhovsky, V. & Migdal, K. "Laser-induced spalling of thin metal film from silica substrate followed by inflation of microbump". *Applied Physics A* **122,** 1–9 (2016).

114. Dudek, R. C. & Weber, P. M. "Ultrafast diffraction imaging of the electrocyclic ring-opening reaction of 1, 3-cyclohexadiene". *The Journal of Physical Chemistry A* **105,** 4167–4171 (2001).

115. Siwick, B. J., Dwyer, J. R., Jordan, R. E. & Miller, R. J. D. "An Atomic-Level View of Melting Using Femtosecond Electron Diffraction." *Science* **302,** 1382–1385 (5649 2003).

116. Nakamura, A., Shimojima, T., Nakano, M., Iwasa, Y. & Ishizaka, K. "Electron and lattice dynamics of transition metal thin films observed by ultrafast electron diffraction and transient optical measurements". *Structural Dynamics* **3,** 064501. ISSN: 2329-7778 (2016).

117. Brockway, L. "Electron diffraction by gas molecules". *Reviews of Modern Physics* **8,** 231–266 (3 1936).

118. Dwyer, J. R. *et al.* "Femtosecond electron diffraction: 'making the molecular movie'". *Philosophical Transactions of the Royal Society A: Mathematical, Physical and Engineering Sciences* **364,** 741–778 (2006).

119. Zewail, A. H. "4D Ultrafast electron diffraction, crystallography, and microscopy". *Annual Review of Physical Chemistry* **57,** 65–103 (2006).

120. Williamson, J. C., Cao, J., Ihee, H., Frey, H. & Zewail, A. H. "Clocking Transient Chemical Changes by Ultrafast Electron Diffraction." *Nature* **386,** 159–162 (6621 1997).

121. Wolf, T. J. *et al.* "The photochemical ring-opening of 1, 3-cyclohexadiene imaged by ultrafast electron diffraction". *Nature chemistry* **11,** 504–509 (2019).

122. Charles Williamson, J. & Zewail, A. H. "Ultrafast electron diffraction. Velocity mismatch and temporal resolution in crossed-beam experiments". *Chemical Physics Letters* **209,** 10–16 (1993).

123. Zandi, O. *Design and construction of a high-current femtosecond gas-phase electron diffraction setup.* PhD thesis (The University of Nebraska-Lincoln, 2017).

124. Weathersby, S. *et al.* "Mega-electron-volt ultrafast electron diffraction at SLAC National Accelerator Laboratory". *Review of Scientific Instruments* **86,** 073702 (2015).

125. Koralek, J. D. *et al.* "Generation and characterization of ultrathin free-flowing liquid sheets". *Nature Communications* **9** (2018).

126. De Kock, M. B., Azim, S., Kassier, G. H. & Miller, R. J. D. "Determining the radial distribution function of water using electron scattering: A key to solution phase chemistry". *The Journal of Chemical Physics* **153,** 194504 (2020).

127. Nunes, J. P. F. *et al.* "Liquid-phase mega-electron-volt ultrafast electron diffraction". *Structural Dynamics* **7,** 024301 (2020).

128. Ledbetter, K. *et al.* "Photodissociation of aqueous I 3 - observed with liquid-phase ultrafast mega-electron-volt electron diffraction". *Structural Dynamics* **7,** 064901 (2020).

129. Yang, J. *et al.* "Structure retrieval in liquid-phase electron scattering". *Phys. Chem. Chem. Phys.* **23,** 1308–1316 (2021).

130. Andreas, G. *Ultrafast electron diffraction: pulsed laser desorption enables time-resolved structural determination of thermally labile chromophores.* PhD thesis (California Institute of technology, Pasadena, California, 2011).

131. Kirkland, E. J. *Advanced Computing in Electron Microscopy* (Springer US, Boston, MA, 1998).

132. Davisson, C. & Kunsman, C. H. "The Scattering of low Speed Electrons by Platinum and Magnesium". *Phys. Rev.* **22,** 242–258 (3 1923).

133. Brockway, L. O. "Electron Diffraction by Gas Molecules". *Reviews of Modern Physics* **8,** 231–266 (1936).

134. Lobato, I. & Van Dyck, D. "An accurate parameterization for scattering factors, electron densities and electrostatic potentials for neutral atoms that obey all physical constraints". *Acta Crystallographica Section A Foundations and Advances* **70,** 636–649 (2014).

135. Gorelik, T. E. *Electron Pair-Distribution Function (ePDF) Analysis.*

136. Vishnevskiy, Y. V., Blomeyer, S. & Reuter, C. G. "Gas standards in gas electron diffraction: accurate molecular structures of CO2 and CCl4". *Structural Chemistry* **31,** 667–677 (2020).

137. Towey, J., Soper, A. & Dougan, L. "The structure of glycerol in the liquid state: a neutron diffraction study". *Physical Chemistry Chemical Physics* **13,** 9397–9406 (2011).

138. Oveisi, E. *Imaging modes in TEM*. EPFL, 2019.

139. Williamson, J. C. *Ultrafast gas-phase electron diffraction* (California Institute of Technology, 1998).

140. Zaccone, A. & Noirez, L. "Universal G L–3 law for the low-frequency shear modulus of confined liquids". *The Journal of Physical Chemistry Letters* **12,** 650–657 (2021).

141. Bartolini, L., Iannuzzi, D. & Mattei, G. "Comparison of frequency and strain-rate domain mechanical characterization". *Scientific Reports* **8,** 13697 (2018).

142. Zeltmann, S. E., Bharath Kumar, B., Doddamani, M. & Gupta, N. "Prediction of strain rate sensitivity of high density polyethylene using integral transform of dynamic mechanical analysis data". *Polymer* **101,** 1–6 (2016).

143. Noirez, L. in *Probing Submillimeter Dynamics to Access Static Shear Elasticity from Polymer Melts to Molecular Fluids* 1–23 (Springer Berlin Heidelberg, 2020).

144. Nguyen, T. T. P., Tanabe, R. & Ito, Y. "Laser-induced shock process in under-liquid regime studied by time-resolved photoelasticity imaging technique". *Applied Physics Letters* **102,** 124103 (2013).

145. Meyers, M. A. & Chawla, K. K. *Mechanical behavior of materials* (Cambridge university press, 2008).

146. Derjaguin, B., Bazaron, U., Zandanova, K. & Budaev, O. "The complex shear modulus of polymeric and small-molecule liquids". *Polymer* **30,** 97–103 (1989).

147. Noirez, L. & Baroni, P. "Identification of a low-frequency elastic behaviour in liquid water". *Journal of Physics: Condensed Matter* **24,** 372101 (2012).

148. Kume, E., Baroni, P. & Noirez, L. "Strain-induced violation of temperature uniformity in mesoscale liquids". *Sci Rep* **10,** 13340 (2020).

149. Zaccone, A. & Trachenko, K. "Explaining the low-frequency shear elasticity of confined liquids". *Proc Natl Acad Sci USA* **117,** 19653–19655 (2020).

150. Ohno, K.-i., Tachikawa, K. & Manz, A. "Microfluidics: applications for analytical purposes in chemistry and biochemistry". *Electrophoresis* **29,** 4443–4453 (2008).

151. Jung, G. & Petersen, C. F. "Confinement-induced demixing and crystallization". *Phys. Rev. Research* **2,** 033207 (3 2020).

152. Tschoegl, N. W., Knauss, W. G. & Emri, I. "Poisson's ratio in linear viscoelasticity–a critical review". *Mechanics of Time-Dependent Materials* **6,** 3–51 (2002).

153. Egorov, A. V., Lyubartsev, A. P. & Laaksonen, A. "Molecular Dynamics Simulation Study of Glycerol–Water Liquid Mixtures". *The Journal of Physical Chemistry B* **115,** 14572–14581 (2011).

154. McKinley, G. H. "Dimensionless groups for understanding free surface flows of complex fluids" (2005).

155. Avila, S. R. G. & Ohl, C.-D. "Fragmentation of acoustically levitating droplets by laser-induced cavitation bubbles". *Journal of Fluid Mechanics* **805,** 551–576 (2016).

156. Salkin, L., Schmit, A., Panizza, P. & Courbin, L. "Generating soap bubbles by blowing on soap films". *Physical review letters* **116,** 077801 (2016).

157. Cohen, C. *et al.* "On the shape of giant soap bubbles". *Proceedings of the National Academy of Sciences* **114,** 2515–2519 (2017).

158. Grady, D. "The spall strength of condensed matter". *Journal of the Mechanics and Physics of Solids* **36,** 353–384 (1988).

159. Tovbin, Y. K. "Surface Tension: Mechanics, Thermodynamics, and Relaxation Times". *Russ. J. Phys. Chem.* **92,** 1045–1059 (2018).

160. Kaufman, S. & Whalen, T. "The surface tension of liquid gold, liquid tin, and liquid gold-tin binary solutions". *Acta metallurgica* **13,** 797–805 (1965).

161. Liu, X. M., He, J., Lu, J. & Ni, X. W. "Effect of surface tension on a liquid-jet produced by the collapse of a laser-induced bubble against a rigid boundary". *Optics & Laser Technology* **41,** 21–24 (2009).

162. Rice, O. K. "The Effect of Pressure on Surface Tension". *The Journal of Chemical Physics* **15,** 333–335 (1947).

163. Hills, G. & Høiland, H. "Pressure dependence of the surface tension of mercury". *Journal of Colloid and Interface Science* **99,** 463–467 (1984).

164. Palmer, S. J. "The effect of temperature on surface tension". *Physics Education* **11,** 119–120 (1976).

Appendix

Substances used during the project

List of the hazardous substances used in the work. They are marked as per Global Harmonised System (GHS) within the European Union (EU). No carcinogenic, mutagenic and toxic chemicals with the GHS categories 1A and 1B were used in this work.

Chemicals	GHS Symbols	Hazard statements	Precautionary statements
Glycerol (1,2,3-Propanetriol)		H315, H319, H335	P280, P302+ P352, P304 + P340, P305 + P351 + P338
Ionic liquid (Tris(2-hydroxyethyl)methylammonium methylsulfate)	--	--	--
Titanium(IV) Oxide		H314, H318	P260, P280, P303 + P361 + P353, P304 + P340, P305 + P351 + P338, P310
Vitamin B12	--	--	--
Acetone		H225, H319, H336	P210, P305 + P351 + P338, P403 + P233
Ethanol		H225, H319	P210, P233, P305 + P351 + P338 + P310, P305 + P351 + P338 + P310
2-Propanol		H225, H319, H336	P210, P233, P305 + P351 + P338

Figure A.1: All the chemicals used during the duration of the PhD with H- and P-data

Viscoelasticity

Building on the discussion in the Introduction, Figure B.1 provides a more detailed understanding of the behavior of both Newtonian and non-Newtonian fluids. Non-Newtonian fluids can be broadly classified as shear thinning (pseudoplastic) and shear thickening (dilatant)[1]. A well-known example of a pseudoplastic material is latex paint, which becomes less viscous as brush strokes become more vigorous (increased stress). On the other hand, a mixture of water and cornstarch (oobleck) is an example of a dilatant material, which behaves more viscous as the stress increases.

As discussed in the introduction, viscoelasticity is measured using dynamic mechanical analysis (DMA) methods, as shown in the simplified scheme in Figure B.2. We have seen that the shear modulus typically measured is frequency dependent. A complex shear modulus $G^*(\omega)$ can be defined as follows [145],

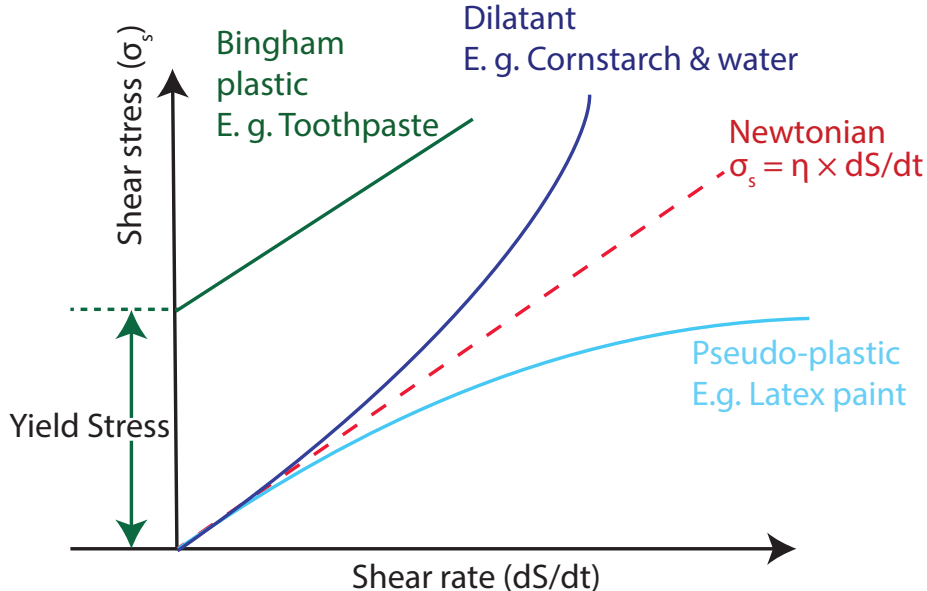$$G^*(\omega) = G'(\omega) + iG''(\omega) \tag{B.1}$$

with the two components , storage modulus ($G'(\omega)$) and loss modulus ($G''(\omega)$). The storage modulus can be expressed using the phase lag as follows,

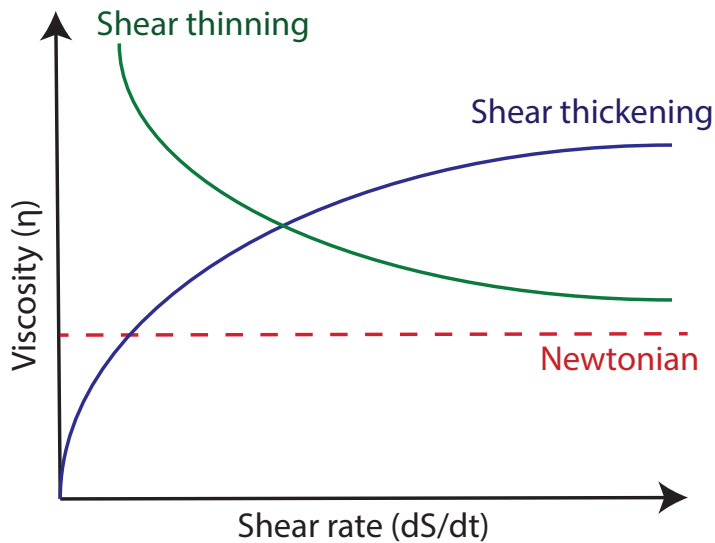$$G'(\omega) = \frac{\sigma_0}{\epsilon_0} cos(\delta) \tag{B.2}$$

Similarly, the loss modulus ($G''(\omega)$) can be written as,

$$G''(\omega) = \frac{\sigma_0}{\epsilon_0} sin(\delta) \tag{B.3}$$

---

[1]Other sub-classifications capture different behaviors, such as Bingham plastic and viscoplastic. A detailed look at these can be found in reference [38]

(a) Shear rate vs shear stress plot depicting the behavior of fluids.

(b) Shear rate vs viscosity plot depicting the behavior of fluids.

Figure B.1: Newtonian and non-Newtonian behavior of fluids.

The storage modulus represents the elastic portion, which is a measure of stored energy, and the loss modulus represents the viscous portion, which results in energy dissipation during flow. Rheometric measurements measure these two components at different frequencies and determine the viscoelastic properties of the materials.
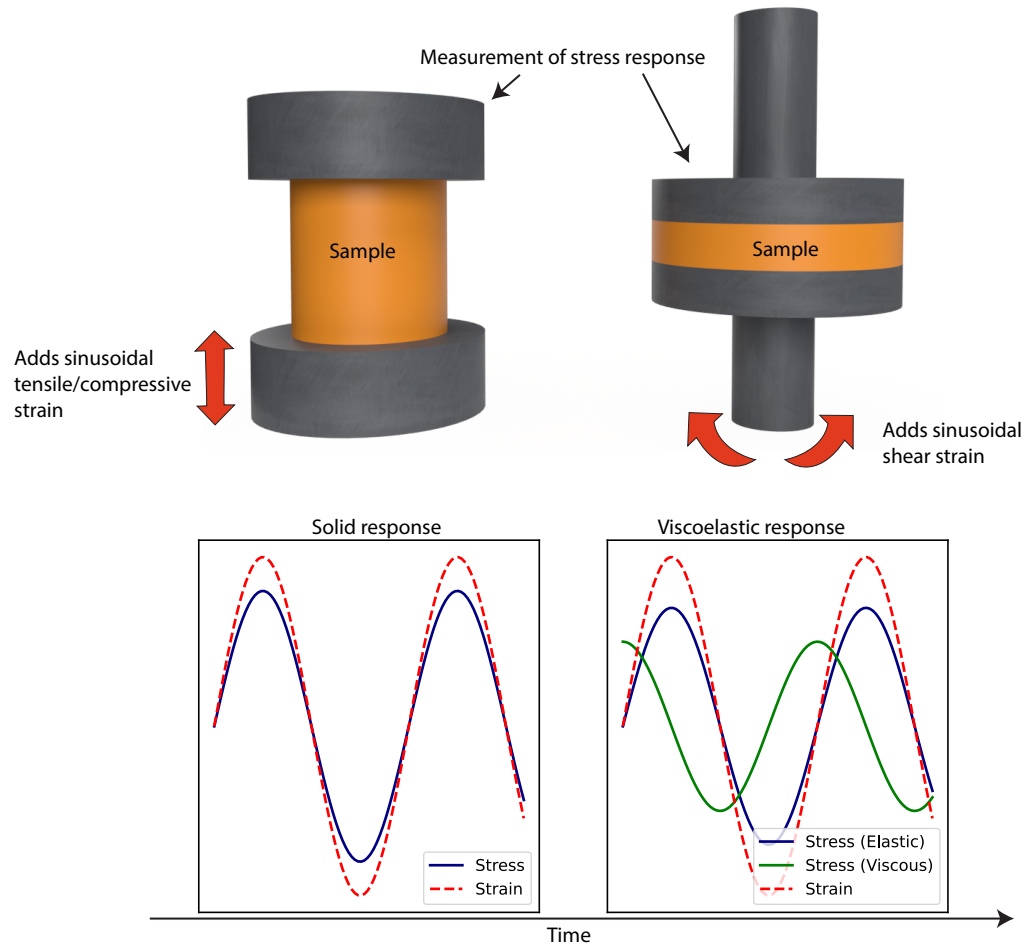

Figure B.2: Simplified schematics of rheometers used for measurement of elastic properties associated with materials and representative responses from such measurements. The unsentangled viscous and elastic response curves are for illustrative purposes only.

B.1. Low-frequency elasticity in liquids

Low-frequency elasticity is a discipline that investigates the existence of elasticity in fluids beyond their expected self-diffusion time τ_m. After the early work of D.D. Joseph [53, 54] and Derjaguin et al. [56, 146], There have been some notable recent works in the area of low-frequency elasticity in Newtonian fluids, led by Prof. Laurence Noirez, attempting to explain the unexpected behavior of Newtonian fluids in confinement [52, 59, 147, 148].

There has been renewed interest in understanding the theoretical basis of low-frequency elasticity in the years since it was first observed. In 2020, Zaccone and Trachenko published a study [149] proposing an explanation for these low-frequency shear elasticities in terms of a scaling law of $G' \approx L^{-3}$. The following year, Zaccone and Noirez further claimed that this law could potentially be universal [140]. Although we lack complete understanding of the origins of elasticity in our system and the connection to the field of low-frequency elasticity, it is crucial to have knowledge of these unusual behaviors of simple NFs. These studies highlight some of the obvious gaps in our understanding of fluids. With the increasing use of microfluidics as lab-on-chip instruments [150], and the understanding of novel phase transition processes [151], we need a better understanding of fluid behavior at time scales, confinement conditions, and strain rates not previously studied.

Appendix C

Modeling the bubble tip motion

Figures and parts of this appendix are adapted from the article [21].

To model the bubble shell, we used the finite element solver *COMSOL Multiphysics 6.0*™, assuming a linear elastic material with:

- Young's modulus, $E \in [0.1 \text{ MPa}, 1 \text{ GPa}]$

- Poisson's ratio $\nu = 0.499$

- Density $\rho = 1.26 \text{ g/cm}^3$

- Temperature $T = 293 \text{ K}$

While Poisson's ratio is included as an input parameter in the modeling, it should be noted that, strictly speaking, Poisson's ratio is a dynamic quantity [152] and can behave non-linearly under transient loading conditions. However, a value of 0.499 is considered reasonable for liquids, since their Poisson's ratio is expected to be close to 0.5. Remarkably, the data did not require more advanced schemes, but rather a constant Poisson's ratio.

A two-dimensional axially symmetric model was used to solve the problem, as shown in figure C.1, and the stability of the simulation was improved by interpolating the spallation layer with hexagonal structures. The bulk of the fluid outside the spallation layer was fixed in space. The modeled layer had a thickness of 10 μm and a diameter

of 160 μm for a laser fluence of 242 ± 11 mJ/cm^2 (160 μm for 206 ± 9 mJ/cm^2 and 130 μm for 174 ± 8 mJ/cm^2). The initial velocity profile of different segments of the layer was obtained from the experimental early plume images, as shown in table C.1 and figure 2.13a at $t = 0$.

The thickness of the elastic film is not a critical factor in the simulation because the local experimental velocities of the shell are used as initial conditions, and increasing the thickness does not change the ratio of kinetic to elastic energy. This ratio is determined by the mass and volume, which are assumed to be constant due to the incompressibility of the fluid.

We've observed that when the value of E, the Young's modulus, is increased beyond 1 GPa, the mass at the tip of the membrane undergoes harmonic motion. We've also noticed, however, that decreasing the value of E causes the membrane thickness to decrease, which can cause the simulation to fail as the thickness approaches zero. In our simulations of a linear elastic membrane, we've found that the modulus values that match the experimental results result in simulation times of about 250 ns, which is much shorter than the multi-microsecond dynamics observed experimentally. Fortunately, we've found that accurate results can still be obtained by fitting a sinusoidal function to a small fraction of the observed codomain values.

To study the dynamics of the plume after a laser pulse, we ran simulations for 10-15 values of E, ranging from 0.1 MPa to 0.2 GPa, for each of the three laser fluences. The simulations were run for 250 ns, and the position-time values of the bubble tip were calculated as $h_{sim}(t)$. We then used a function of the form,

$$h_{sim}(t) = h_{max} \times sin(\frac{2\pi}{T} \times t) \tag{C.1}$$

with fit parameters h_{max} and T to fit these values. The resulting E vs. $T_{sim}/2$ values are plotted in Figure C.2 for the three ablation intensities used. Next, the fit parameters T_{exp} and h_{exp} were obtained from the experimental data. The function $\frac{T_{sim}}{2}(E) = a \times (E - b)^c$ used to fit the simulated data points was a generalized version of the functional relationship between period time and spring constant D of a simple spring pendulum, where T is proportional to $D^{-0.5}$. However, this function is only a phenomenological approach and fits the data well for this specific purpose.

The derived dynamic Young's modulus values $E_{sim}(\frac{T_{exp}}{2})$ of 0.15 ± 0.01, 0.19 ± 0.02, and 0.21 ± 0.01 MPa for the three laser intensities from low to high are found as shown in Figure C.2. Since they can be expected to be dominated by a systematic error rather than relatively small statistical errors, the true error bars of these values

are difficult to evaluate.

Segment	Velocity (m/s) at 242 ± 11 mJ/cm^2	206 ± 9 mJ/cm^2	174 ± 8 mJ/cm^2
1	288.4	263.5	200.6
2	282.9	258.5	192.7
3	260.5	238.0	178.9
4	223.9	204.6	157.2
5	177.5	162.2	127.1
6	126.4	115.5	90.8
7	75.2	68.8	53.4
8	28.1	25.7	22.3
9	6.9	6.3	5.0

Table C.1: Initial velocities of the shell segments for simulation according to figureC.1 for the three different laser peak fluences.
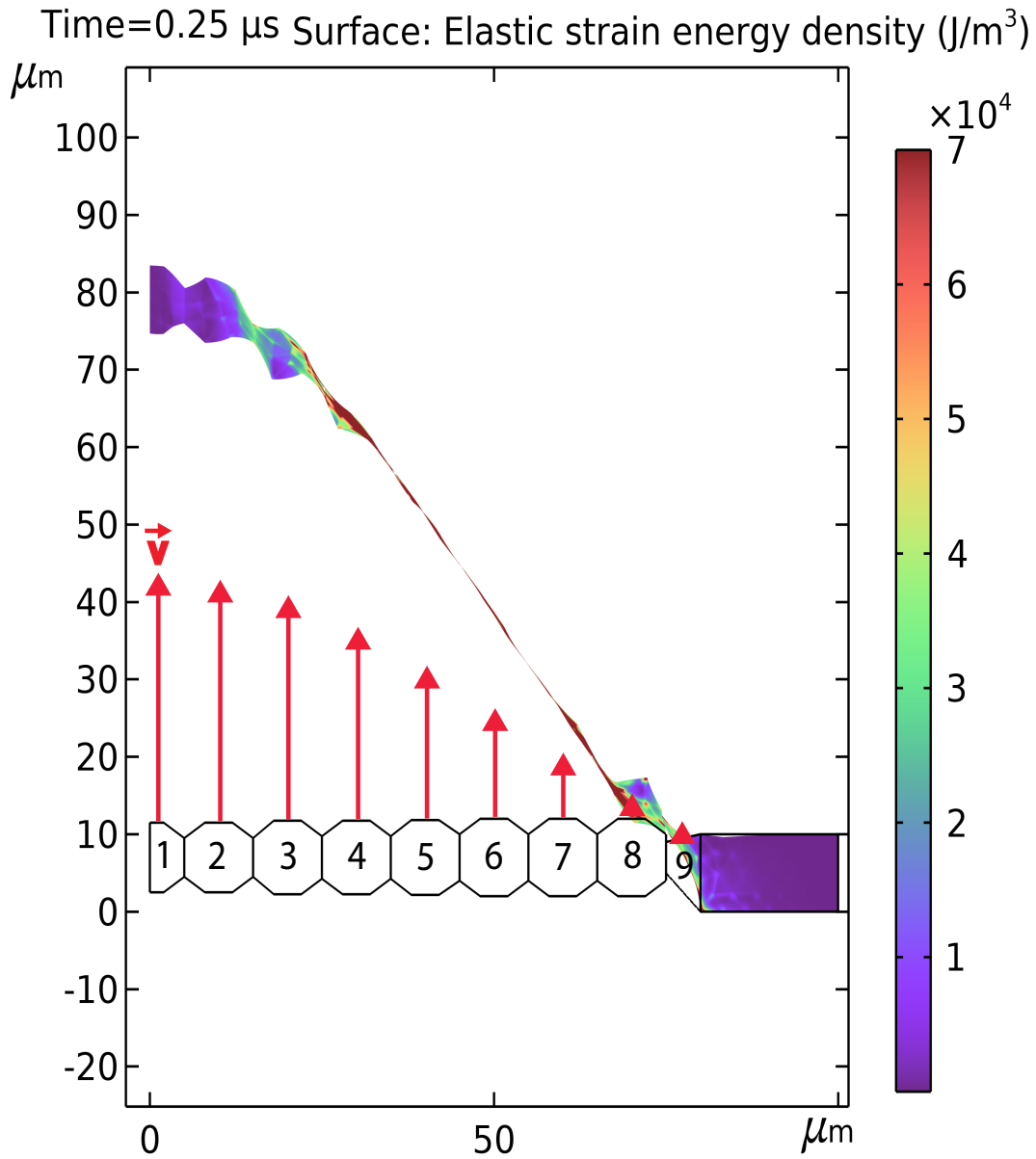
Figure C.1: The horizontal axis represents the radius, while the vertical axis represents the z-axis. The membrane is composed of several sections, the inner eight of which have a hexagonal shape. The initial velocities of the different sections are indicated by red arrows. The membrane is visible at two different times: at the beginning, denoted by $t = 0$, and 250 nanoseconds later. At the later time point, the colored sections of the membrane show the elastic strain energy, which becomes very high as the membrane becomes extremely thin.

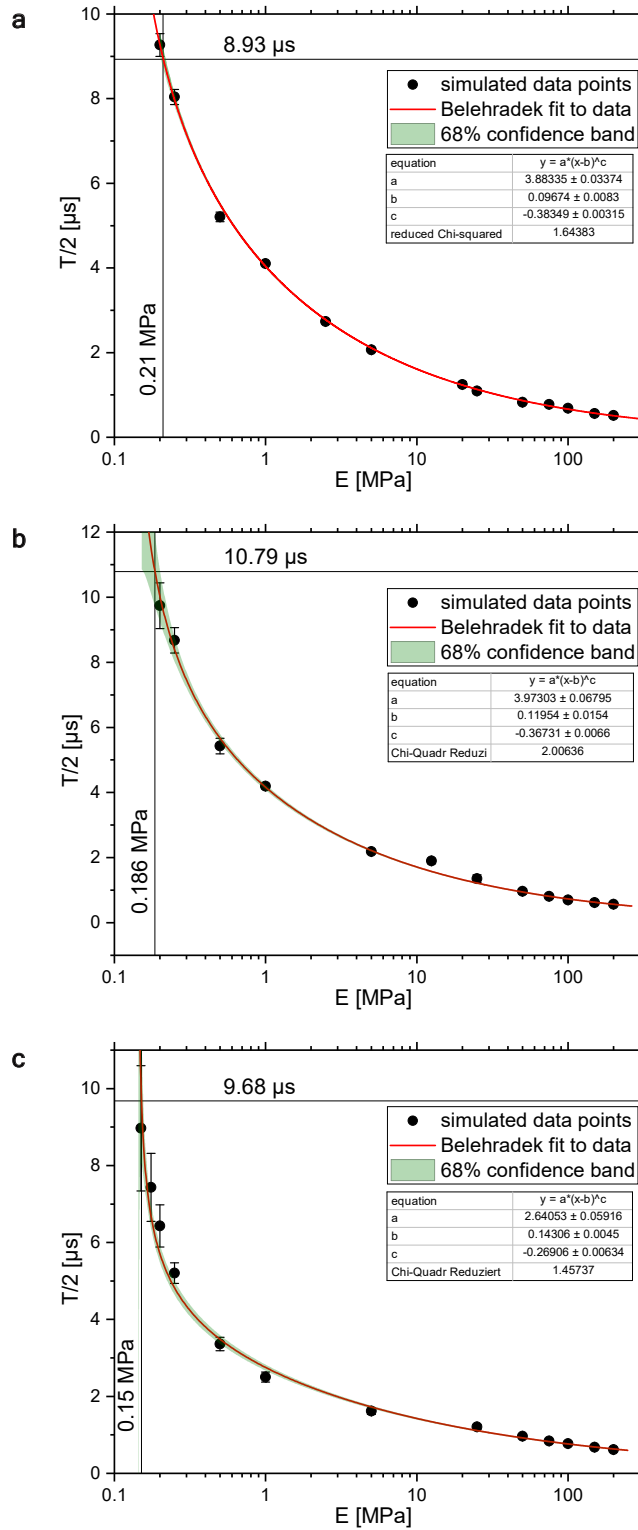**Figure C.2:** E vs. $\frac{T_{sim}}{2}$. **a**) peak fluence of 242 ± 11 mJ/cm², **b**) peak fluence of 206 ± 9 mJ/cm², **c**) peak fluence of 174 ± 8 mJ/cm². Young's modulus (vertical line) is found from the experimental period times (horizontal line).

Appendix D

Molecular dynamics simulations for liquid structure

To understand the diffraction pattern produced after a laser ablation electron diffraction experiment and to come up with explanations for the observations, we need the structural information of the isolated and liquid phase structure for glycerol. Once we have a geometry file with atomic position values, experimental and theoretical results can be compared. The ground energy structure of isolated glycerol is available in the Computational Chemistry Comparison and Benchmark Data Base from the National Institute of Standards and Technology[1]. Optimized geometry can be chosen based on different approximations in the calculation methods; however, the variation in the structure is small for most DFT calculations. These can be used to calculate the diffraction pattern and the electron pair distribution function, depending on the use case.

On the other hand, such a process is not feasible for liquid phase geometry. The easiest way to solve this problem is to generate the geometry file after optimizing the energy for several glycerol molecules satisfying the temperature, pressure, and density conditions. This can be done using standard molecular dynamics software such as GROMACS[2].

In this appendix I'll give a general overview of how we used GROMACS to create the geometry file. Before we start the simulation, there are two main requirements:

---

[1]https://cccbdb.nist.gov/
[2]https://www.gromacs.org/

finding a suitable geometry file for a single molecule and defining the force field specifications.

Our initial geometry file was the same as the one we used for isolated glycerol. With some syntax modifications to make it an acceptable input for the GROMACS software. We then needed to define the topology of the molecule, including the atomic charges on each atom. This data was taken from [153]. After defining the atomic charges and topology, we defined a box of 398 molecules that satisfy the density conditions for liquid glycerol (1260 kg/m^3) within a margin of error of less than 10%. This box creation can also be fine-tuned at the user's discretion[3]. After the box has been created as shown in the figure D.1, the energy of the system can be minimized based on the input parameters specified in a '.mpd' (molecular dynamics parameters) file. More information about the inputs that go into the parameter file can be found here[4].
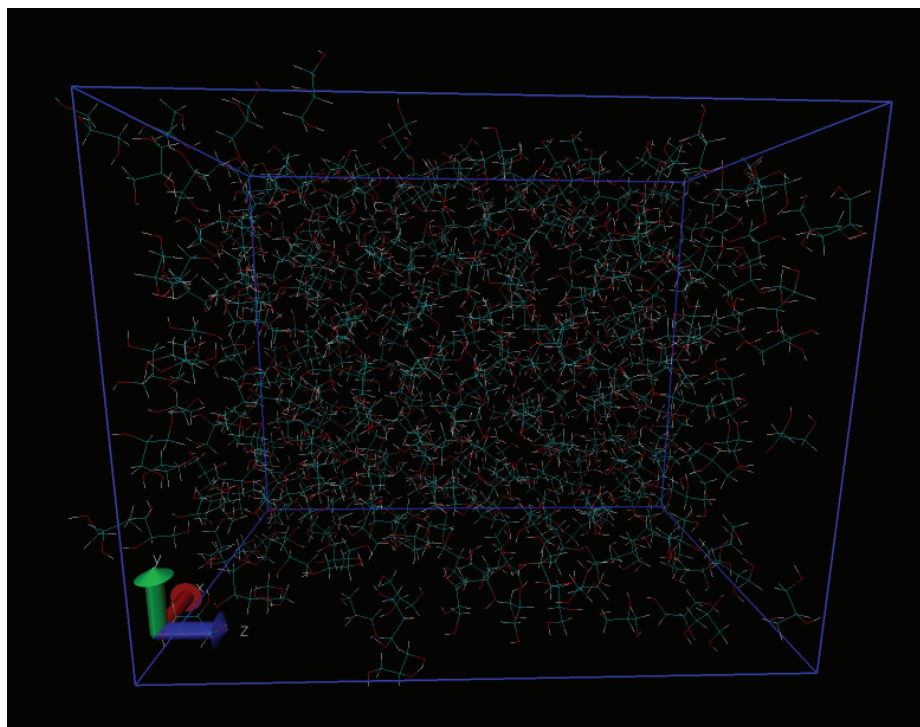

Figure D.1: A box of 398 glycerol molecules with optimized geometry as per the used discretion.

---

[3]https://manual.gromacs.org/documentation/current/onlinehelp/gmx-insert-molecules.html

[4]https://manual.gromacs.org/documentation/current/user-guide/mdp-options.html

Dimensionless groups and bubble dynamics

Systematically understanding free surface deformations in fluids as we have is no easy task. Generally, there are multiple forces contributing to the dynamics. The tools which can help us understand the influence of different forces involved in such a situation are that of dimensional analysis, which is thoroughly explained here [154].

Constants of importance for room temperature liquid glycerol

- Viscosity $(\eta) = 1.487$ P.s $= 1487$ mPa.s $= 1487$ (mN/m^2).s

- Surface tension $(\sigma_{ST}) = 63.4$ mN/m

- Density $(\rho) = 1260$ kg/m^3

For ablation fluence of 242 ± 11 mJ/cm^2

- Vertical velocity of the bubble, $V \approx 270 \pm 18$ m/s

- Horizontal diameter of the bubble, $l \approx 160$ μm

We will look into the Reynolds number and capillary number for our case. Reynolds

number helps us assess the system's relationship between inertial and viscous forces. Re can be deduced as,

$$Re = \frac{\rho V l}{\eta} \tag{E.1}$$

Where V is the velocity, l is the characteristic length scale, ρ and η are density and viscosity, respectively.

$$Re = \frac{1260\ \frac{\text{kg}}{\text{m}^3} \times 270\ \frac{\text{m}}{\text{s}} \times 80 \times 10^{-6}\ \text{m}}{1.487\ \frac{\text{kgm/s}^2}{\text{m}^2}\text{s}} = \frac{1260 \times 270 \times 80 \times 10^{-6}}{1.487} = 18$$

The ratio of inertial to viscous forces is represented by the Reynolds number Re. Viscous forces predominate at low Re. It is a smooth fluid motion laminar flow regime. High Re results in turbulent flow and inertial forces that are predominant. The capillary number gives us an estimate of the effect of viscous forces vs. surface tension forces in the system. Ca can be deduced as,

$$Ca = V \times \frac{\eta}{\sigma_{ST}} \tag{E.2}$$

Where η is the liquid viscosity, and σ_{ST} is the surface tension between liquid and air.

$$Ca = \frac{270\ \frac{\text{m}}{\text{s}} \times 1487\ \frac{\text{mN}}{\text{m}^2}\text{s}}{63.4\ \frac{\text{mN}}{\text{m}}} = 6332$$

The extremely high value of capillary number suggests the negligent effect traditionally measured surface tension of liquid glycerol has in our case.

Validation of shell thickness estimate method

Our research requires an accurate estimation of the shell thickness. This is particularly important because we have observed a significant discrepancy between the Taylor-Culick velocity and surface energy values when only the surface tension contribution is considered. Our method, which makes simple and conservative geometric assumptions, has been very reliable in modeling the shell thickness in our system. However, since we do not have a complementary estimate for the shell thickness, there has always been a quest to verify the performance of the method. Fortunately, there were other studies where cavitation growth of acoustically levitated liquid droplets resulted in a thin liquid shell [155]. In this case, the volume of the droplet is known to the researchers, and assuming volume equivalence between the droplet and the resulting shell, an average thickness estimate is available. To validate our shell thickness estimation technique, an image from the article [155], specifically the image F.1, was used. From the scale bar, one pixel corresponded to about 32 μm. To increase the accuracy of the fit, we performed a simple linear interpolation of the intensity profile, which increased the data points by $10X$. Each data point corresponds to approximately 3.2 μm. The resolution limit of the imaging system mentioned in the article is 20 μm, which we use for the Gaussian convolution.

The intensity profile for the filled slice was taken from the locations marked with a red line in Figure F.1 and this is used to estimate the parameters for the transfer
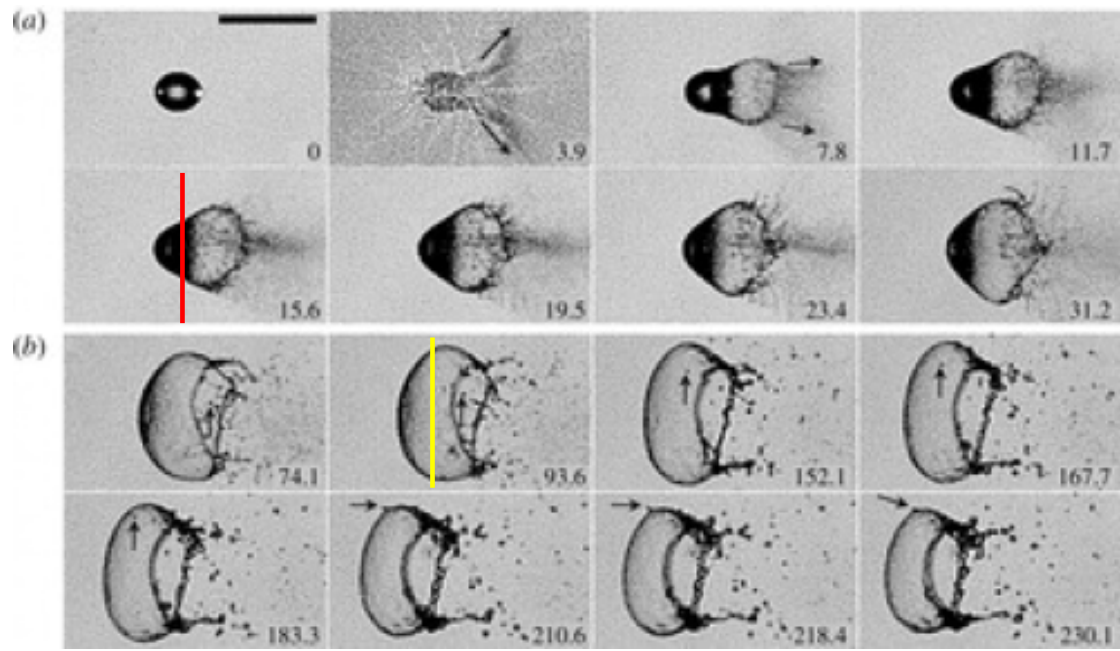
Figure F.1: Cavitation-induced stable shell formation used to verify the shell thickness estimation method. Figure adapted from [155]. Red line indicates the base profile Yellow line indicates the shell profile used for thickness estimation.

function,

$$I(Z_e) = I_0 \times exp(aZ_e^b) \tag{F.1}$$

Since the light level is constant throughout the images (varying between 200 and 0), we did not normalize the intensity values. Instead, we reintroduced the I_0 term. Figure F.2 shows the fit for the derived parameters.

Using these parameters, we tried to estimate the thickness of a shell. The average thickness of this shell is 10 μm, assuming volume conservation. Our estimate for a specific profile, shown with a yellow line in Figure F.1, is ≈ 15 μm, in agreement with Figure F.3. This is in excellent agreement with the estimate from the article.
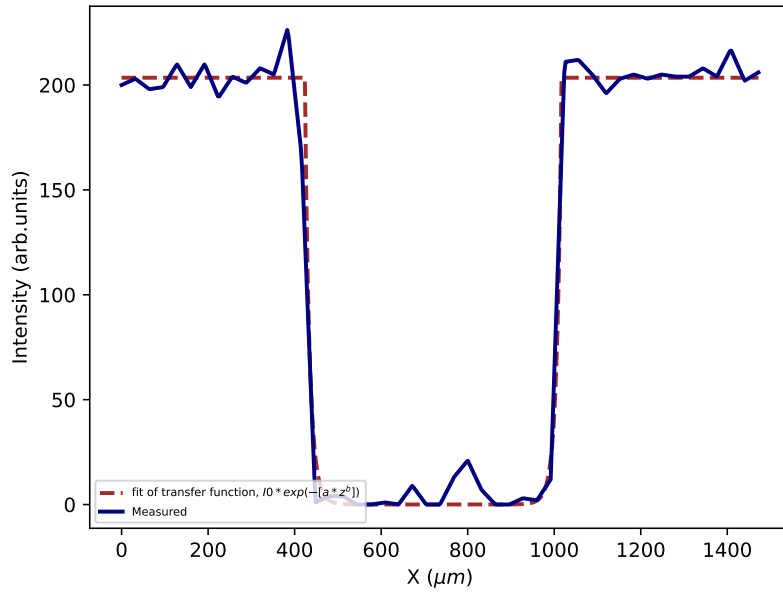
Figure F.2: Intensity profile over the red line shown in FigureF.1 in navy. The brown(dashed) line is the fit of the function shown in Equation F.1.
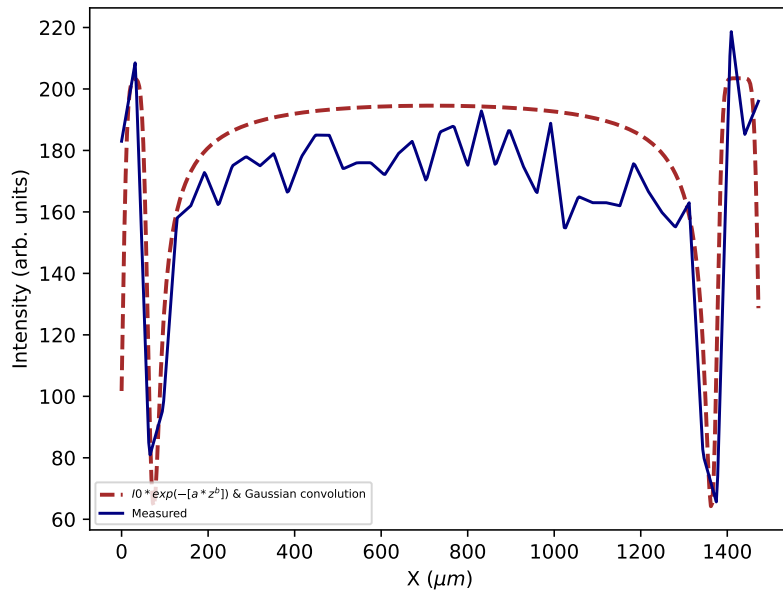

Figure F.3: Intensity profile over the yellow line shown in FigureF.1 in navy. The brown (dashed) line is the result of the transfer function shown in EquationF.1, where all parameters are determined in FigureF.2. The decay of the transfer function at the edges of the plot is the result of the convolution.

Appendix G

Surface tension

We are not able to explain the TCV we had during bubble rupture mearly by invoking surface tension. However, when discussing bubbles, surface tension is arguably the most important parameter determining a variety of properties [156, 157]. Also, in early spallation studies (typically in metals), spallation growth was described in terms of surface tension and viscous dissipation [158].

The definition and interpretation of surface tension can vary slightly depending on the field of study, such as mechanics, rheology, or thermodynamics. A thorough exploration of surface tension can be found in the 2018 article by Tovbin [159].

> Surface tension can be defined as the work required to create an interface unit[1].

Another interpretation can be that the free energy per unit area is equivalent to the surface tension, defined as the force acting on the unit length[2]. This force is tangential to the interface and prevents its spontaneous growth.

In most cases, equilibrium surface tension is sufficient to explain the stability and bursting of bubbles, as in the case of soap bubbles. However, when the process under consideration can induce non-equilibrium behavior, especially when there may be changes in pressure, density, and temperature, we need to look at the non-equilibrium

---

[1]Typical example is a vapor-liquid interface.

[2]SI of the surface tension is N/m (J/m^2), but typically mN/m = 10^{-3} N/m is used.

surface tension.

G.1. Non-equilibrium surface tension

As the term clearly indicates, non-equilibrium surface tension can be understood as the surface tension resulting from a deviation from equilibrium conditions. This can be due to dynamic processes involving variations in temperature, pressure, density, or a combination of all of these.

Dynamic surface tension is a subset of nonequilibrium surface tension. It results from molecular rearrangements in the fluid and at interfaces that cause the surface tension to change with time. An example that can help understand the effects of dynamic surface tension is when a mixture of water and surfactant is vigorously stirred. At equilibrium, the air-solution interface has a specific arrangement of molecules that is disturbed by stirring. Initially, the surface tension increases due to the absence of surfactant molecules at the interface (water has a higher surface tension compared to a water-surfactant mixture), but when stirring is stopped, the surfactants move to the interface over time, resulting in a decrease in surface tension compared to the moving fluid mixture.

The standard approach to dealing with surface tension in laser-induced bulk bubble/-cavity formation is to ignore it. This is because the contribution of surface tension is negligible compared to other high-energy processes in the system. However, in laser-induced bubble formation in metals, surface tension is sometimes invoked [113] to explain the dynamics. One reason could be the case of metals where the surface tension is orders of magnitude higher than that of simple molecular liquids such as glycerol[3].

In the case of the laser-induced bubble formation we encountered in glycerol, it is appropriate to consider the non-equilibrium surface tension and the dynamic surface tension before exploring other possible explanations for the persistence and bursting of bubbles. However, there is no established method for calculating these values for

---

[3]For example, liquid gold, the material studied by Inogamov et.al.[113] has a surface tension of $\sigma_{ST} \approx 1200$ mN/m [160] compared to that of glycerol with $\sigma_{ST} \approx 64$ mN/m.

phenomena such as laser ablation. Typically, even in the extreme case of laser ablation processes, the values determined for equilibrium conditions are used [161].

Because of the difficulty in estimating a value for the surface tension, the best approach is to observe the evolution of the surface tension in relation to the changes expected to occur during the laser ablation of liquids.

We can begin to evaluate a trend by looking at the relationship between pressure and surface tension. In the studies that have looked at the pressure-surface tension relationship [162, 163], the general trend is that the surface tension decreases with increasing pressure. Noticeably, no dramatic changes in measured surface tension were observed, suggesting no spontaneous decrease or increase in surface tension from pressure changes alone.

Regarding the relationship between surface tension and temperature, S.J. Palmer published an article in 1976 [164] in which he concludes that surface tension decreases with increasing temperature. Since we know that the temperature of the shell can increase, a decrease in surface tension is possible. Unfortunately, we have no direct evidence of such a surface tension variation.

Dynamic surface tension changes are the most complicated case of all those discussed here because of all the changes that occur to the surface during laser ablation. All of the parameters discussed above, such as temperature and pressure, change on the timescales that we observe the bubble, so in addition to the motion of the fluid and the interface, all of the other influences must be taken into account. However, without significant changes in density[4], we do not expect to see a dramatic change in the magnitude of the surface tension relative to its equilibrium value.

---

[4]This is only possible with pressures above the bulk modulus, which is a few gigapascals, or freezing of the liquid, neither of which are present in our case.

Acknowledgements

Jatropha or Nettlespurges are plants commonly grown in the Americas and best known for their use in bio-diesel production. It is quite rare where I grew up. But, one of these trees was in front of my parent's small farm. What fascinated me as a child was not its potential to produce bio-diesel but its ability to make bubbles. When you gently break the tender stem attached to the leaf and blow carefully at the fracture site, you can make tons of bubbles, and as a child, I always enjoyed doing that. I never in my wildest imaginations thought I would look and study bubbles for my Ph.D., but I would be lying if I said I didn't enjoy it as much as the kid blowing the jatropha bubbles. It took a lot of help from an uncountable number of people for that kid to reach the point of writing this thesis, and I am grateful for each one of them in my life. Those who inspired me and helped me reach this point deserve acknowledgment, but that will be a long and exhausting list, so I will stick to the people who helped me make my Ph.D. journey possible in the last few years.

First, I would like to thank the two people who spent their significant time, energy, and skills making this project a reality. Dr. Sascha Epp by being my de facto supervisor throughout the project, helping me constantly in developing the ideas, correcting me with all my silly mistakes, and holding me to a higher standard all the time (although I disagreed with him in this case occasionally, I am glad he did that). The second person is Dr. Zhipeng Huang, who started this project with me, guided me, and worked with me in realizing all the experiments. Although Zhipeng left MPSD earlier than I would have liked, he gave the necessary starting fuel to this work.

I am thankful to Prof. Dwayne Miller for allowing me to work on interesting problems with talented people. I would also like to thank Prof. Alf Mews for being my co-supervisor during a pretty convoluted Ph.D. journey. I express my gratitude to Prof. Volker Abetz for fulfilling the role of the second examiner for my thesis. I extend my

sincere appreciation to Prof. Arwen Pearson for being a member of my oral defense committee. I appreciate all the help I received from Dr. Franca Fuchs in navigating the chemistry graduate school. I would also like to thank Ms. Uta Fischer and Ms. Kathja Schroeder for all the administrative help I have received over the years.

I am fortunate to be placed in the sub-group where I had tons of fun discussing science, technology, food, and everything in between with Dr. Andrey Krutilin and Dr. Frederik Busse. Beyond my sub-group, I am particularly thankful to Dr. Heinrich Schwoerer, Dr. Günther Kassier, Hendrik Schikora, Dr. Simon Bittmann, Dr. Lindsey Bultema, Dr. Gabriele Tauscher, Djordje Gitaric, and Kirsten Teschke.

Outside MPSD, I am glad to have had the great company of friends who made Hamburg feel special. Mahesh, Harita, Steffi, and Swathi for welcoming me and being there for me with all the flavors (not just in terms of food) of Kerala. I could not have survived my anxiety without my newly discovered love for climbing and bouldering. I must thank Mike and Angus (along with Günther again) for making these activities special. As I moved continents for my Ph.D. I was scared of losing some ties with my home. However, Sanjeev, Bipin, Ajith, Mibin, and Gokul have shown me that our friendship can survive much more and have soothed me of that fear. I am forever thankful to you for the fifteen-plus years of our company.

Someone who came to my life the most unexpectedly during this time and made it special is Lieke Fröberg. I cannot thank you enough for your companionship, ability to make me smile, impeccable proofreading skills, and much more. Your love made my hardships during the last few years bearable and my life more beautiful.

Finally, I want to thank my family for caring for me, loving me, and being there even through tough times. I would not be the man I am today without my father's love and care, my mother's kindness and resilience, my brother's many sacrifices, and his wife's voice of reason.

Declaration on Oath

I hereby declare on oath that this doctoral dissertation is written independently and solely by my own based on the original work of my Ph.D. and has not been used other than the acknowledged resources and aids.

Signature:

Hamburg, Date: 01-11-2023